Table of Contents

1. Introduction

This final report documents the research completed under the proposed research effort entitled "CALIPSO and LITE Data for Space-based DWL Design and Data Utility Studies" which was awarded in response to NASA Research Announcement NNH07ZDA001N; Research Opportunities in Space and Earth Sciences – 2007(ROSES -2007) under TopicA14 Wind Lidar Science, Opportunity 1. Although it was first envisioned that the proposed work would include investigations of the older LITE data set, the researchers decided to focus solely on the Cloud-Aerosol Lidar and Infrared Pathfinder Satellite Observations (CALIPSO) data and its' extension to a potential Global Wind Observing System (GWOS) in order to conduct basic trade studies that relate directly to space-based Doppler Wind Lidar (DWL) design and scanning options.

2. Objectives

The main objectives of the research effort are summarized below:

2.1 Construct CFLOS statistics

The first objective was to use the cloud data from CALIPSO to construct Cloud Free Line Of Sight (CFLOS) or cloud penetration statistics that could be used to conduct DWL sampling trade studies and to help guide the instrument design of future space-based DWLs. The primary LOS statistics are:

- cloud cover and ground detection statistics
- probability of CFLOS penetrations to specific levels (1 km vertical resolution) in the atmosphere;
- probability of multiple level interception of clouds of low to modest optical depths (tau < .5);
- probabilities of contiguous CFLOSs for various duration of beam stares and shot integration.

This work included analyzing and investigating the Level 2 CALIPSO data products, specifically the cloud layer products to see how they compared with other measurements and the values used in current Observing System Simulation Experiments (OSSEs) and simulation models, focusing on the potential future GWOS.

2.2 Develop global PDFs

The second objective was to develop global probability density functions (PDFs) of aerosol backscatter. The primary atmospheric optical properties are:

- PDFs for the background mode of backscatter at measured wavelengths
- PDFs for the "enhanced mode" of backscatter at measured wavelengths
- Attenuated backscatter or transmission (2 way) PDFs at measured wavelengths

This work included analyzing and investigating the Level 2 CALIPSO data products, specifically the vertical profiles of total backscatter to see how they compared with other measurements and the values used in current Observing System Simulation Experiments (OSSEs) and simulation models.

2.3 Extend findings in 2.1 and 2.2 to GWOS, OSSEs, and DWL design studies

This third objective was to extend the basic findings from 2.1 and 2.2 to the potential future GWOS 2 micron coherent sub-system:

- Converting backscatter and transmission statistics at measured wavelengths (532 and 1064 nm) to GWOS coherent wavelengths (e.g., 2010 nm.)
- Developing cloud/aerosol backscatter correlations with atmospheric phenomena (fronts, tropical storms, high pressure systems) or variable (such as relative humidity) for use in OSSEs
- Validating and calibrating backscatter and cloud distributions and optical properties being used in OSSEs and DWL design studies
- Conduct instrument design trade studies and to design follow-on OSSEs to explore the potential impact of the CFLOS and aerosol distribution knowledge resulting from the previous work

3. Results

As mentioned in scientific articles such as Winker et al., (2010) and many others, the CALIPSO mission which was launched in April, 2006 and continues today, combines an active lidar instrument with passive infrared and visible images to probe vertical structures and properties of clouds and aerosols. In particular, the Cloud-Aerosol Lidar with Orthogonal Polarization (CALIOP) is a two-wavelength polarization-sensitive lidar that provides high-resolution vertical profiles of aerosol and clouds. The CALIOP measures backscatter intensity from aerosol and clouds at 532 nm and 1064 nm with 70 m horizontal resolution sampled every 333 m and 30–60 m vertical resolution (depending on the height in the atmosphere). Level 2 cloud layer products are also created for the 333 m resolution as well as for 1 km and 5 km resolutions. This study uses all three Level 2 layered products.

A main objective of this CALIPSO data analyses was to devise cloud (and ground return) statistics and CFLOS statistics for the CALIPSO cloud products. In addition, comparisons were to be made against similar existing statistics such as were found for LITE and GLAS.

A previous NASA ESTO funded analysis of GLAS cloud data by the PI (Emmitt and Greco (2006)) revealed global total cloud values (80%) which is very close to those found with a small set of data from LITE. These values are higher than values determined from ISCCP (60-70%), suggesting that active optical remote sensing is revealing higher cloudiness due to the increased sensitivity of the measurement. The primary results of that study were:

1) 70 - 80% of the GLAS lidar samples involved some return from clouds (assumed that "no cloud/no ground returns" intercepted physically thick layers of optically thin clouds and thus not meeting the "cloud" threshold at any one level)
2) 75 - 80% of the GLAS lidar samples detected the earth's surface (adjusted for smooth water returns)
3) When clouds were present, At least two layers were detected between 25 – 40% of the time.

Utilizing the experience and lessons learned from the LITE and GLAS analyses, the goal was to devise a more complete and detailed set of statistics using CALIPSO data that can also be compared to the previous results.

3.1 Cloud and Ground Detection Statistics

For the purpose of this analysis, we looked at the latest version/release (V3.01) of the CALIPSO Level 2 Cloud Layer products for all three available resolutions (333 m (single shot); 1 km (3 shots); 5 km (15 shots)). A two-day period was selected (August 8-9, 2007) and the data from this entire period, giving global coverage, was utilized.

Prior to discussing the results, we would like to note that the CALIPSO 1 km cloud product is closest to the GLAS "High" resolution (8 shots over 1.4 km horizontal) and the CALIPSO 5 KM product is closest to the GLAS "Medium" resolution (40 shots over 6.8 km horizontal). In addition, it should also be noted that when, making comparisons between statistics derived for different resolution products or for differing shot integration intervals, the following must be taken into consideration. The likelihood of cloud detection within the interval is a function of both the degree of threshold sensitivity and the area of regard. The more individual shots averaged together to determine the signal to noise ratio (SNR), the more likely it is that optically thin clouds will be detected. Also, the longer the shot integration interval, the more likely it is that an individual shot or lower resolution product will intercept a cloud.

Tables 1 and 2 provide a summary of various cloud cover and cloud layer statistics for the Calipso Level 2 Cloud Layer date products at 333 m, 1 km and 5 km resolution for, respectively, night-time and daylight observation. Cloud statistics (in terms of percentages) presented include the percent of time cloud was or was not reported for the product as well as the distribution of number of cloud layers.

From Table 1, we can see the following cloud statistics:

- 44-49% cloud cover for CALIPSO 333 m
- 67-70% cloud cover for CALIPSO 1 km (3 shots)
- 69-71% cloud cover for CALIPSO 5 km (15 shots)

This trend was as expected given that more shots (with the ability to intercept cloud layers) with the coarser resolution cloud products. Previous analyses of the GLAS High and Medium resolution products showed, respectively, 49.1% and 73.2% cloud cover. The global cloud cover percentages determined for the 1 km and 5 km resolutions are very similar to previous investigations of CALIPSO cloud cover and comparisons with AIRS (66-74%) (Stubenrauch et al., 2010) and GLAS/LITE (Berthier et al., 2008).

There was also an expected variation in the number of cloud layers depending on the individual CALIPSO cloud layer product. When there were clouds, between 75-82% of the 333 m and 1 km products had ONE cloud layer. These results confirmed what the analysis of the GLAS High resolution product found (70% for a single cloud layer). However, for the 5 km CALIPSO product, this only happened 55% of the time when there were clouds. More importantly, as compared to findings of only 2-5% of the time for > 2 cloud layers (when there are clouds) at both 333 m and 1 km, more than 2 cloud layers were found over 20% of the time for the 5 km product (more shots to detect cloud layers). Once again, this confirmed the results of the GLAS Medium resolution analysis which found more than 2 cloud layers over 25% of the time. Looking closer at Tables 1 and 2, we see that there was not a significant difference in cloud cover percentages (total cloud cover and cloud layers) between the daytime and night-time observations. This was true for all three resolutions.

The individual cloud products were looked into with more detail to investigate the effects of different surfaces (i.e., land and water). These results are shown in Tables 3-5. As shown in Tables 3-5, the small differences (3-8%) seen in the day-night comparisons of Tables 1 and 2 also extends to both land and water surfaces at all three resolutions of the CALIPSO Level 2 Cloud layer products. From these tables we can see that, for night observations, the cloud cover percentage is 25.2%, 25.6% and 14.9% larger over the water surfaces as compared to land surfaces for, respectively, the 333 m, 1 km and 5 km Level 2 cloud layer products. This difference is much smaller during the day time for the 333 m and 1 km resolutions (~ 15%), and similar to the 5 km product.

In addition to clouds, we also investigated the occurrence of ground returns. These "ground statistics" can also be seen in Tables 1 and 2. Looking at the 1 km and 5 km products, we see in

Tables 1 and 2 that between 52 and 66% of all CALIPSO products detected a ground return. This is very similar to the results from LITE (60-65%) and GLAS High resolution before adjustments were made (45%). As shown in these tables, we also note that, of all the products that detected cloud, 30-45% and 38-52% of, respectively, the 1 km and 5 km product also hit ground. Once again, this fits in very nicely with previous findings which showed this number to be 37-50% (LITE) and 34-49% (GLAS High and Medium resolution). However, looking at the highest resolution single shot or 333 m data product, it is seen that only 9-18% of the individual shots that hit cloud also hit the ground, signifying the important role of attenuation and the need to accumulate shots or favor high energy per pulse.

Further analyzing both the CALIPSO Level 2 1 km and 5 km cloud layer products, it is shown in Tables 4-5 that there were higher ground returns over land (58-68% for 1 km; 63-72% for 5 km) compared to the percentage of ground returns found over water (49-52% for 1 km; 52-57% for 5 km). It is also seen that these differences are much larger in the night then during day-light. This difference is probably due to lower returns from smooth water surfaces that may not be considered Lambertian.

3.2 CFLOS and Pass Through Statistics

Reinke et al., (2010) utilized CloudSat and CALIPSO data to determine CFLOS, including beneath opaque cloud layers, by looking at 10 degree intervals from nadir to 90 degrees and computing the probability of CFLOS at many vertical levels between the surface and 20 km. We have been making similar computations in this study but with a focus on the impacts of CFLOS (mainly nadir) on potential space-based wind lidar technology and performance (as will be discussed below). For both the selection of different lidar technologies (e.g. coherent and direct detection) and the choice of sampling strategies, one important consideration is the number of shots or even consecutive shots that either have a CFLOS or, despite clouds, make it to the ground or to a particular level in the atmosphere over a specified distance (temporal stare). The strategy employed in this research was to investigate CFLOS and “Pass Through” statistics for various integration distances, namely 25 km, 50 km and 75 km.

The term “pass through” denotes statistics based upon the positive answer to the question: “Are there returns (cloud or ground) reported for lower layers?” For example, if we are dealing with the 1 km product and the integration distance is 50 km at 10 km height, then the question is asked of 50 contiguous products at that level. If all answer yes, then that 50 km segment is recorded as a case of 100% pass through at the 10 km level. If only 25 products reached a lower level or the ground, then this is identified as 50% pass through. One point that needs to be emphasized is that all that is required for a “pass through” is a lower level return, not necessarily a ground return. Another point to keep in mind is that, if identified as a positive pass through because of cloud return, there could have been cloud detected by any of the individual shots that compose the products (i.e. the 3 individual shots that comprise the 1 km product). Thus the "pass through" statistics tend to belie the amount of cloud that is intercepted by the 3 shots over 1 km.

On the other hand, the question may be: "How many of the products down to 10 km arrived without any cloud detection?" The answers to this question would form the CFLOS statistics. For example, if the integration distance is 50 km for the 1 km product at 10 km, then the question of no cloud detected down to 10 km is asked 50 times (consecutively). If 50% answers yes, then that 50 km segment is recorded as a case of 50% CFLOS. It must be kept in mind that this test of "no cloud" does not give credit to those cases where, perhaps, only 1 of the 3 individual shots hit a cloud and the remaining shots were cloud free. <u>Thus the tendency is to understate the CFLOS opportunities at the 1 km scale (and probably 5 km scale).</u>

The set of "pass through" statistics may be most useful for investigating an instrument that needs only a few of its attempts to get through clouds to still provide a useful data product. The coherent DWL is an example where the accuracy of the observation is tied to a threshold number of photons (as opposed to direct detection where accuracy scales to the total number of photons). On the other hand, the statistics returned as an answer to the second question asked (i.e., how often, for selected sampling distances, are there CFLOS down to various levels) are of most interest to direct detection lidar performance since accuracy is strongly tied to the number of photons returning and the problems associated with cloud reflectance as a background source of noise photons.

Below, we present CFLOS and "Pass Through" statistics in the form of a percent of occurrence versus percent of "shot product" graph for all three CALIPSO Level 2 resolutions. We initially looked at a small data sample (4 files) on August 8-9, 2007 to study the differences between the CFLOS statistics of the various data resolutions. Initially, only the 1 km and 5 km pass through statistics were computed as there was some uncertainty about the ground hits at the 333 m resolution. For comparisons with previous missions and data sets (LITE, GLAS, etc.,), we have focused on the 5 km and, especially, the 1 km CALIPSO cloud layer products and their computed CFLOS and "pass through" statistics.

Looking at the Pass Through figures 1-4, we initially saw the following:

- Little difference is seen between the 1 km and 5 km product EXCEPT for the 100% pass through. This difference is as large as 15% below 10 km
- Integration distance means very little except for the highest "pass through" success
- The efficiency (i.e., 100%, 80% and 50%) of products reaching a certain level contributes the largest difference and explains most of the variability within the opportunity windows.

Similarly, looking at the CFLOS results (Figures 5-10) we can see that there is a larger difference between the 1 km and 5 km products (up to 10-12%) then was found for the Pass Through statistics. This reflects the cloud cover differences illustrated in Tables 1-5.We also found the following:

- Even bigger differences (20-30%) between the single shot 333 m products and the 1 km product (This could be expected due to cloud statistics shown earlier where there was a 20% difference between the 333 m and 1 km cloud cover)
- Again, as with the pass through statistics, the integration difference makes little impact
- Changes in efficiency (100%, 80% and 50%) once again make the biggest impacts on the CFLOS statistics

Before discussing these results and their impact on space-based DWL design studies (i.e., coherent vs direct detection), we focused on the statistics generated using the 1 km CALIPSO Level 2 Cloud Layer Product, especially for comparison with previous studies and data sets like LITE and GLAS, for the entire two day period of August 8-9, 2007.

To illustrate the results, we provided the similar figures for the 1 km product (Figures 11-16) as mentioned as well as in tabular format. Tables 6-11 are individually used to show the impact or lack of impact of integration distance while comparing Tables 6-11 can give us further insight into the impact of efficiency requirements. The small impact of integration distance is clearly seen. More specifically, we see the following:

- Again, except for the 100% (and probably down to 90%) requirement for both Pass Through and CFLOS, the integration distance is shown to have little impact
- The significant impact of the efficiency requirements is clearly seen

Comparisons with previous GLAS High resolution Pass Through statistics (not shown) revealed the following:

- For 100% pass through at 75, 50 and 25 km integration distance, the pass through is greater for GLAS down to ~ 3 km but greater for the CALIPSO 1 km below 3 km
- However, at 80% and 50% pass through at 75, 50 and 25 km integration distance, the pass through is greater for the CALIPSO 1 km product below 10 km

Regarding the CFLOS statistics, comparisons with GLAS data show that:

- At 100% CFLOS for 75, 50 and 25 km integration distance, the GLAS CFLOS is greater down to ~ 3 km and greater for CALIPSO 1 km below 3 km

- Unlike the pass through statistics, this is very similar for the 80% and 50% CFLOS, with the change over height being somewhere between 3 and 5 km

As mentioned earlier, the "pass through" and CFLOS statistics we have presented in the form of tables and figures can be very beneficial to trade studies investigating the requirements, scanning strategies and performance of space-based DWL such as the potential GWOS configuration which may include both a coherent DWL and a direct detection DWL. These statistics can help us determine what type of trades have to be made between accuracy, energy (to get the required number of shots), and integration distance (averaging). This, and the type of scanning strategy (say, a few concentrated shots versus a shot gun or scatter approach), will depend on the type of DWL technology as the coherent lidar just needs a pre-defined threshold number of shots through to the target while the performance or accuracy of the direct detection system is usually directly scaled to the number of photons used in the measurement.

Before continuing, it should be noted that the Energy-Aperture Product (EAP) is often used as a figure of merit for lidar design where:

EAP (coherent) = E * sqrt(prf) * A

EAP(direct detection) = sqrt(e) * sqrt (prf) *A

and where

E = energy per pulse (Joules)

PRF = pulse repetition frequency (Hz)

A = area of primary collector (meters squared)

An important usage of the CFLOS data would be in the specification of the integration interval necessary for achieving specified target measurement accuracy in the presence of clouds. In some cases, the instrument trade may involve trading greater energy per pulse for a lower pulse rate, simply having to increase the overall EAP to get sufficient return over less time (shorter integration distances). In the case of direct detection, the performance of the system is usually directly scaled to the square root of the number of photons used in the measurement. When multiple shot integration is required to obtain the needed photon count, the question is then "How often do clouds preclude getting the required photon count?" Another way to ask that question is "What are the probabilities of getting the required number (say, 50% or 80% or 100%) of individual shots through to various levels of the atmosphere when clouds are in the target area?" While there are unlimited variations on the choice of target integration times and signal return requirements, we can make a few general summary statements from the tables and figures that were presented:

1. As shown by the cloud statistics, especially for the 1 km and 5 km products, clouds in a Lidar LOS are the rule (~ 80%). Whether the cloud is detected and penetrated depends upon the lidar's energy output and the optical depth of the cloud. The lidar's sensitivity to

optically thin clouds and aerosols can be improved by shot integration. However, reliable shot integration can be frustrated by cloud cover variation within targeted sampling windows.

2. In cloudy situations, the longer the integration time (distance) the less likely all shots will reach a target layer beneath clouds. However, the success rate does not scale linearly to the integration distance. For example, going from 80% success at 75 km may only improve by a few % by going to 25 km integration.

3. The CFLOS and "pass through" data generated from the CALIPSO Level 2 cloud layer products suggest that more coverage is gained by increasing the strength of the signal or the sensitivity of the lidar (higher EAP) rather than increasing the integration time (distance). Thus, these results show that a better trade would be the increasing (or decreasing) the required success rate by decreasing (or increasing) the EAP or selecting a technology with an accuracy dependent upon the number of shots.

3.3 Cloud and CFLOS Statistics: Tropics vs Mid-Latitudes

As part of this funded research, we also wanted to investigate the difference in cloud and CFLOS statistics on the global scale, specifically looking at various zonal regions such as the Tropics (30N – 30S), Mid-latitudes (30 – 60 S/N) and Polar (60 – 90 S/N) and investigating differences. For this exercise, we utilized the CALIPSO 1 km product.

Looking at Table 12, it can be seen that there is little difference in the percent cloud cover over the various regions, ranging from 67% in the tropics to 75% in the mid-latitudes. However, a much higher percentage of the laser shots or products (3 shots in each 1 km product) makes it to the ground in the tropics (60.1%) as compared to the mid-latitudes. A reason for this and the preceding cloud cover statistics may be the increased presence of thin high clouds (some of which also may not be detected) in the tropics that allow the laser beam to continue to the ground and the larger amount of lower, thicker clouds in the mid-latitudes which are detected but lead to complete extinction. This is further supported by the Cloud/No Ground statistics for the tropics (38.8%) and mid-latitudes (51.4%).

CFLOS statistics were then computed for the 1 km CALIPSO product and analyzed to further investigate these differences. This information is shown in Tables 13-15 (Pass Through) and tables 16-18 (CFLOS). From the CFLOS statistics, we can see the "smaller" CFLOS above 5 km in the tropics as compared to the mid-latitudes and very likely indicating the increased detection of high clouds in the tropics. Similarly, the higher (lower) CFLOS below 5 km indicates a decreased (increased) detection of lower clouds in the tropics (mid-latitudes).

However, at the same time that the CFLOS indicate the higher amount of high clouds in the tropics, the Pass Through statistics show a higher percentage of the laser shots or products at the 1 km resolution make it to the lower levels or ground in the tropics, perhaps indicating that much of the higher clouds that are detected by CALIPSO are thin enough (and the laser strong enough) to allow the laser beam to continue downward and return useful measurements.

3.4 Application CALIPSO Level 2 Aerosol Profile Data to the 2 micron component of GWOS

To conduct OSSEs and DWL trade studies, SWA employs a Doppler Lidar Simulation Model (DLSM) which utilizes target atmospheres generated from global scale Nature Runs such as the ECMWF T511 NR. However, this can't be done directly with aerosol and backscatter as the gridded fields for these parameters are not provided. Thus, aerosol or backscatter profiles for these target atmospheres have been taken from community approved climatological backscatter profiles (for "background" and "enhanced") that were previously generated from historical field campaign data sets (GLOBE, SABLE/GABLE). The backscatter profiles in the DLSM are then slaved to the relative humidity fields of the Nature Run and then used in the OSSEs.

Thus, one of the objectives of the proposed research was the analysis and investigation of the Level 2 CALIPSO 5 km profiles products, specifically the vertical profiles of total backscatter, to see how they compared with other backscatter profile measurements, in particular the values used in current OSSEs and simulation models that are focusing on GWOS trade studies.

Before describing the related analyses of CALIPSO data, the backscatter modes, "background" and "enhanced" mentioned earlier are briefly defined. Imagine a global 3D grid with horizontal cell dimensions of a few 10's of kilometers and a vertical thickness on the order of 1 km. We then take lidar taken from airborne campaigns (e.g. GLOBE, SABLE/GABLE) and bin it by altitude and the log of the back scatter coefficient. One feature of the histogram is a persistent log-normal PDF with a median value we refer to as the "background" mode. This "background" mode is found mainly in the upper troposphere and where there are few surface sources of large aerosols. The chemical identity of these "background" mode aerosols is often sulfates with low number concentrations and weak backscatter cross sections. In Figure 17, the "background" mode is shown in red with a median (dark red line) value and the 1 sigma width of the distribution.

While the "background" mode is considered to be rather stable (globally) with long (weeks-months) half life's, the second mode ("enhanced") is more transient or episodic. This higher backscatter mode is usually associated with local sources of aerosols (surface dust, salt sprays) that are injected and transported vertically by convection or high wind driven mixing.

Our PDF model for global backscatter is thus bi-model and varies vertically around the globe. Our objective in this part of the CALIPSO research has been to obtain an estimate of the frequency of occurrence of the two modes. We would expect the occurrence of the "enhanced" mode to be more frequent in the northern hemisphere than in the southern hemisphere due to the higher amount of land mass and anthropogenic sources of aerosols. A primary two part question being asked of the CALIPSO data is " what is the lowest backscatter coefficient detectable by CALIPSO and can it be used to obtain an estimate of the percentage of the globe (vertical and horizontal) dominated by the "background" mode. We argue that if we can detect just the upper portion of the "background" mode PDF (as seen in Figure 17), then we can say that the situations not detectable by CALIPSO are "background" mode cases. While this is not strictly true due to a continuum of attenuation conditions, it would still be a better source of information than anything else we currently have on a global scale.

Next we describe the two step process we used to obtain backscatter information at 2 microns , the wave length most important to the GWOS concept since the coherent sub-system depends on the aerosol backscatter (while the direct detection depends upon the molecular backscatter). The first step is to establish the distributions of backscatter at CALIPSO's 532 µm and 1064 µm wavelengths. The second step is to use the wavelength conversion model (coefficients) derived by UAH as part of this research effort (see attached report from UAH) to express the opportunities in terms of 2.012 µm.

To meet the objectives of this task, SWA acquired, processed, reformatted and analyzed the CALIPSO Level 2 Aerosol Profile data available from the Atmospheric Science Data Center at Langley. Initial analysis began on the then most current data set (Version 2.2). The only Level 2 aerosol profile product available in this data release was the CALIPSO Lidar Level 2 aerosol profile data using the CALIPSO Lidar Ratio selection algorithm at 40 km resolution. After looking at the initial analysis results and consulting with Dr. David Winker of LaRC, it was decided not to proceed with the analysis of the vertical profiles of backscatter and wait for the improved Version 3.01 data release. This data became available in April-May of 2010 and contained CALIPSO Lidar Level 2 aerosol profile data at 5 Km resolution, the same as the cloud profile data. The Level 2 CALIPSO aerosol profile data provides backscatter measurements throughout the troposphere and stratosphere at ~60 m vertical resolution. As was done previously, the new data was acquired, processed, reformatted and analyzed.

A primary focus was to investigate the sensitivity of the CALIPSO Level 2 aerosol profile backscatter measurements and, specifically, to how very low values of attenuated backscatter were determined from the CALIPSO observations and if this data could provide information and guidance that could be used in describing the global background mode of aerosols in GWOS simulation studies. Histograms of the observations for a day (or month) were created for several vertical levels.

In Figure 18 (taken from Winker et al., 2010), the estimated threshold sensitivities for CALIPSO (and LITE) are shown. We will use the nighttime 80 km value of 2.7 E-4/km/sr (2.7 E-7/km/sr) at the 532 µm wavelength. Later we will the implications for 2 µm operations.

Presented here are the histograms or distribution of Level 2 532 nm total backscatter coefficient values at 1000m AGL for a single day (August 1, 2007) and utilizing the log of the backscatter coefficient as the x-axis. Figure 19 (all cases) and Figure 20 (no cloud above) contain all possibilities at 1000m, including where no aerosol was detected (the furthest right column for presentation purposes) while Figure 21 contains only the observations where aerosols were detected. It should be noted that, for the sake of comparisons, both have been normalized to the 2010 nm GWOS wavelength.

From Figure 19 we can see that, even at 1000m AGL, only 15-20% of the time are aerosols detected in the Level 2 aerosol profile product. Even when there are no clouds above the 1000m AGL level, only 35-40% of the time are aerosols detected. This may cast some doubt on the sensitivity of the aerosol detection algorithm for the Level 2 data .

However, looking at Figure 21 in comparison with a similar distribution of attenuated backscatter from the background aerosol mode at 1000m AGL computed from the ECMWF T511 Nature Run (Figure 22), it is seen that the CALIPSO Level 2 products do a good job of representing the higher end of the cleaner or background mode of aerosols but may not provide enough sensitivity to represent the weaker end or tail.

3.5 CALIPSO Backscatter: Modeling, PDFs and Wavelength Conversion

Another main objective of the research, done mainly by the co-investigators at the University of Alabama-Huntsville (UAH) in collaboration with SWA was "Using measurements of attenuated aerosol backscatter and retrievals of aerosol backscatter and extinction coefficients at 0.532 µm and 1.064 µm from CALIOP to predict aerosol backscatter coefficients, aerosol extinction coefficients, and attenuated aerosol backscatter at the 0.355 µm and 2.01 µm wavelengths." To accomplish this, UAH used in-house aerosol scattering models to derive theoretical conversion factors for aerosol backscatter coefficients and aerosol extinction coefficients among all pairs of the four wavelengths (0.355 µm, 0.532 µm, 2.01 µm, and 1.064 µm).

Attachment 1 contains a detailed report of the activities, methods and findings for these tasks. Found below is a high level summary of the important results that have come out of this work.

An aerosol scattering model has been developed that computes the volume backscatter coefficient, volume extinction coefficient, volume scattering coefficient, single-scatter albedo, and lidar ratio at a given wavelength and relative humidity, for spherical aerosol particles with arbitrary concentrations, size distributions, and compositions. The scattering model was applied to the six distinct aerosol types (Omar et al., 2009) used by CALIOP (Smoke, Dust, Polluted Dust, Clean continental, Polluted continental, and Clean marine) and extrapolated to NASA's prospective Global Wind Observing System (GWOS). Using the existing CALIOP models for the aerosol physical and chemical properties for both instruments, the CALIOP optical properties at the CALIOP wavelengths (0.532 μm, 1.064 μm) were extrapolated to optical properties at the GWOS wavelengths (0.355 μm, 2 μm). Modeled scattering properties for the six wavelength pairs were ratioed and parameterized in terms of their wavelength dependence. The end-to-end uncertainties in modeled aerosol backscatter at the GWOS wavelengths, including CALIOP calibration, data processing, detection thresholds, and aerosol models; and UAH aerosol models was also examined.

The major conclusions of this part of the effort were the following:

- Based upon the modeling, an Angstrom exponent for 532-2064 nm would be 1.36-2.23 for bimodal fine conditions and .11-1.36 for coarse conditions (Table 19). Prior DWL simulations based upon LITE and GLOBE measurements at 532 nm have used a 532-2064 nm Angstrom exponent of 2.5 ($beta_{2.06}/beta_{.532}$ = .034) for the background mode and 1.5 ($beta_{2.06}/beta_{.532}$ = .125) for the "enhanced" or coarser mode. <u>Thus, the angstrom coefficient used to model the 2 micron backscatter from 532 nm in DWL simulations that have used the target atmospheres most likely understated the backscatter and the aerosol pdf median by a factor of ~2-5 for "background" situations and, perhaps, a factor of ~ 2-7 for "enhanced" conditions.</u>

- Modeled aerosol backscatter color ratios fell into two classes: (a) clean, with backscatter properties dominated by coarse particles, and wavelength exponent of order unity; and (b) anthropogenic, with backscatter properties dominated by fine particles, and wavelength exponent of order 2. Color ratio dependence on these broad aerosol types was much more important than variations within these broad types.

- Color ratio dependence on the broad aerosol types was also more important than variations with relative humidity. The humidity-dependent variations fell into three classes: (a) low humidity, where backscatter color ratios showed little variability; (b) intermediate humidity, where these quantities showed rapid fluctuations (presumably related to the "optical glory phenomenon), in the clean aerosol types, and smooth monotonic growth or non-monotonic features for the other aerosol types; and (c) high humidity, with large rapid changes that varied by aerosol type. Color ratio variations in the intermediate humidity range were small enough that GWOS screening studies could treat low and intermediate humidity as a single domain for each aerosol type. Color ratio uncertainties at high humidity will not be important until free-running global numerical models can generate realistic high-humidity fields.

- Backscatter values at the GWOS wavelengths, and backscatter color ratios between CALIOP and GWOS wavelengths, could encounter very large uncertainties from unknown complex index of refraction for organic constituents at 0.355 μm, and from optical resonances in sulfate-coated dust at 2 μm.
- Uncertainties in the physical, chemical, and optical properties of the six CALIOP aerosol models were less important than uncertainties in the aerosol optical constants at GWOS wavelengths. These uncertainties alone do not warrant reformulating CALIOP models or reprocessing CALIOP data for GWOS applications.
- Nevertheless, aerosol backscatter conversions from CALIOP to GWOS wavelengths should use Level 1 attenuated total aerosol backscatter ratios, instead of Level 2 backscatter and extinction. The Level 1 product is calibrated from first principles. It has not undergone *a priori* algebraic thresholding that sacrifices information content when aerosol backscatter is much smaller than molecular backscatter. Equally importantly, it avoids compounding errors that assumed or derived aerosol models otherwise impose on conversions from attenuated backscatter (at CALIOP wavelengths) to extinction and backscatter (at CALIOP wavelengths), and back again to attenuated backscatter (at GWOS wavelengths).

3.6 Investigating correlations between Calipso Level 2 Aerosol Backscatter Profile data and Relative Humidity

Observations of total attenuated backscattering intensity at 532 nm and total attenuated backscattering intensity at 1064 are obtained for CALIPSO at a vertical resolution ranging from 30m (0.5 km and 8.2 km) to 60m (between 8.2 and 20.2 km) and horizontal resolution 333 m. The most recent studies of CALIOP 532 nm total attenuated backscatter show very good agreement (2.7 – 2.9% plus/minus 2.1%) with airborne backscatter measurements such as those from the HSRL (Rogers et al., 2011). Level 2 averaged layer products are also available at 1 km and 5m. However, the Level 2 averaged vertical profiles that this study makes use of is the 5 km resolution.

Based on previous research undertaken by the current investigators, it was decided that rather than investigate the correlations between the Level 2 profiles (5 km resolution) of atmospheric backscatter and parameters that in part define synoptic atmospheric features such as high/low pressure centers or fonts or jets, it was decided to investigate the relationship between the Level 2 aerosol backscatter profile data and the atmospheric relative humidity (RH). This was done by utilizing values of RH passed on by the Calipso Level 2 Profile product which is taken from the GEOS model. Another reason for focusing on the relationship between RH (and not a number of parameters associated with atmospheric phenomena) and backscatter is that a current Doppler Lidar Simulation Model (Wood, et al., 2000) utilizes values and, especially, the variability of RH to represent or drive the variability in the model global scale backscatter fields.

As in previous studies such as Lamquin et al., 2009, for validation, we looked at the comparisons between model forecasted RH (ECMWF re-analysis) and the location of CALIPSO Level 2 Cloud Profiles and, as expected, found high model RH where there was high cloud amounts. Many other studies have shown the co-location between model or in-situ RH and the location of CALIPSO clouds, but also sometimes inferring a similar relationship with backscatter. As far back as the work of Hamel and Frankenberger and Werner (1972) relationships have been demonstrated between the backscatter coefficient and relative humidity. Some more recent studies have been focused on the cloud-RH-Backscatter relationship. A recent study by Su et al., 2008 using HSRL data showed that aerosol backscatter is ~ 20-30% higher in proximity of clouds as compared to 4-5 km away. However, there was still a question about how much is explained by changes in RH. Twohy et al., 2009 utilized airborne data to show an increase in RH as the distance from the edges of small trade cumulus decreases and also indicated a 40-80% increase in aerosol scattering cross section. Finally, Tackett and Di Girolamo (2009) used CALIPSO data to show backscatter is enhanced adjacent to the cloud (trade winds) edge where the RH also increases. They found layer integrated median backscatter at 532 nm (1064 nm) increase by 31% (42%) when moved closer to the cloud edge. Similar results (20-30%) with HSRL data were presented by Ferrare et al., (2009) which also noted a coincident RH increase of 5-10%.

Unfortunately, we were unable to investigate in detail the backscatter-RH relationship of the CALIPSO Level 2 532 nm backscatter profiles. However, we present some of the initial findings below of work that we hope to continue over the next year. For an entire day of night observations, we graphically looked at the relationship between RH and the CALIPSO Level 2 5 km Profile backscatter (presented as log) observation. The histograms and scattergrams for the 1 km level is provided in, respectively, Figures 23 and 24. No real relationship or difference is noted in the histograms for different RH bins. This was true for all levels and also when broken down into regions such as the tropics and mid latitudes. However, the scattergrams hint at the relationship of higher backscatter values with higher relative humidity values, especially when there were clouds above that level. Much more work has to be done in this area and it is likely that the correlation between RH and backscatter is much more apparent and obvious when dealing with the individual shot Level 1 backscatter data rather than the averaged 5 Km profiles.

4. Summary and Discussion

4.1 Cloud Cover and Ground Detection

Analysis of the CALIPSO Level 2 Cloud layer products for the 1 km and 5 km resolution show global cloud cover of 67-71% (and 45 -50% for the 333 m resolution), very similar to previous results from AIRS, GLAS and LITE. When clouds are present within the resolution distance, ~ 75% of the time there was just one cloud layer reported. For the 333 m and 1 km resolutions, more than two cloud layers existed only 2-5 % of the time. However, this increased to over 20% for the 5 km resolution, a result similar to the GLAS medium resolution findings.

Higher cloud cover percentages for all three resolutions were found over open water, with the larger differences occurring at night. Not surprisingly, ground returns were higher over land for all resolutions.

Ground detection statistics show that, for the 1 and 5 km resolution products, 55 – 65 % of the products had ground detection. In addition, 35 – 50 % of the shots that hit clouds, also hit the ground. Both these results were similar to previous LITE findings. However, for the single shot 333 m product, only 10 -20 % of the products that hit cloud also hit the ground. The fact that ~60% of the 1 km integrations included a ground return (including cloudy areas) bodes well for a space-based DWL that integrates over similar distances and only needs a few of the integrated samples to make a useful measurement (e.g. coherent detection).

4.2 CFLOS/PASS THROUGH – Integration Distance, EAP, DWL Trades

Utilizing the CALIPSO Level 2 Cloud Layer 1 Km product, we computed CFLOS and "pass through" (if the shot made it through to a lower level) statistics for various trades of integrations distance and efficiency requirements. Universally we found that, taken individually, integration distance (25 km to 50 km to 75 km) makes little impact on the percentage of occurrence of CFLOS or "pass through". Put another way, it is more advantageous to increase the energy or clear air performance rather than counting on integrating longer to obtain the number of photons needed to get the accuracy we desire. Thus, it is more efficient to design to, say, 50% cloud cover (rather than clear air) and keep the integration distance limited to reduce spread in the returns due to LOS velocity variability.

4.3 Backscatter Modeling, PDFs and Wavelength Conversion

The conversion of backscatter coefficients measured by CALIPSO at .532 µm and 1.064 µm to the GWOS wavelengths of .355 and 2.06 µm were done using a scattering model residing at the University of Alabama, Huntsville and the six aerosol types suggested by Omar (2009). The most critical GWOS wavelength with aerosol backscatter issues is the 2 µm used by the coherent detection subsystem. The wavelength conversion to .355 is less critical since direct detection channel relies on the molecular backscatter with aerosol attenuation (accuracy) being a secondary concern. The conclusion we reach is that the OSSEs conducted to date have used 2 µm backscatter coefficients that are ~ 2 -7 times lower than modeled with the CALIPSO aerosol types. Note that these are model results and not direct measurements. However, prior modeling was done using more simplistic and less realistic aerosol characterization.

4.4 Backscatter and Validation of backscatter used in DLSM/NRs/OSSEs

Our investigation into the global distribution of backscatter in terms of PDFs at various altitudes and latitudes met with only partial success. The limiting factor was the threshold sensitivity of the CALIPSO sensors. Given those limitations, we can only state that the GWOS as currently designed will have sufficient aerosol returns at 1000m to make a measurement 30% of the time; less frequently above that level and more frequently at lower altitudes. This is encouraging (we have been assuming only 25% success rate) but it is not as definitive as we had hoped. It does mean that we have been conservative with our modeling DWL data coverage and thus any improvement in our defense of more advantageous backscatter would only improve the modeled data coverage and weather model impacts.

5. References

Berthier, S., P. Chazette, J. Pelon and B. Baun, 2008: Comparison of cloud statistics from spaceborne lidar systems, Atmos. Chem. Phys., 8, 6965-6977

Emmitt, G.D. and S. Greco, 2006: Using ICESAT observations to obtain CFLOS statistics for use in the design of space-based lidars (invited paper), SPIE Europe Remote Sensing, Stockholm, Sweden, September 11 – 14.

Ferrare, R. and others, 2009: Observations of Aerosols Near Clouds during CHAPS/CLASIC, Proceedings of the ASP_ST meeting.

Lamquin, N., K. Gierens, C.J. Stubenrauch and R. Chaterjee, 2009: Evaluation of upper tropospheric humidity forecasts from ECMWF using AIRS and CALIPSO data, Atmos. Chem. Phys., 9,1779 -1793

Omar, A., D. Winker, C. Kittaka, M. Vaughan, Z. Liu, Y. Hu, C. Trepte, R. Rogers, R. Ferrare, R. Kuehn, C. Hostetler, 2009: "The CALIPSO Automated Aerosol Classification and Lidar Ratio Selection Algorithm", *J. Atmos. Oceanic Technol.*, **26**, 1994-2014, doi:10.1175/2009-JTECHA1231.1.

Reinke, D.L., J.M. Forsythe, K.E. Milberger and T.H. Vonder Haar, 2010: Probability of cloud-free line of sight (PCFLOS) derived from CloudSat cloud profiling radar (CPR) and coincident CALIPSO lidar data, 17th Conference on Satellite Meteorology and Oceanography, September 2010.

Rogers, R.R., C.A. Hostetler, J.W. Hair, R.A. Ferrare, Z. Liu, M.D. Obland, D.B. Harper, A.L. Cook, K.A. Powell, M.A. Vaughan and D.M. Winker, 2011: Assessment of the CALIPSO Lidar 532nm attenuated backscatter calibration using the NASA airborne High Spectral Resolution Lidar, Atmos. Chem. Phys., 11, 1295-1311

Stubenrauch, C.J., S. Cros, A. Guginard and N. Lamquin, 2010: A 6-year global cloud climatology from the Atmospheric InfraRed Sounder AIRS and a statistical analysis in synergy with CALIPSO and CloudSat, Atmos. Chem. Phys. Discuss., 10, 8247-8296

Su, W., G.L. Schuster, N.G. Loeb, R.R. Rogers, R.A. Ferrare, C.A. Hostetler, J.W. Hair and M.D. Obland, 2008: Aerosol and cloud interaction observed from high spectral resolution lidar data, JOURNAL OF GEOPHYSICAL RESEARCH, VOL. 113, D24202

Tackett, J.L. and L. Di Girolamo, 2009: Enhanced aerosol backscatter adjacent to tropical trade wind clouds revealed by satellite-based lidar, Geophys. Res. Let's, Vol. 36, LI4804,

Twohy, C.H., J.A. Coakley and W.R. Tahnk, 2009: Effect of changes in relative humidity on aerosol scattering near clouds, Jour. of Geophys. Res., Vol 114, D05205

Werner, C., 1972: Lidar measurement of atmospheric aerosol as a function of relative humidity, Optical and Quantum Electronics, Vol. 4, No. 2, 125-132.

Winker, D.., J. Pelon, J.A. Coakley, S.A. Ackerman, R.J. Charlson, P.R. Colarco, P. Flamant, Q. Fu, R.M. Hoff, C. Kittaka, T.L. Kubar, H. Le Treut, M.P. Mccormick, G. Megie, L. Poole, K. Powell, C. Trepte, M.A. Vaughn and B.A. Wielicki, 2010: THE CALIPSO MISSION A Global 3D View of Aerosols and Clouds, Bulletin of the Amer. Meteo. Soc., September 2010, 1211-1228.

Wood, S., G. Emmitt and S. Greco, 2000: DLSM: A coherent and direct detection lidar simulation model for simulating space-based and aircraft-based lidar winds. Proceedings SPIE's 14th Annual Internat. Symp. Aerospace Defense Sensing, Simulation and Controls, Orlando , FL , April.

6. TABLES

Condition		333 m	1 km	5km	
Cloud		44.4	67.8	69.0	
No Cloud		55.6	32.2	31.0	
Hit Ground		47.0	63.6	66.6	
No Ground		53.0	36.4	33.4	
No Cloud		55.6	32.2	31.0	
1 cloud Layer		35.7 (80.3)	51.2 (75.5)	37.5 (54.4)	
2 cloud layers		6.4 (14.5)	14.7 (21.7)	17.1 (24.9)	
>2 cloud layers		2.3 (5.2)	1.9 (2.8)	14.3 (20.8)	
Cloud and Ground		7.9	30.6	35.8	
No Cloud and Ground		39.1	33.0	30.8	
Cloud and No Ground		36.5	37.2	33.1	
No Cloud and No Ground		16.4	0.1	0.2	
Percent of cloud that hit ground		17.8	45.1	51.9	

Table 1: Cloud and ground detection statistics from the CALIPSO Level 2 cloud layer products for 333m, 1km, and 5km resolution for Aug 11-12, 2007 (Night only). Numbers in parentheses reflect cases where there were clouds.

Condition		333 m	1 km	5km	
Cloud		48.3	69.3	71.3	
No Cloud		51.7	30.7	28.7	
Hit Ground		34.5	52.3	55.7	
No Ground		65.5	47.7	44.3	
No Cloud		51.7	30.7	28.7	
1 cloud Layer		39.5 (81.7)	53.9 (77.8)	39.9 (55.9)	
2 cloud layers		6.5 (13.6)	13.6 (19.6)	16.5 (23.1)	
>2 cloud layers		2.3 (4.7)	1.8 (2.6)	14.9 (21.0)	
Cloud and Ground		4.4	21.8	27.1	
No Cloud and Ground		30.1	30.6	28.6	
Cloud and No Ground		43.9	47.5	44.2	
No Cloud and No Ground		21.6	0.1	0.1	
Percent of cloud that hit ground		9.1	31.5	38.1	

Table 2: Cloud and ground detection statistics from the CALIPSO Level 2 cloud layer products for 333m, 1km, and 5km resolution for Aug 11-12, 2007 (Day only). Numbers in parentheses reflect cases where there were clouds.

Condition	ALL	Water	Land
Cloud	44.4	55.6	30.4
No Cloud	55.6	44.4	69.6
Hit Ground	47.0	30.3	62.8
No Ground	53.0	69.7	37.2
No Cloud	55.6	44.4	69.6
1 cloud Layer	35.7	45.4	26.0
2 cloud layers	6.4	7.5	3.8
>2 cloud layers	2.3	2.8	0.6
Cloud and Ground	7.9	7.0	4.6
No Cloud and Ground	39.1	23.3	58.1
Cloud and No Ground	36.5	48.6	25.7
No Cloud and No Ground	16.4	21.1	11.5
Percent of cloud that hit ground	17.8	12.6	15.2

Table 3a: Cloud statistics over different surfaces for the CALIPSO Level 2 cloud layer 333 m product on Aug 11-12, 2007. Night Observations.

Condition	ALL	Water	Land
Cloud	48.3	52.5	37.6
No Cloud	51.7	47.5	62.4
Hit Ground	34.5	28.1	49.1
No Ground	65.5	71.9	50.9
No Cloud	51.7	47.5	62.4
1 cloud Layer	39.5	42.5	32.4
2 cloud layers	6.5	7.3	4.3
>2 cloud layers	2.3	2.7	0.9
Cloud and Ground	4.4	4.8	2.9
No Cloud and Ground	30.1	23.3	46.2
Cloud and No Ground	43.9	47.8	34.7
No Cloud and No Ground	21.6	24.2	16.2
Percent of cloud that hit ground	9.1	9.1	7.8

Table 3b: Cloud statistics over different surfaces for the CALIPSO Level 2 cloud layer 333 m product on Aug 11-12, 2007. Day Observations.

Condition	ALL	Water	Land
Cloud	67.8	77.5	52.0
No Cloud	32.2	22.5	48.0
Hit Ground	62.7	52.2	68.3
No Ground	37.3	47.8	31.7
No Cloud	32.2	22.5	48.0
1 cloud Layer	51.2	58.5	36.6
2 cloud layers	14.7	16.9	13.5
>2 cloud layers	1.9	2.2	2.0
Cloud and Ground	30.6	29.9	20.6
No Cloud and Ground	32.1	22.4	47.8
Cloud and No Ground	37.2	47.6	31.5
No Cloud and No Ground	0.1	0.1	0.2
	45.1	38.5	39.5

Table 4a: Cloud statistics over different surfaces for the CALIPSO Level 2 cloud layer 1 km product on Aug 11-12, 2007. Night Observations.

Condition	ALL	Water	Land
Cloud	69.3	73.2	59.8
No Cloud	30.7	26.8	40.2
Hit Ground	52.3	49.3	58.3
No Ground	47.7	50.7	41.7
No Cloud	30.7	26.8	40.2
1 cloud Layer	53.9	56.6	47.2
2 cloud layers	13.6	14.6	11.3
>2 cloud layers	1.8	2.0	1.2
Cloud and Ground	21.8	22.6	18.4
No Cloud and Ground	30.6	26.7	39.6
Cloud and No Ground	47.5	50.6	41.4
No Cloud and No Ground	0.1	0.1	0.3
	31.5	30.9	30.8

Table 4b: Cloud statistics over different surfaces for the CALIPSO Level 2 cloud layer 1 km product on Aug 11-12, 2007. Day Observations.

Condition	ALL	Water	Land
Cloud	69.0	73.3	59.4
No Cloud	31.0	26.7	40.6
Hit Ground	66.7	57.3	72.1
No Ground	33.3	42.7	27.9
No Cloud	31.0	26.8	40.6
1 cloud Layer	37.5	43.2	30.6
2 cloud layers	17.1	17.1	16.5
>2 cloud layers	14.3	13.0	12.3
Cloud and Ground	35.8	30.9	31.6
No Cloud and Ground	30.8	26.4	40.5
Cloud and No Ground	33.1	42.4	27.8
No Cloud and No Ground	0.2	0.1	0.1
Percent of cloud that hit ground	52.0	42.2	53.3

Table 5a: Cloud statistics over different surfaces for the CALIPSO Level 2 cloud layer 5 km product on Aug 11-12, 2007. Night Observations.

Condition	ALL	Water	Land
Cloud	71.2	73.3	66.6
No Cloud	28.8	26.7	33.4
Hit Ground	55.7	52.2	63.0
No Ground	44.3	47.8	37.0
No Cloud	28.8	26.7	33.4
1 cloud Layer	39.9	41.8	35.7
2 cloud layers	16.5	16.3	16.9
>2 cloud layers	15.0	15.2	13.9
Cloud and Ground	27.1	25.6	29.7
No Cloud and Ground	28.6	26.6	33.3
Cloud and No Ground	44.1	47.7	36.9
No Cloud and No Ground	0.1	0.1	0.1
Percent of cloud that hit ground	38.1	34.9	44.6

Table 5b: Cloud statistics over different surfaces for the CALIPSO Level 2 cloud layer 5 km product on Aug 11-12, 2007. Day Observations.

Altitude (m)	75 km	50 km	25 km
> 15000	89.7	92.0	95.0
10000	82.6	85.7	90.0
5000	64.8	69.2	75.5
3000	55.9	60.6	67.3
2000	49.7	54.4	61.3
500	28.8	33.2	40.6

Table 6: Percent of time where 100% of Calipso Level 2 cloud layer 1 km products pass through various atmospheric levels for 75, 50, and 25 km integration distance.

Altitude (m)	75 km	50 km	25 km
> 15000	99.0	99.0	99.0
10000	95.3	95.4	95.8
5000	82.2	83.0	84.0
3000	74.1	75.1	76.5
2000	69.0	70.0	71.6
500	49.3	50.8	53.3

Table 7: Percent of time where 80% of Calipso Level 2 cloud layer 1 km products pass through various atmospheric levels for 75, 50, and 25 km integration distance.

Altitude (m)	75 km	50 km	25 km
> 15000	99.7	99.7	99.6
10000	97.7	97.6	97.4
5000	88.8	88.7	88.3
3000	82.1	82.1	81.7
2000	77.8	77.9	77.7
500	63.2	63.2	63.2

Table 8: Percent of time where 50% of Calipso Level 2 cloud layer 1 km products pass through various atmospheric levels for 75, 50, and 25 km integration distance.

Altitude (m)	75 km	50 km	25 km
> 15000	93.2	93.8	94.5
10000	69.7	72.0	75.0
5000	49.3	52.1	56.1
3000	40.4	43.4	47.9
2000	32.0	35.1	40.1
500	11.8	13.6	17.1

Table 9: Percent of time where 100% of Calipso Level 2 cloud layer 1 km products have CFLOS down to various atmospheric levels for 75, 50, and 25 km integration distance.

Altitude (m)	75 km	50 km	25 km
> 15000	95.1	95.3	95.5
10000	76.1	77.0	78.3
5000	56.9	58.0	60.0
3000	49.9	51.0	53.1
2000	43.0	44.2	46.6
500	20.3	21.7	24.0

Table 10: Percent of time where 80% of Calipso Level 2 cloud layer 1 km products have CFLOS down to various atmospheric levels for 75, 50, and 25 km integration distance.

Altitude (m)	75 km	50 km	25 km
> 15000	96.3	96.3	96.3
10000	81.4	81.6	81.1
5000	64.1	64.4	64.1
3000	57.8	58.3	57.9
2000	52.2	52.6	52.4
500	31.5	32.0	32.6

Table 11: Percent of time where 50% of Calipso Level 2 cloud layer 1 km products have CFLOS down to various atmospheric levels for 75, 50, and 25 km integration distance.

Condition	ALL	Tropical	Mid-latitude	Polar
Cloud	69.6	66.1	72.5	70.2
No Cloud	30.4	33.9	27.5	29.8
Hit Ground	55.1	60.1	47.5	58.0
No Ground	44.9	39.9	52.5	42.0
No Cloud	30.4	33.9	27.5	29.8
1 cloud Layer	50.2 (72.1)	49.7	51.2	49.5
2 cloud layers	15.9 (22.8)	13.7	17.1	16.8
>2 cloud layers	3.6 (5.1)	2.7	4.2	3.8
Cloud and Ground	25.6	27.3	21.1	28.4
No Cloud and Ground	29.6	32.8	26.4	29.6
Cloud and No Ground	44.1	38.8	51.4	41.8
No Cloud and No Ground	0.8	1.1	1.1	0.2

Table 12: Cloud statistics over different zonal regions for the CALIPSO Level 2 cloud layer 1 km product on Aug 8-9, 2007. Numbers in parentheses reflect cases where there were clouds.

Altitude	1 km ALL	1 km TROP	1 km MID	1 km POL
> 15000	92.0	87.6	92.2	96.7
10000	85.7	74.5	88.2	96.4
5000	69.2	61.0	66.0	83.1
3000	60.6	55.8	56.4	70.9
2000	54.4	51.0	50.0	63.3
500	33.2	25.9	26.1	49.9

Table 13: Percentage of time where all (100%) of the CALIPSO Level 2 cloud layer 1 km shot products passed through a given altitude over a ~50 km distance.

Altitude (m)	1 km ALL	1 km TROP	1 km MID	1 km POL
> 15000	99.0	98.8	98.6	99.8
10000	95.4	90.7	96.7	99.7
5000	83.0	78.6	80.2	91.9
3000	75.1	74.4	70.7	82.0
2000	70.0	70.9	65.2	75.0
500	50.8	49.7	43.8	61.1

Table 14: Percentage of time where 80% of the CALIPSO Level 2 cloud layer 1 km shot products passed through a given altitude over a ~50 km distance.

Altitude (m)	1 km ALL	1 km TROP	1 km MID	1 km POL
> 15000	99.7	99.8	99.3	99.9
10000	97.6	95.0	98.3	99.9
5000	88.7	85.2	86.7	94.9
3000	82.1	81.6	77.6	87.3
2000	77.9	79.3	73.2	81.2
500	63.2	65.5	56.0	68.6

Table 15: Percentage of time where 50% of the CALIPSO Level 2 cloud layer 1 km shot products passed through a given altitude over a ~50 km distance.

Altitude (m)	1 km ALL	1 km TROP	1 km MID	1 km POL
> 15000	93.8	85.3	98.7	97.5
10000	72.0	62.0	73.5	81.8
5000	52.1	53.8	50.3	50.5
3000	43.4	44.8	42.1	41.6
2000	35.1	35.0	33.8	35.6
500	13.6	9.3	10.9	21.6

Table 16: Percentage of time where all (100%) of the CALIPSO Level 2 cloud layer 1 km shot products had a CFLOS down to a given altitude over a ~50 km distance.

Altitude (m)	1 km ALL	1 km TROP	1 km MID	1 km POL
> 15000	95.3	88.4	99.1	98.6
10000	77.0	67.2	78.8	86.1
5000	58.0	59.4	56.2	57.9
3000	51.0	54.1	49.4	48.5
2000	44.2	47.1	42.5	42.4
500	21.7	18.4	19.0	28.6

Table 17: Percentage of time where 80% of the CALIPSO Level 2 cloud layer 1 km shot products had a CFLOS down to a given altitude over a ~50 km distance.

Altitude (m)	1 km ALL	1 km TROP	1 km MID	1 km POL
> 15000	96.3	90.8	99.4	99.1
10000	81.6	73.0	83.4	88.9
5000	64.4	65.4	62.4	64.6
3000	58.3	61.6	56.7	54.9
2000	52.6	56.5	51.2	48.8
500	32.0	33.3	28.7	34.4

Table 18: Percentage of time where 50% of the CALIPSO Level 2 cloud layer 1 km shot products had a CFLOS down to a given altitude over a ~50 km distance.

Three primary classes of aerosols

Particle Size Class	Angstrom Exponent Ratio	Backscatter Coefficient Ratio
Fine (dust, marine, dry smoke)	-2.18	.055
Coarse natural (marine, continental)	-1.32	.175
Coarse polluted (smoke, etc.)	-1.0	1.0

General derivations of backscatter at 2.01 um from observations at .532 um
Example: Beta 2.01 = (2.01/.532)^-2.22 *Beta .532 = .055 *Beta .532

Table 19: Angstrom exponent ration and backscatter coefficient ratio at 2 microns for three primary classes of aerosols.

7. FIGURES

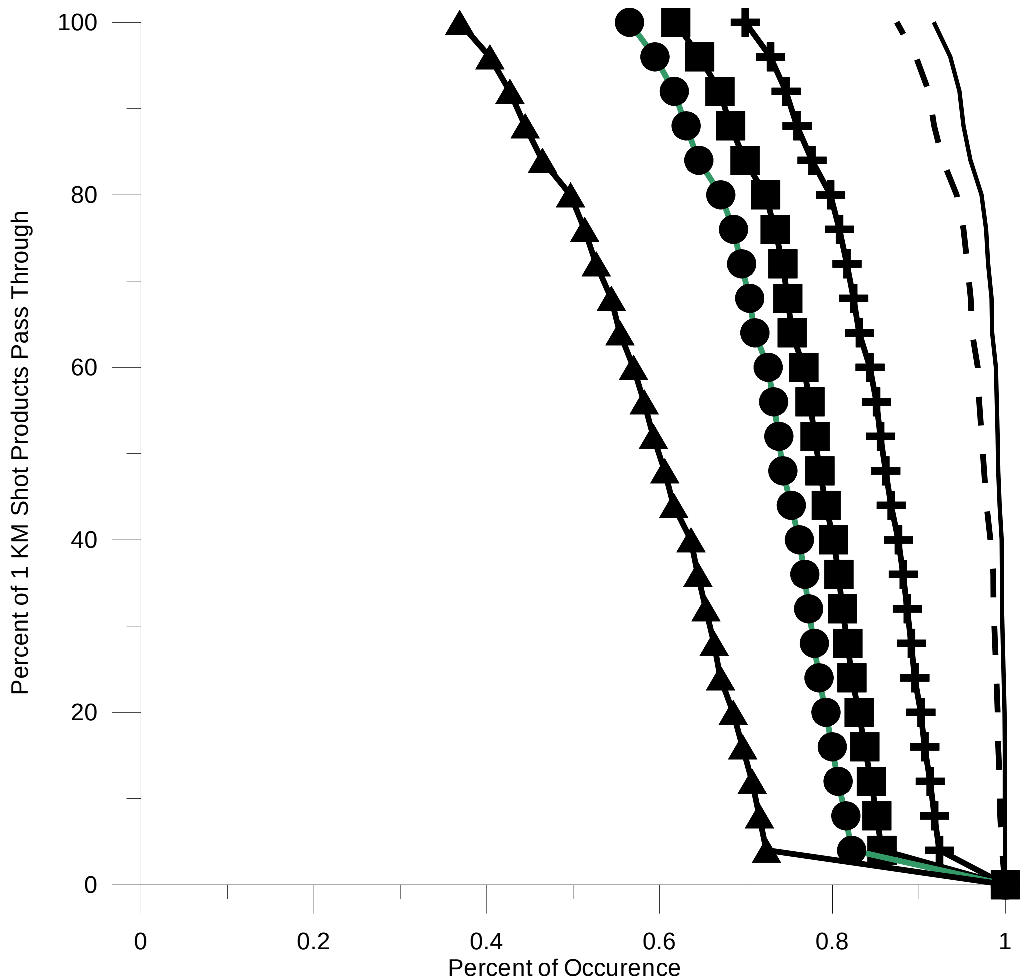

Figure 1: Initial Pass Through of CALIPSO Level 2 1 km product utilizing a 25 km integration distance for various levels in the atmosphere on August 8, 2007. Solid line is for above15 km; Dashed line = 10 km; Plus sign = 5 km; Square = 3 km; Circle = 2 km; Triangle = 500 m.

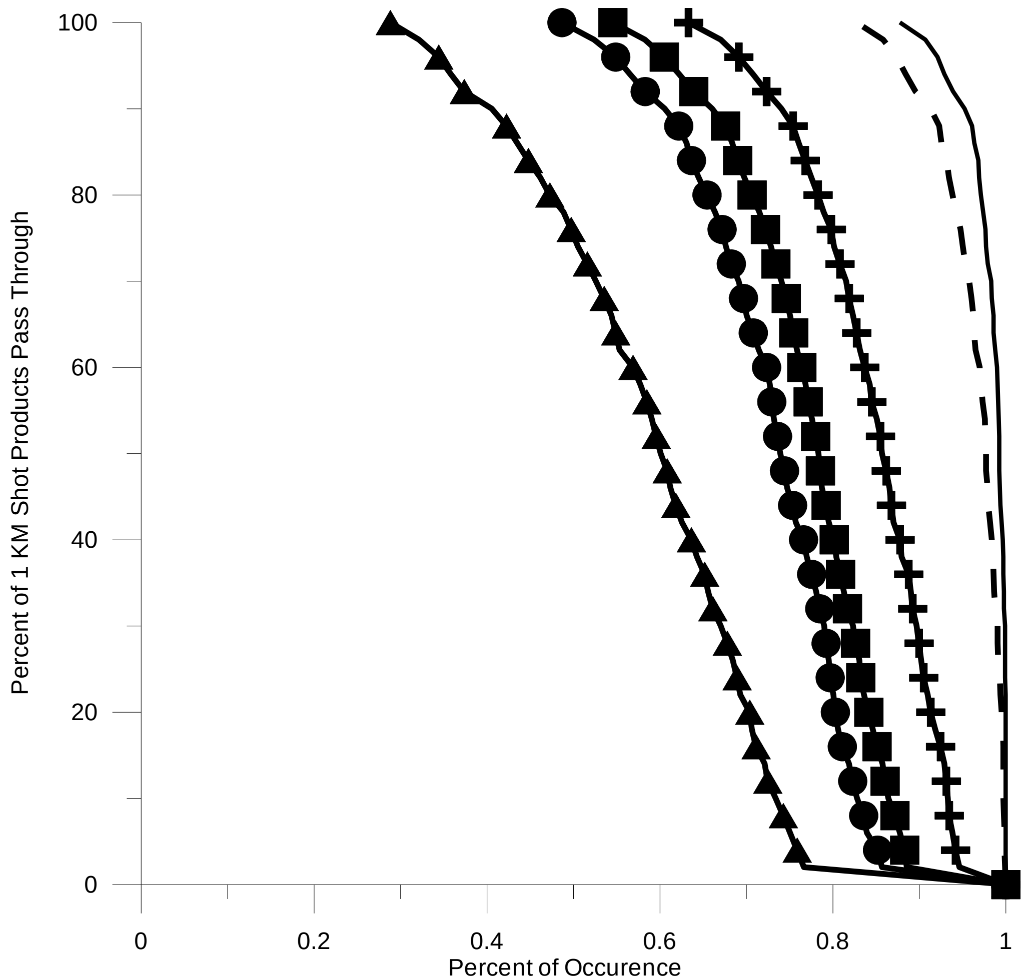

Figure 2: Initial Pass Through of CALIPSO Level 2 1 km product utilizing a 50 km integration distance for various levels in the atmosphere on August 8, 2007. Solid line is for above15 km; Dashed line = 10 km; Plus sign = 5 km; Square = 3 km; Circle = 2 km; Triangle = 500 m.

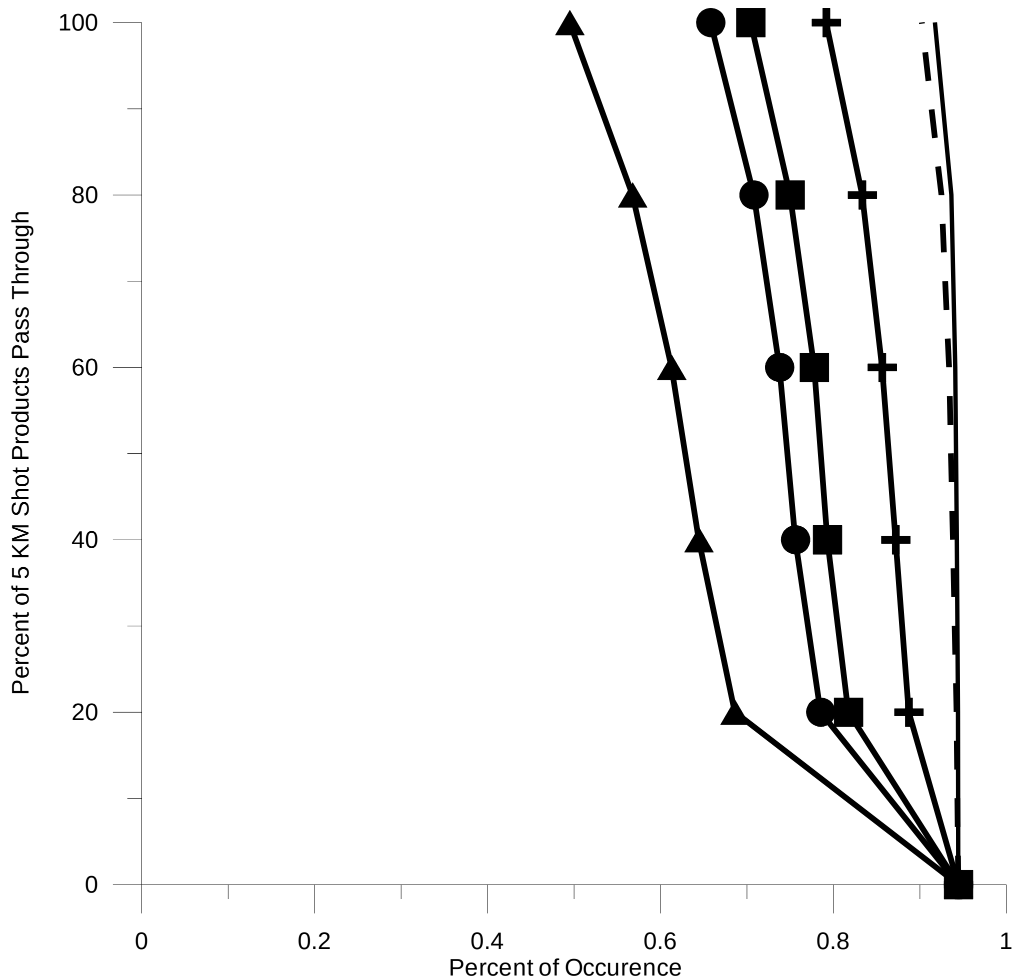

Figure 3: Initial Pass Through of CALIPSO Level 2 5 km product utilizing a 25 km integration distance for various levels in the atmosphere on August 8, 2007. Solid line is for above15 km; Dashed line = 10 km; Plus sign = 5 km; Square = 3 km; Circle = 2 km; Triangle = 500 m.

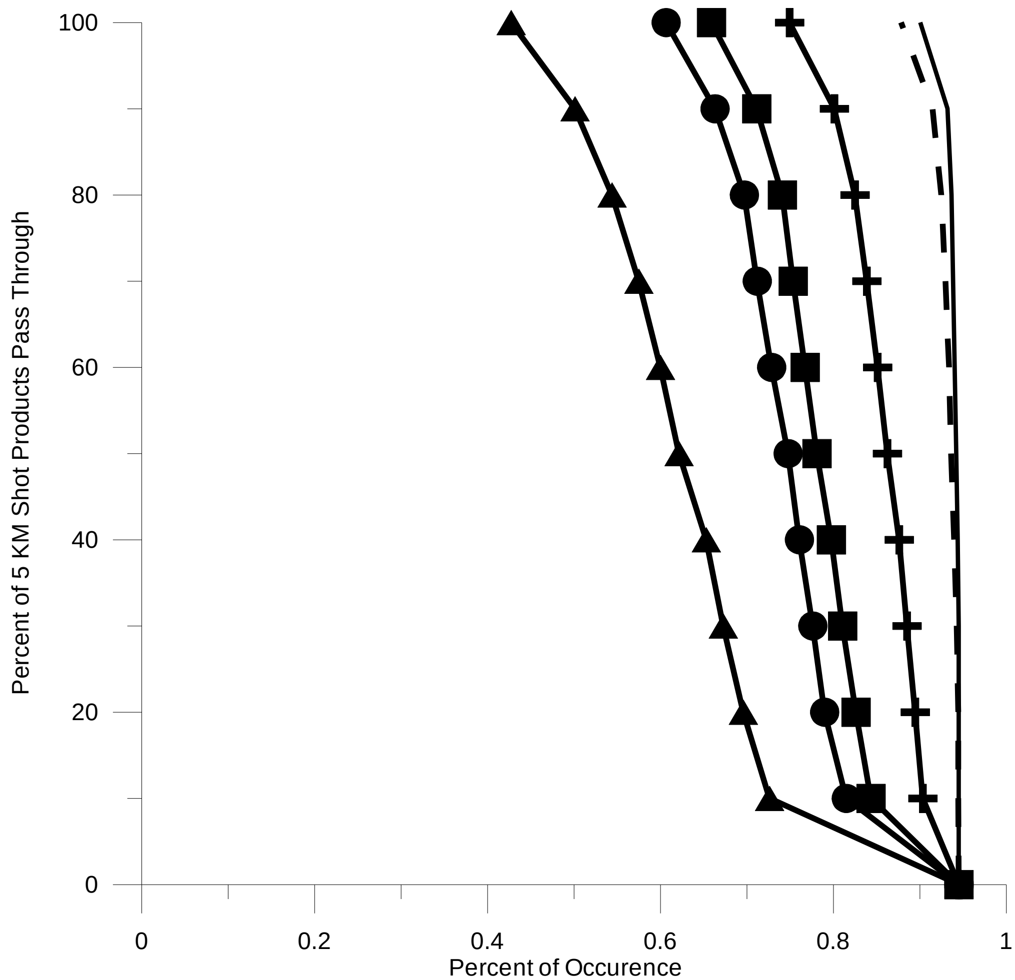

Figure 4: Initial Pass Through of CALIPSO Level 2 5 km product utilizing a 50 km integration distance for various levels in the atmosphere on August 8, 2007. Solid line is for above15 km; Dashed line = 10 km; Plus sign = 5 km; Square = 3 km; Circle = 2 km; Triangle = 500 m.

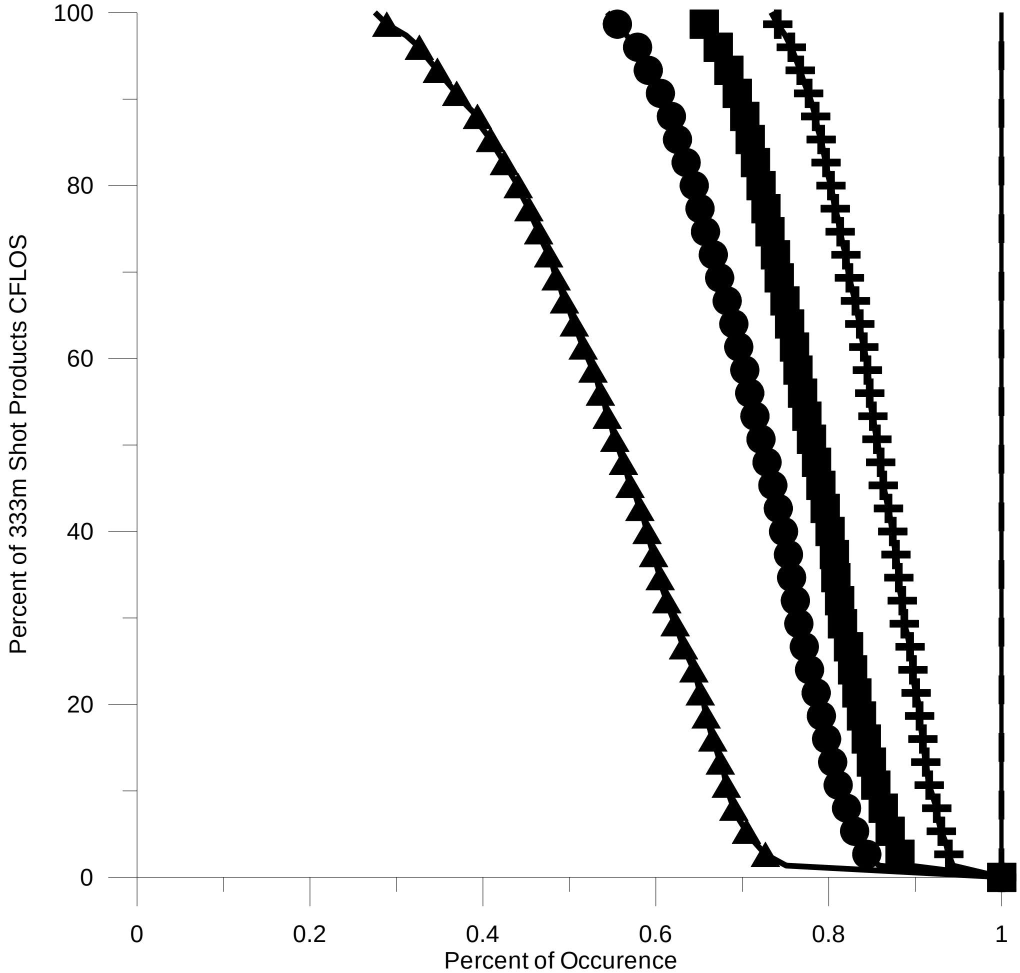

Figure 5: Initial CFLOS of CALIPSO Level 2 333 m product utilizing a 25 km integration distance for various levels in the atmosphere on August 8, 2007. Solid line is for above15 km; Dashed line = 10 km; Plus sign = 5 km; Square = 3 km; Circle = 2 km; Triangle = 500 m.

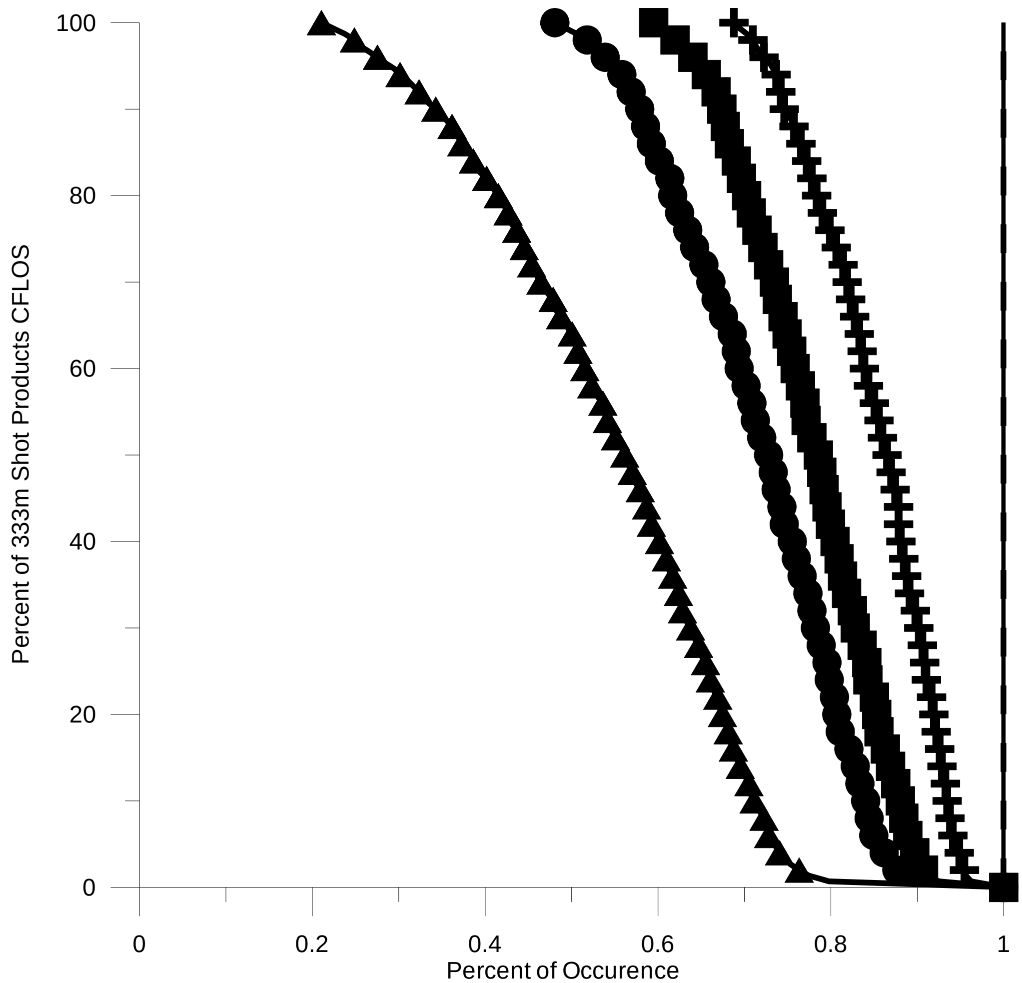

Figure 6: Initial CFLOS of CALIPSO Level 2 333 m product utilizing a 50 km integration distance for various levels in the atmosphere on August 8, 2007. Solid line is for above15 km; Dashed line = 10 km; Plus sign = 5 km; Square = 3 km; Circle = 2 km; Triangle = 500 m.

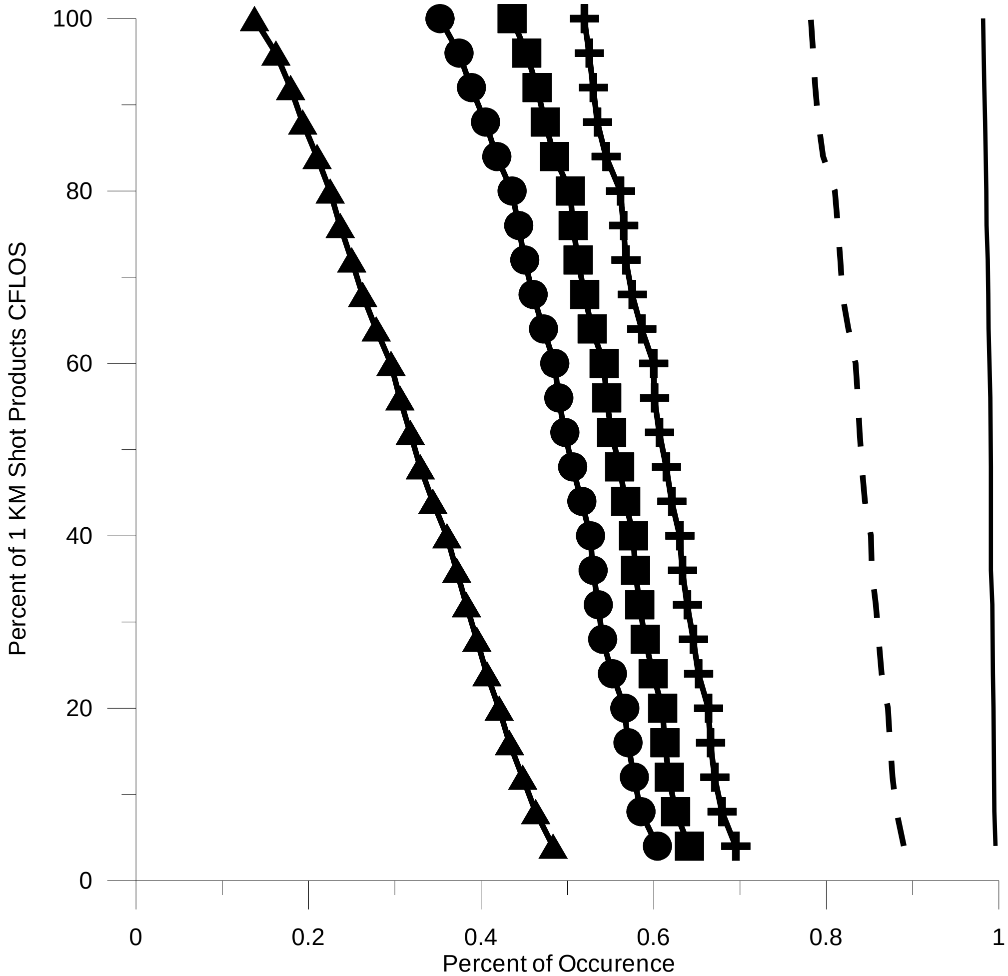

Figure 7: Initial CFLOS of CALIPSO Level 2 1 km product utilizing a 25 km integration distance for various levels in the atmosphere on August 8, 2007. Solid line is for above15 km; Dashed line = 10 km; Plus sign = 5 km; Square = 3 km; Circle = 2 km; Triangle = 500 m.

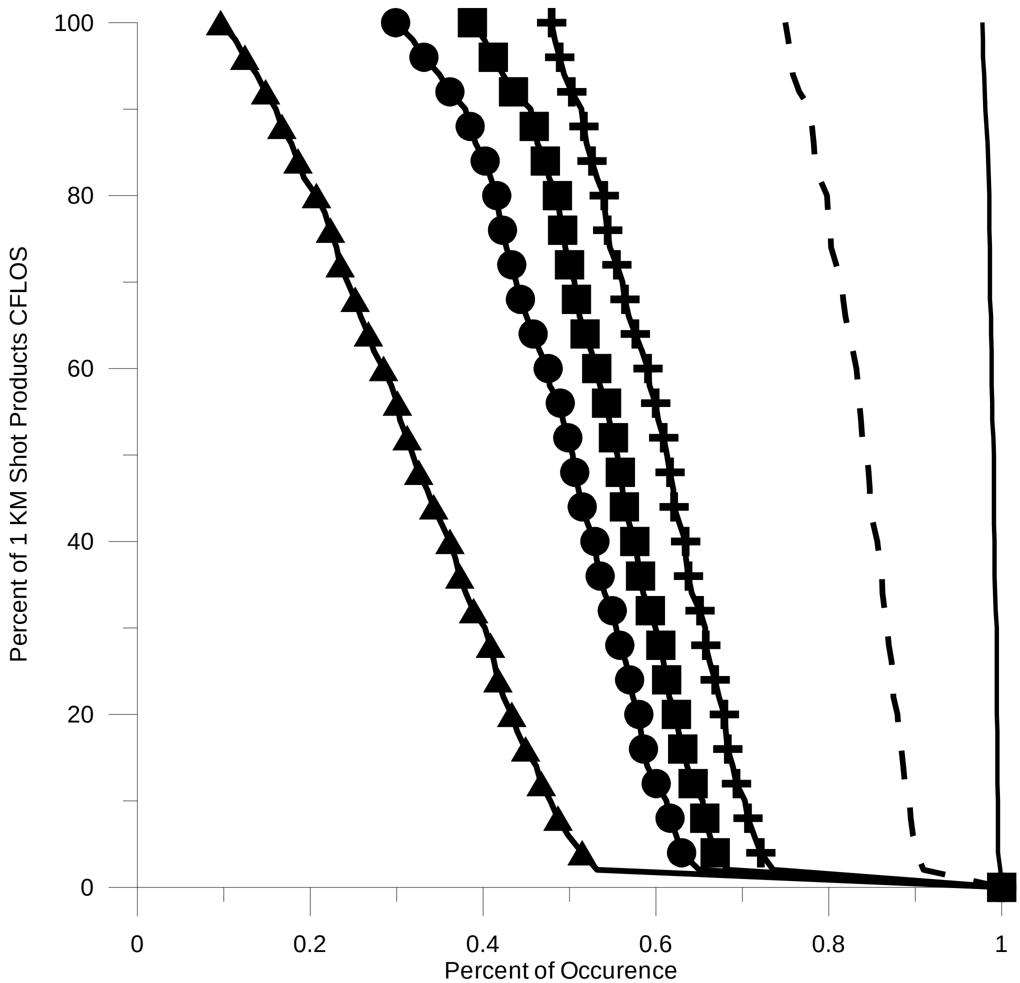

Figure 8: Initial CFLOS of CALIPSO Level 2 1 km product utilizing a 50 km integration distance for various levels in the atmosphere on August 8, 2007. Solid line is for above15 km; Dashed line = 10 km; Plus sign = 5 km; Square = 3 km; Circle = 2 km; Triangle = 500 m.

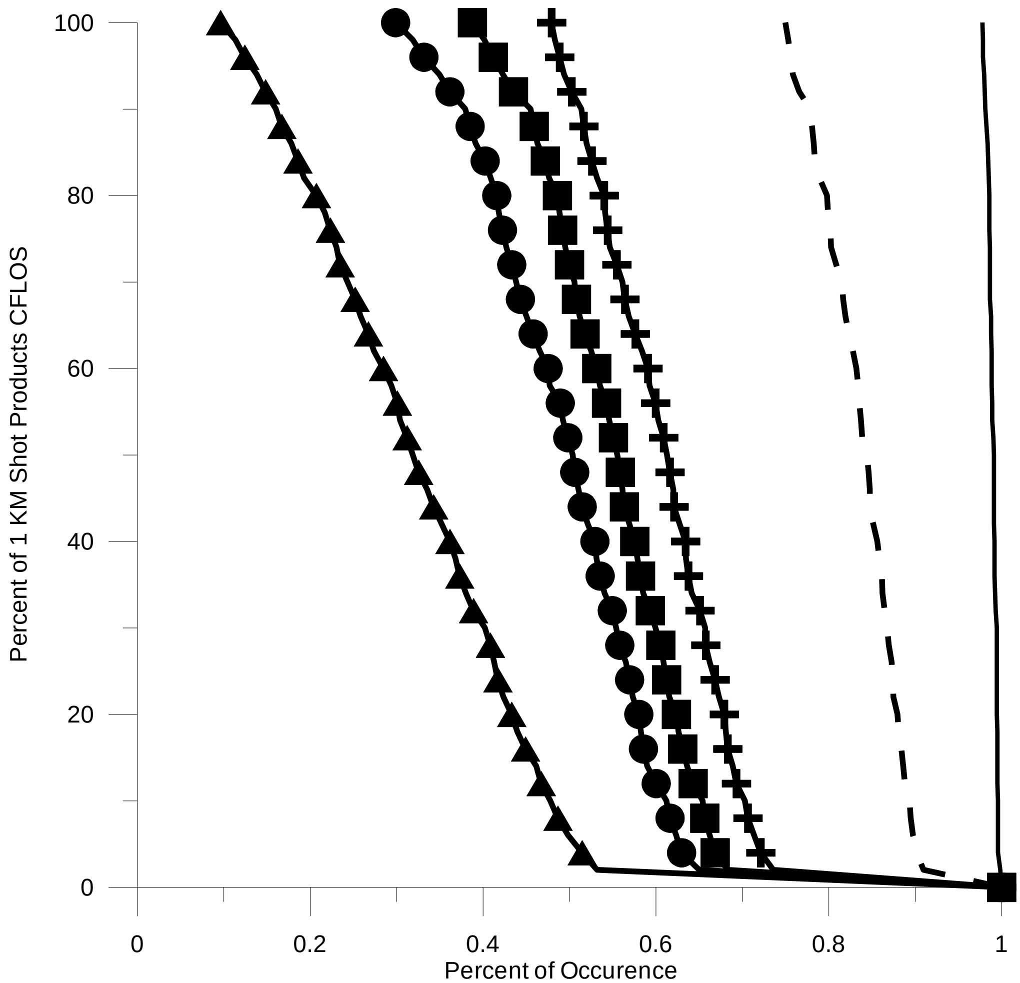

Figure 9: Initial CFLOS of CALIPSO Level 2 5 km product utilizing a 25 km integration distance for various levels in the atmosphere on August 8, 2007. Solid line is for above15 km; Dashed line = 10 km; Plus sign = 5 km; Square = 3 km; Circle = 2 km; Triangle = 500 m.

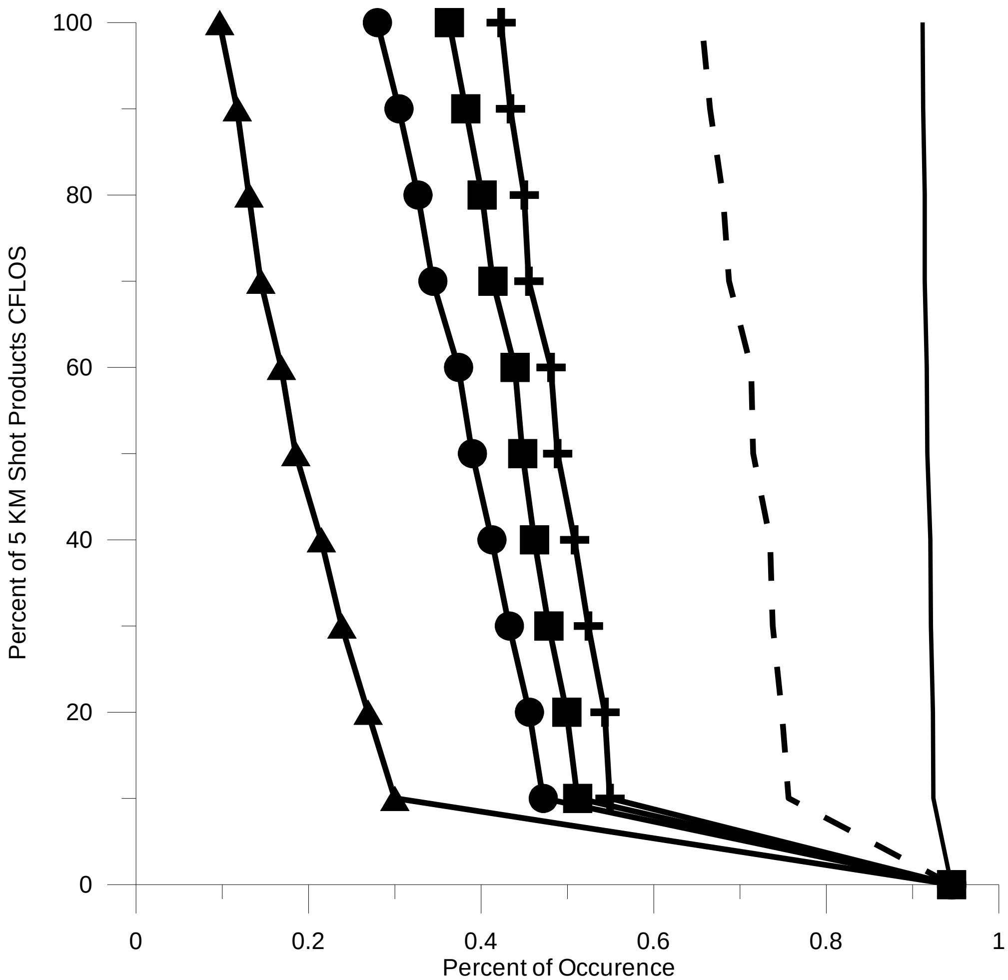

Figure 10: Initial CFLOS of CALIPSO Level 2 5 km product utilizing a 50 km integration distance for various levels in the atmosphere on August 8, 2007. Solid line is for above15 km; Dashed line = 10 km; Plus sign = 5 km; Square = 3 km; Circle = 2 km; Triangle = 500 m.

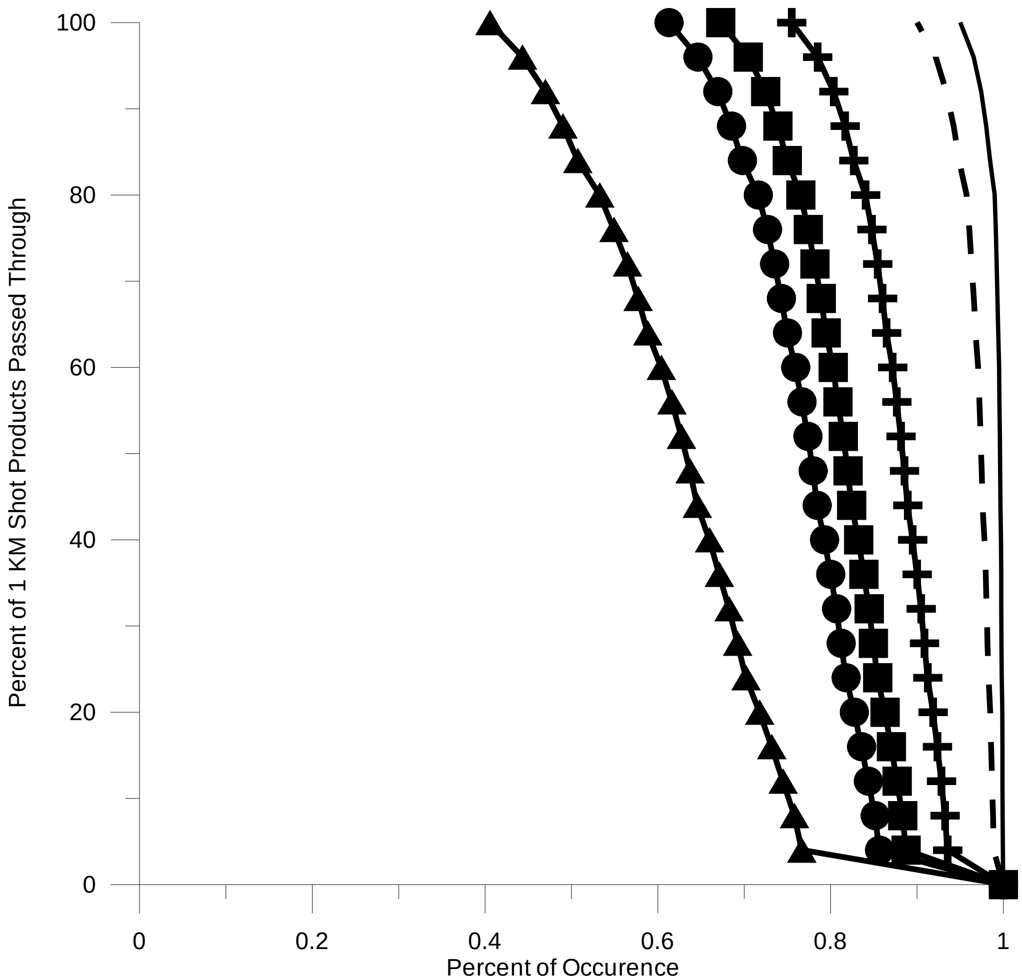

Figure 11: Pass Through of CALIPSO Level 2 1 km product utilizing a 25 km integration distance for various levels in the atmosphere on August 8-9, 2007. Solid line is for above15 km; Dashed line = 10 km; Plus sign = 5 km; Square = 3 km; Circle = 2 km; Triangle = 500 m.

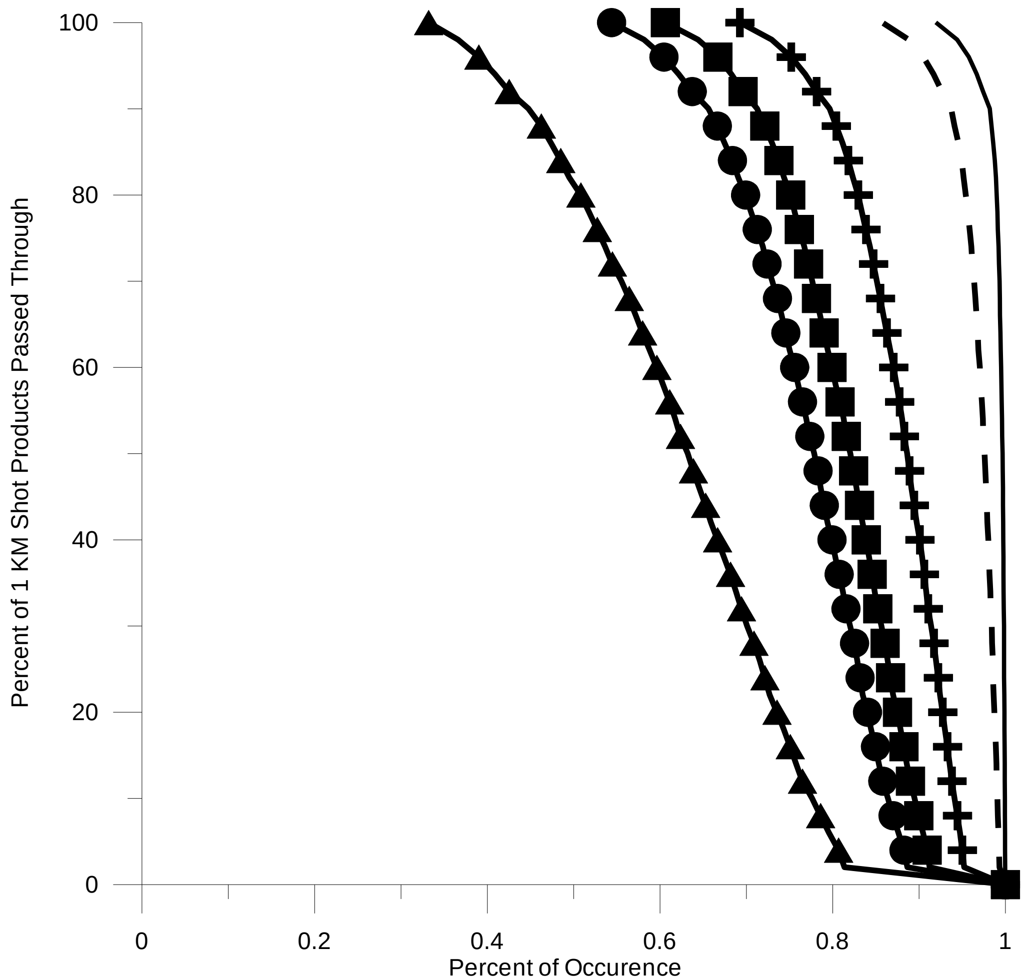

Figure 12: Pass Through of CALIPSO Level 2 1 km product utilizing a 50 km integration distance for various levels in the atmosphere on August 8-9, 2007. Solid line is for above15 km; Dashed line = 10 km; Plus sign = 5 km; Square = 3 km; Circle = 2 km; Triangle = 500 m.

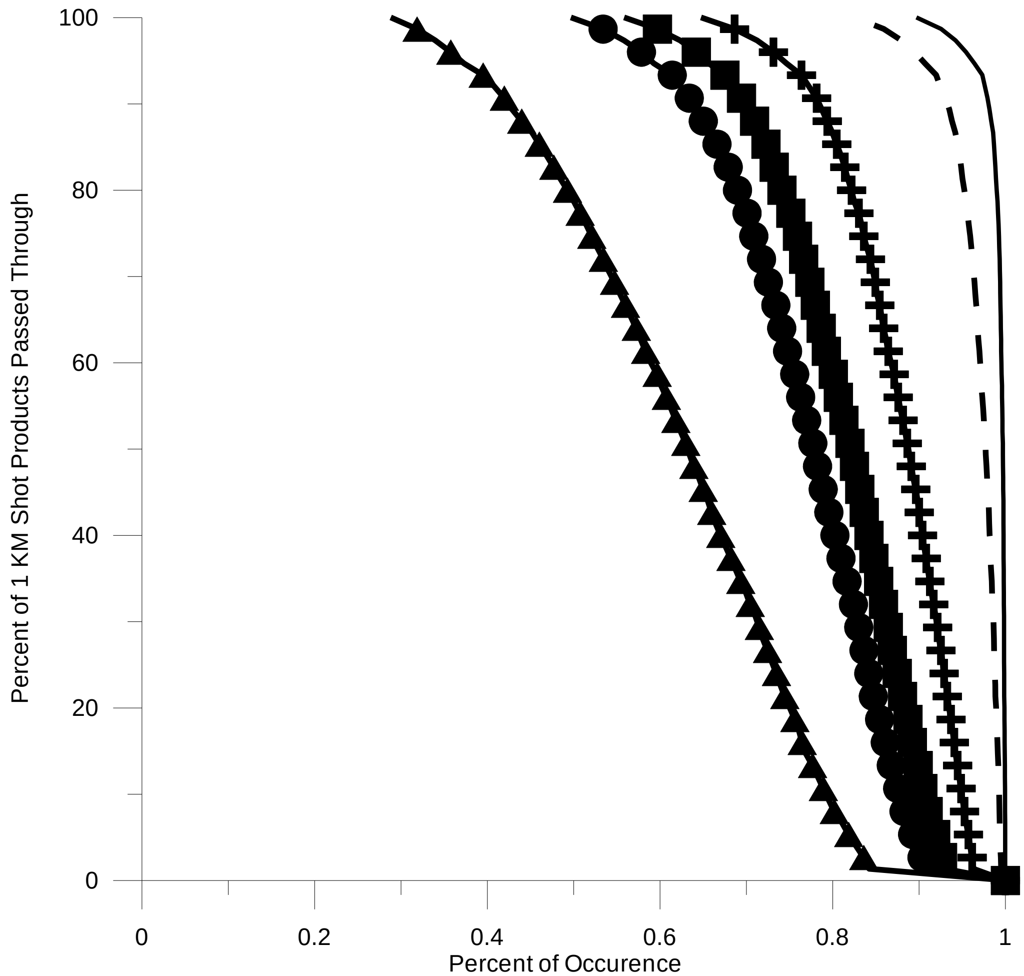

Figure 13: Pass Through of CALIPSO Level 2 1 km product utilizing a 75 km integration distance for various levels in the atmosphere on August 8-9, 2007. Solid line is for above15 km; Dashed line = 10 km; Plus sign = 5 km; Square = 3 km; Circle = 2 km; Triangle = 500 m.

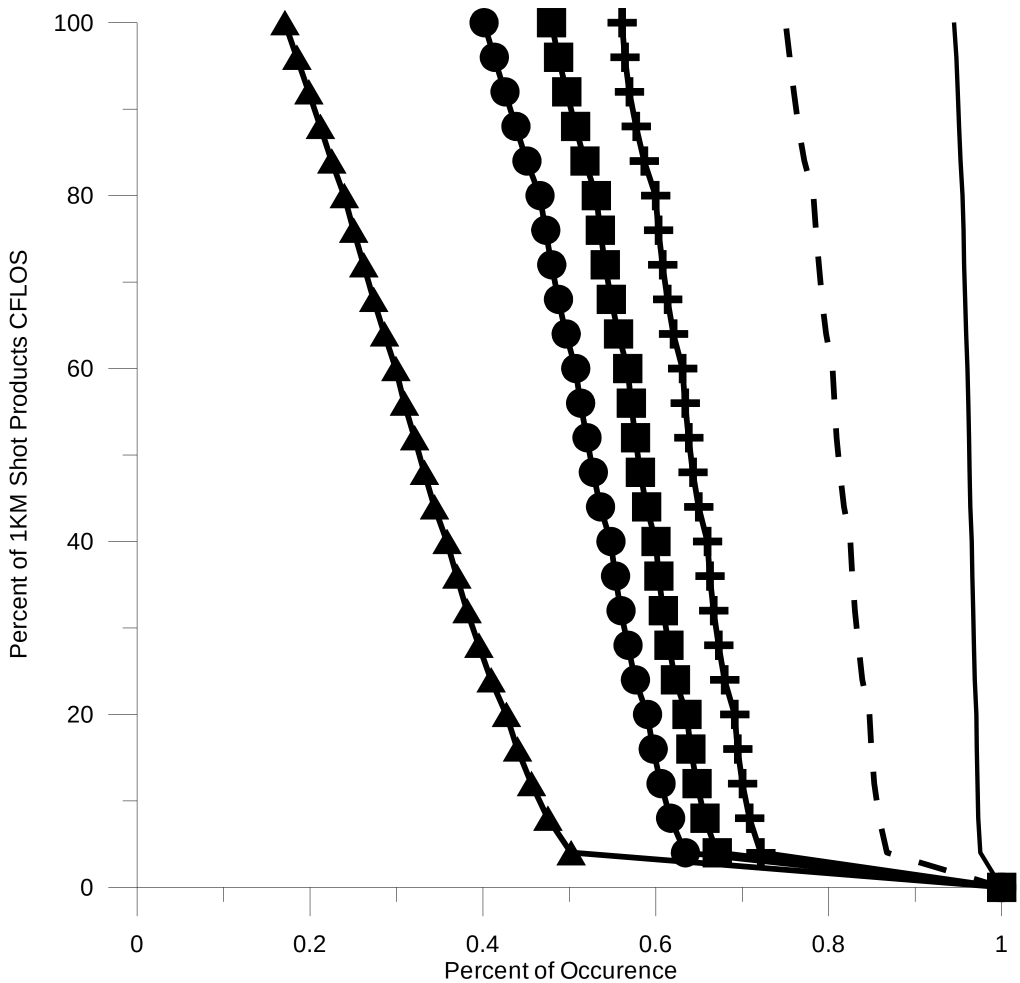

Figure 14: CFLOS of CALIPSO Level 2 1 km product utilizing a 25 km integration distance for various levels in the atmosphere on August 8-9, 2007. Solid line is for above15 km; Dashed line = 10 km; Plus sign = 5 km; Square = 3 km; Circle = 2 km; Triangle = 500 m.

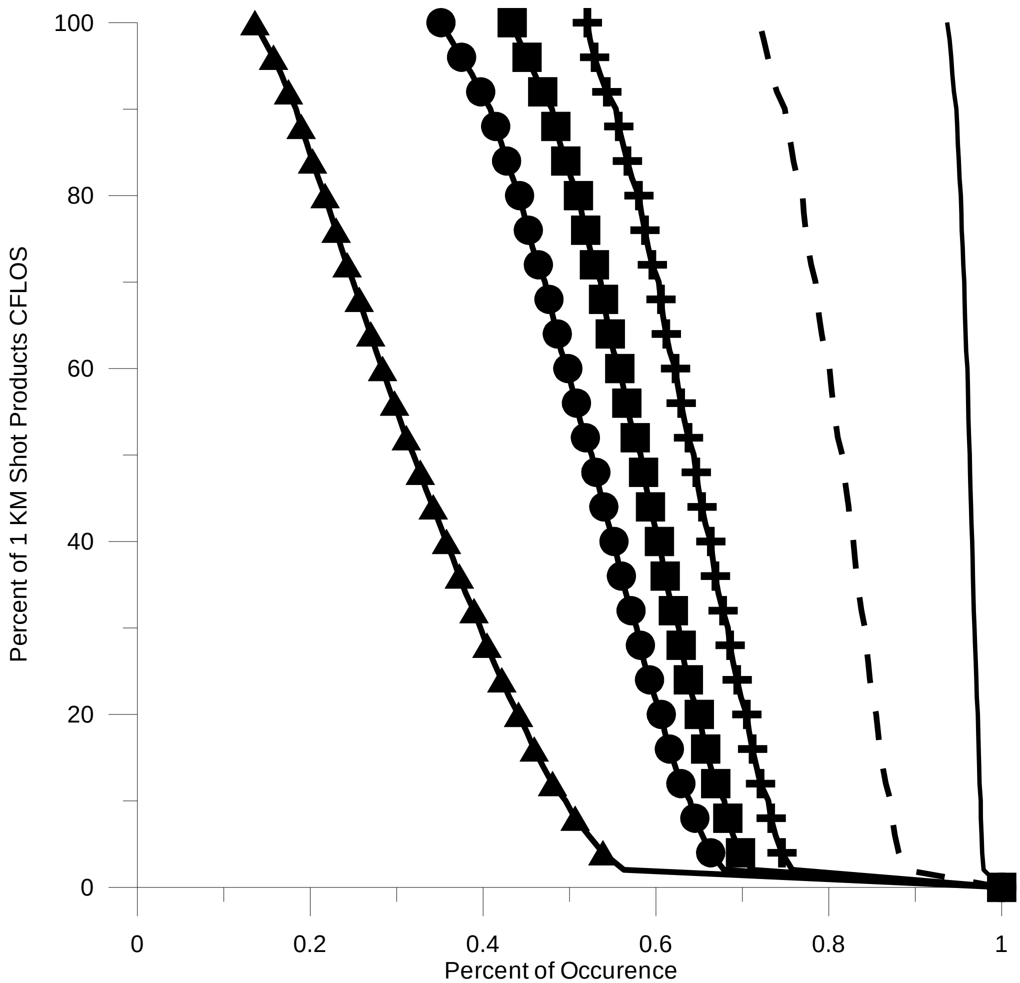

Figure 15: CFLOS of CALIPSO Level 2 1 km product utilizing a 50 km integration distance for various levels in the atmosphere on August 8-9, 2007. Solid line is for above15 km; Dashed line = 10 km; Plus sign = 5 km; Square = 3 km; Circle = 2 km; Triangle = 500 m.

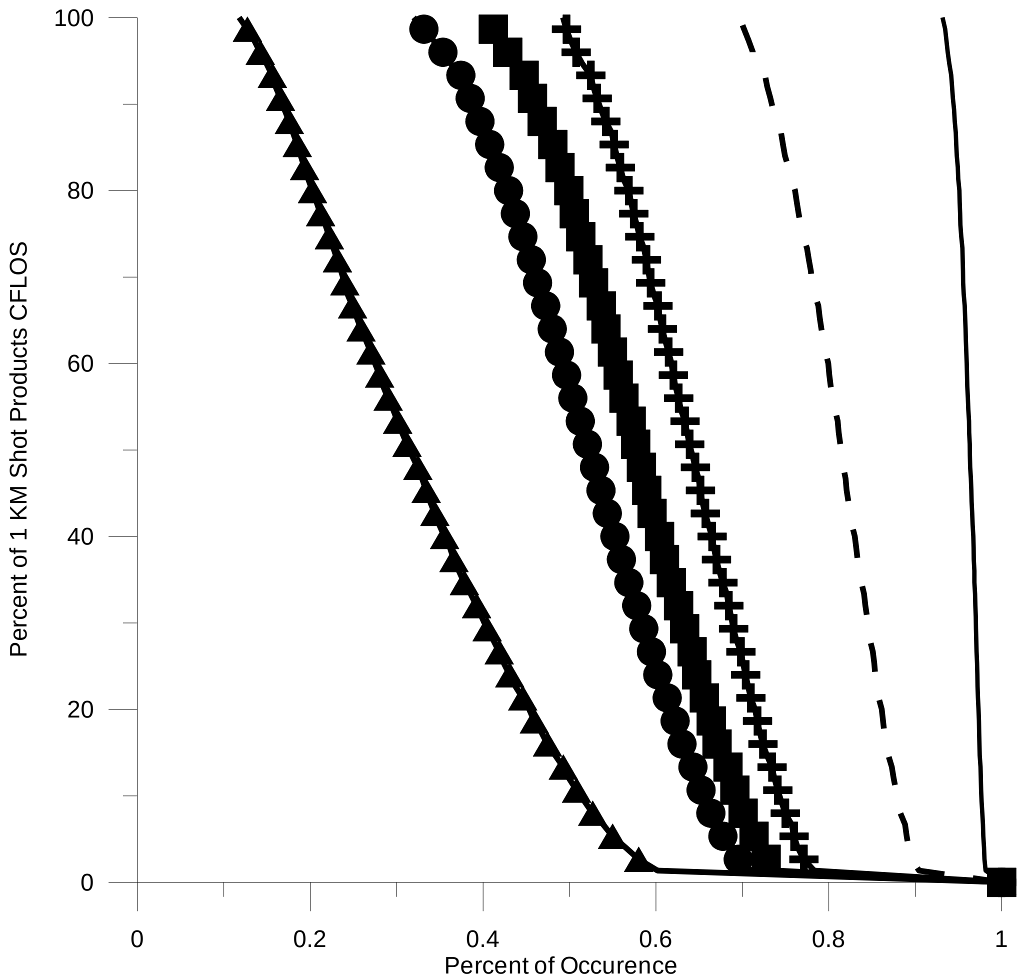

Figure 16: CFLOS of CALIPSO Level 2 1 km product utilizing a 75 km integration distance for various levels in the atmosphere on August 8-9, 2007. Solid line is for above15 km; Dashed line = 10 km; Plus sign = 5 km; Square = 3 km; Circle = 2 km; Triangle = 500 m.

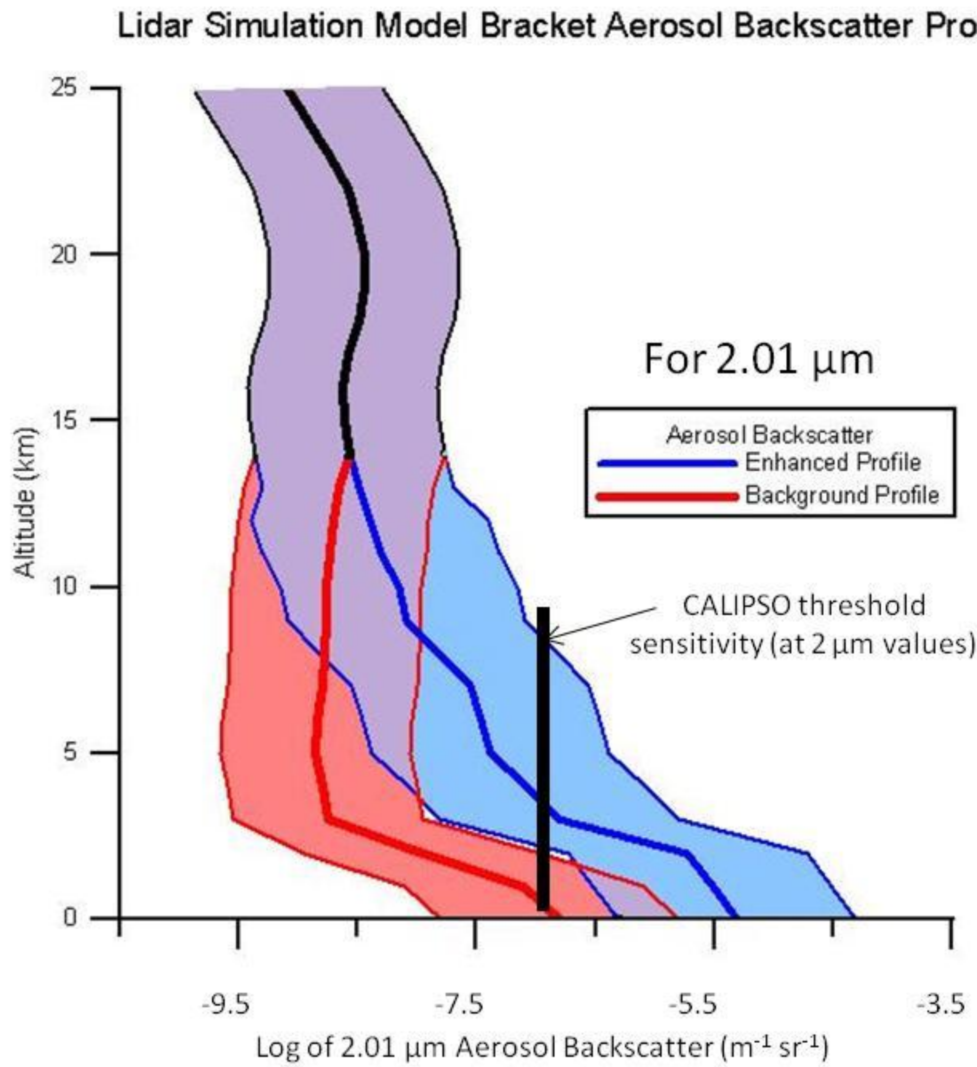

Figure 17: Bracket aerosol backscatter profiles used in current Doppler Lidar Simulation Model along with Background and and enhanced profiles as well as CALIPSO threshold.

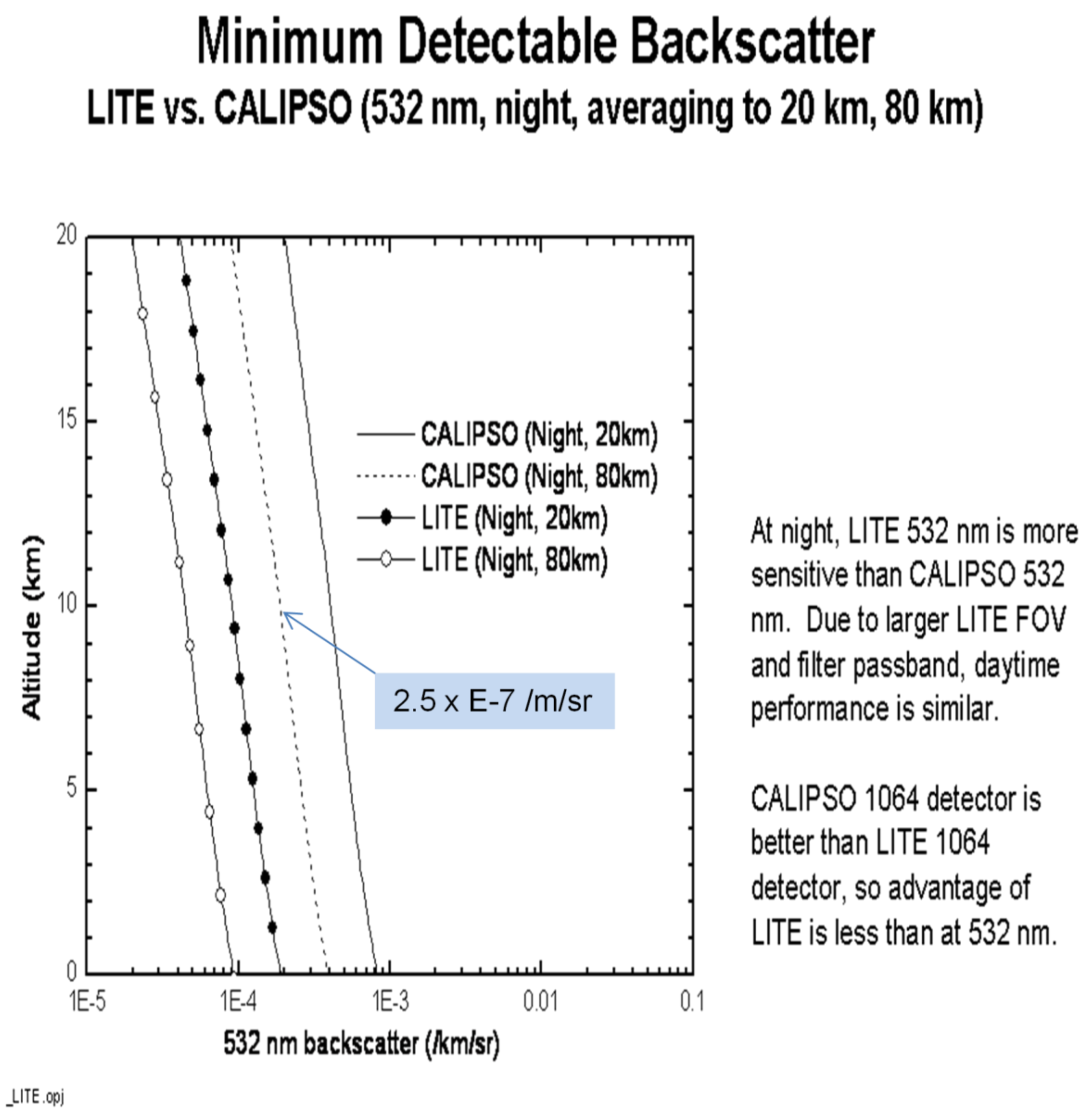

Figure 18: Estimated threshold sensitivities for CALIPSO and LITE (Provided by Winker et al., 2010)

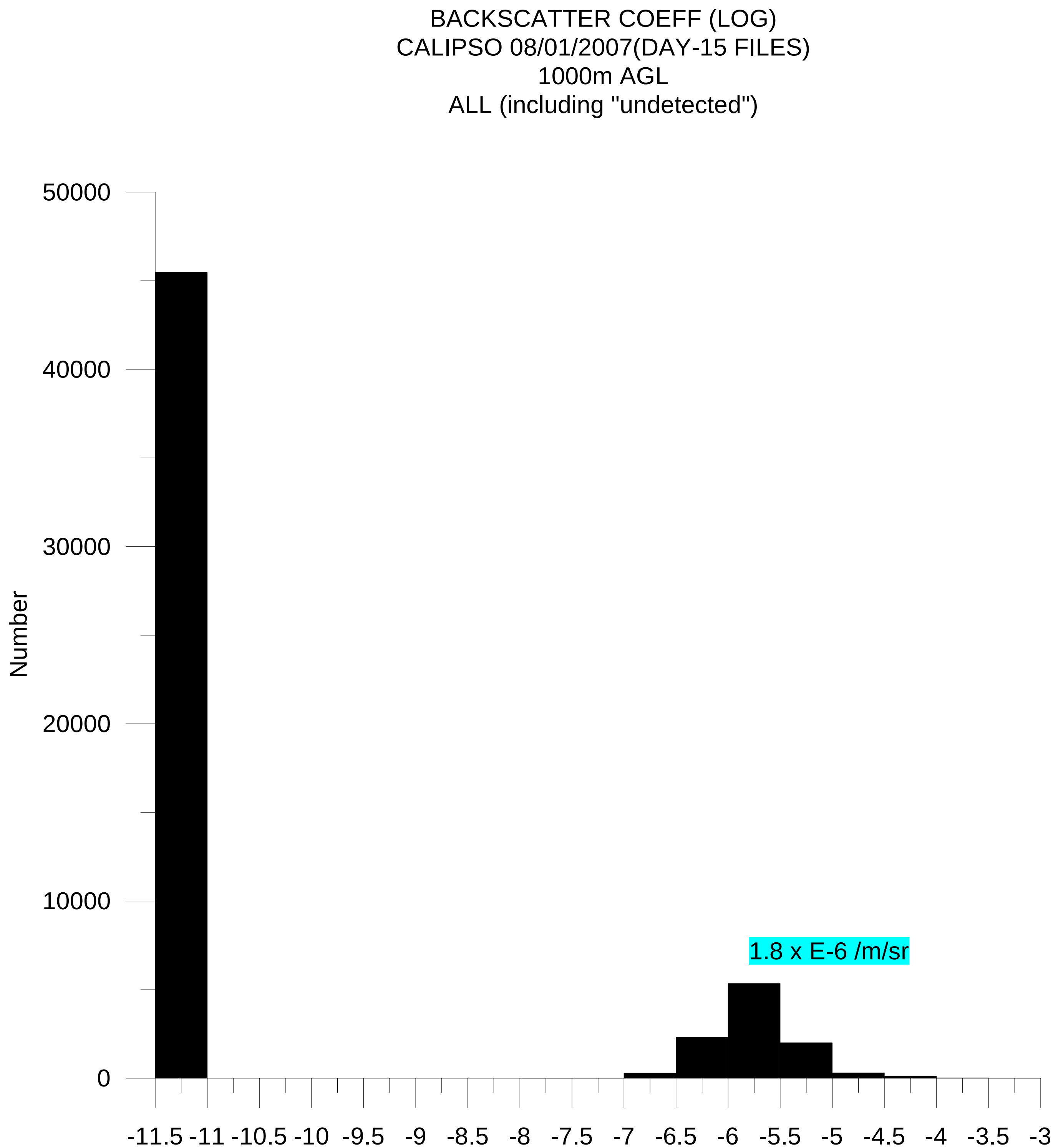

Figure 19: Distribution of CALIPSO Level II Backscatter Coefficient values (log) including when no aerosols were deteced on August 1, 2007

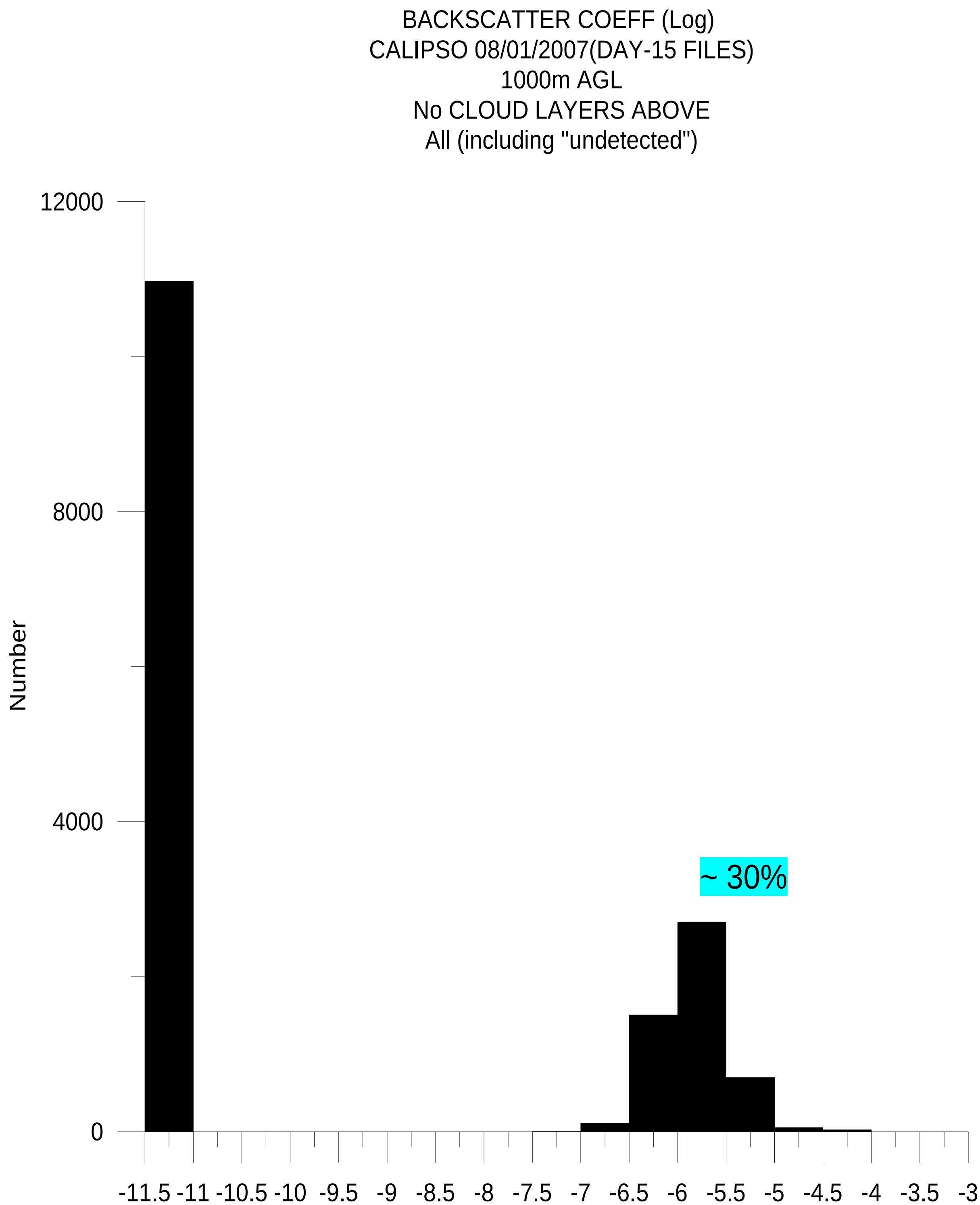

Figure 20: Distribution of CALIPSO Level II Backscatter Coefficient values (log) with no clouds above and including when no aerosols were deteced on August 1, 2007

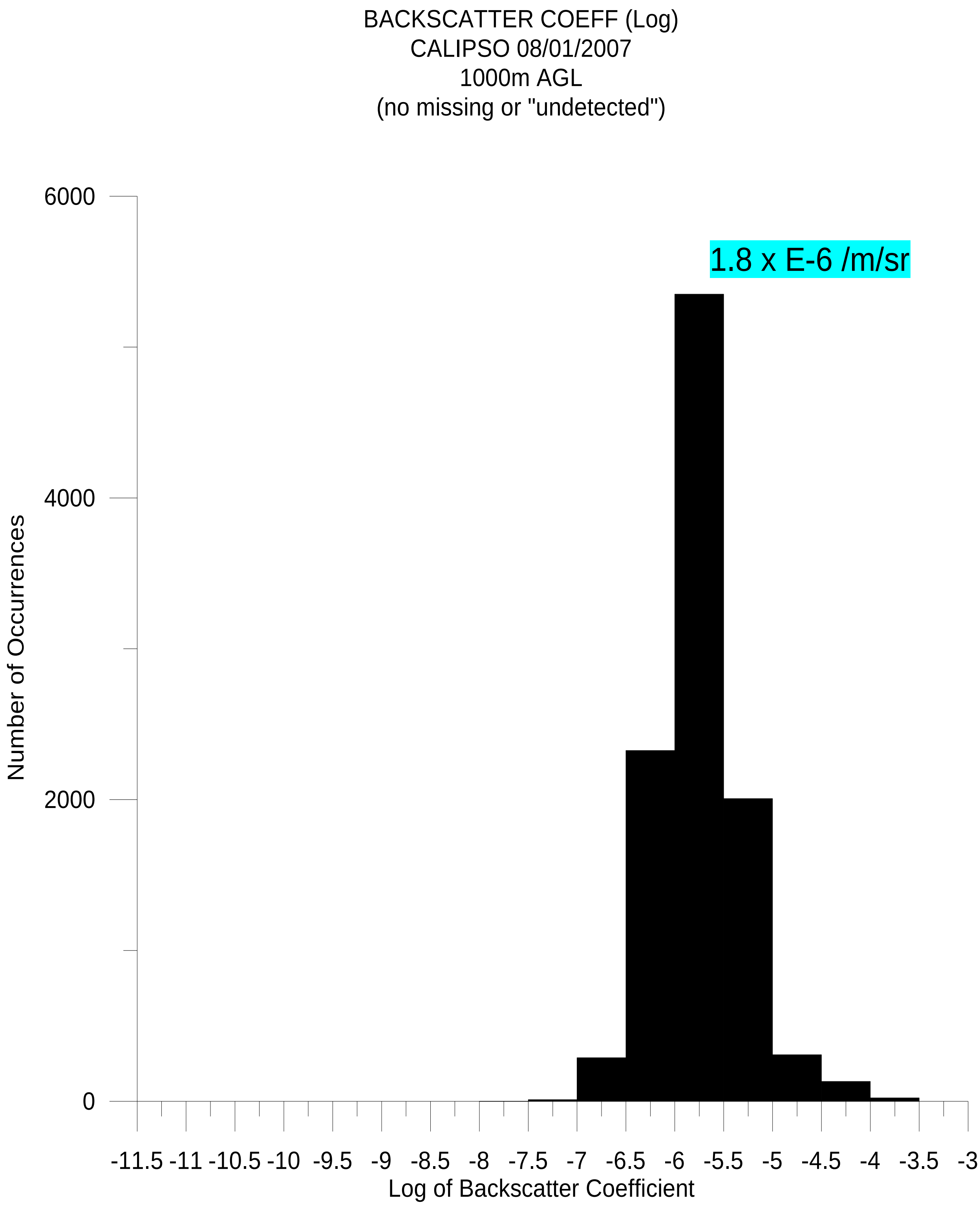

Figure 21: Distribution of CALIPSO Level II Backscatter Coefficient values (log) when aerosols were deteced on August 1, 2007

Range	Count	Upper Limit	Cum. Freq.
>-11 - -10	0.144226575770096	-10	0.144226575770096
>-10 - -9	0.055751618234403	-9	0.199978194004499
>-9 - -8	0.243383601891383	-8	0.443361795895882
>-8 - -7	0.307639558371207	-7	0.751001354267089
>-7 - -6	0.184579144286829	-6	0.935580498553918
>-6 - -5	0.0596824358444659	-5	0.995262934398384
>-5 - -4	0.00473706560161594	-4	1

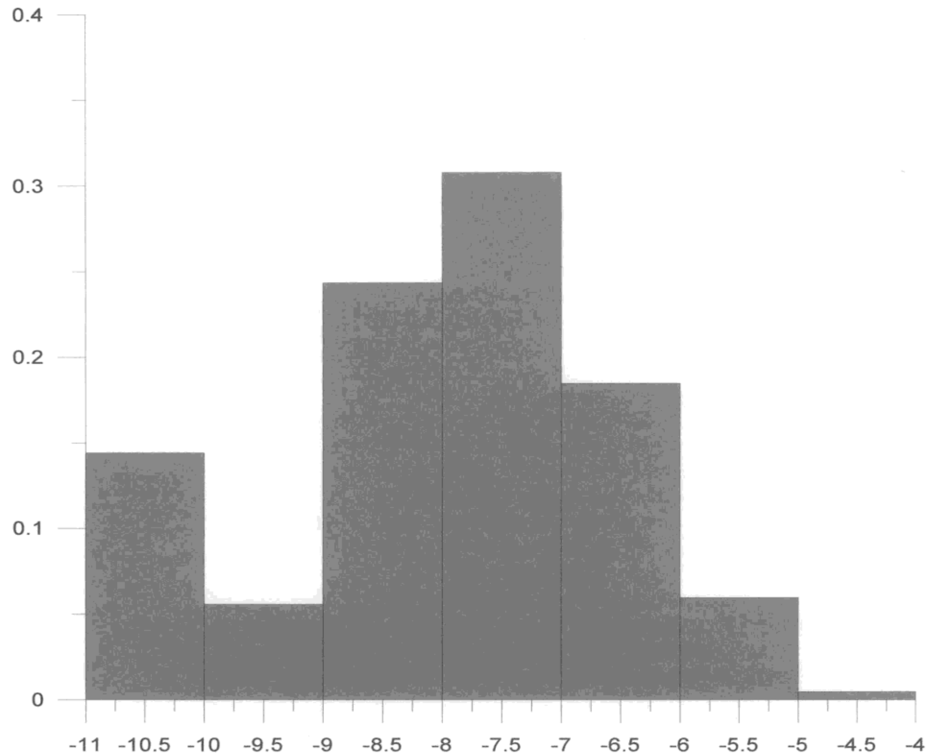

Figure 22: Distribution of calculated ECMWF T511 Nature Run Backscatter Coefficient Values (log) in m-1 sr-1 for background mode of aerosols. Y-axis is percentage of occurrence while x-axis is as in Figures 19-21

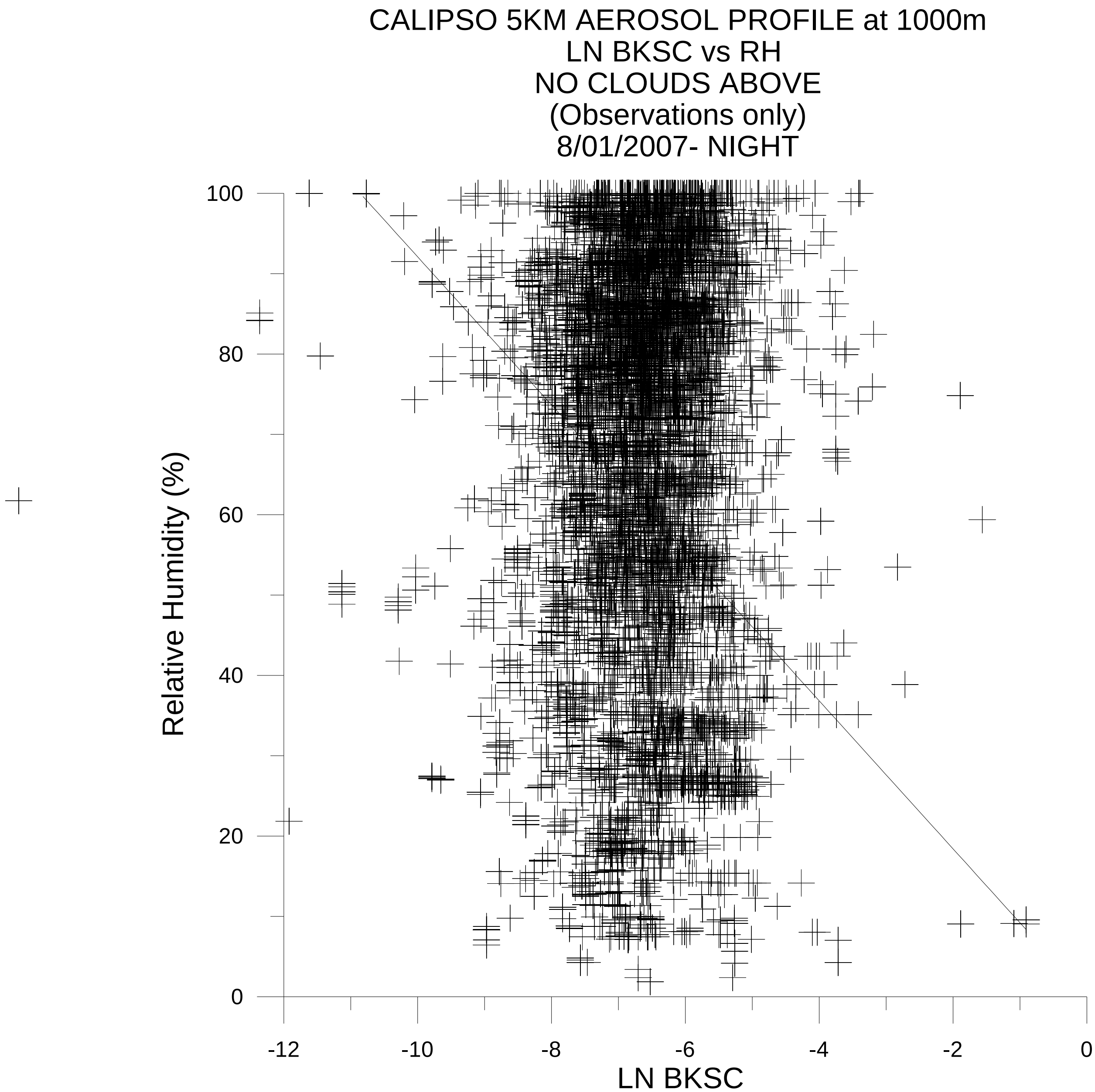

Figure 23: Scatterplot of CALISPO Level 2 5 km 532 nm backscatter coefficient (log) versus RH for at 1000 m for profile observations with no clouds above.

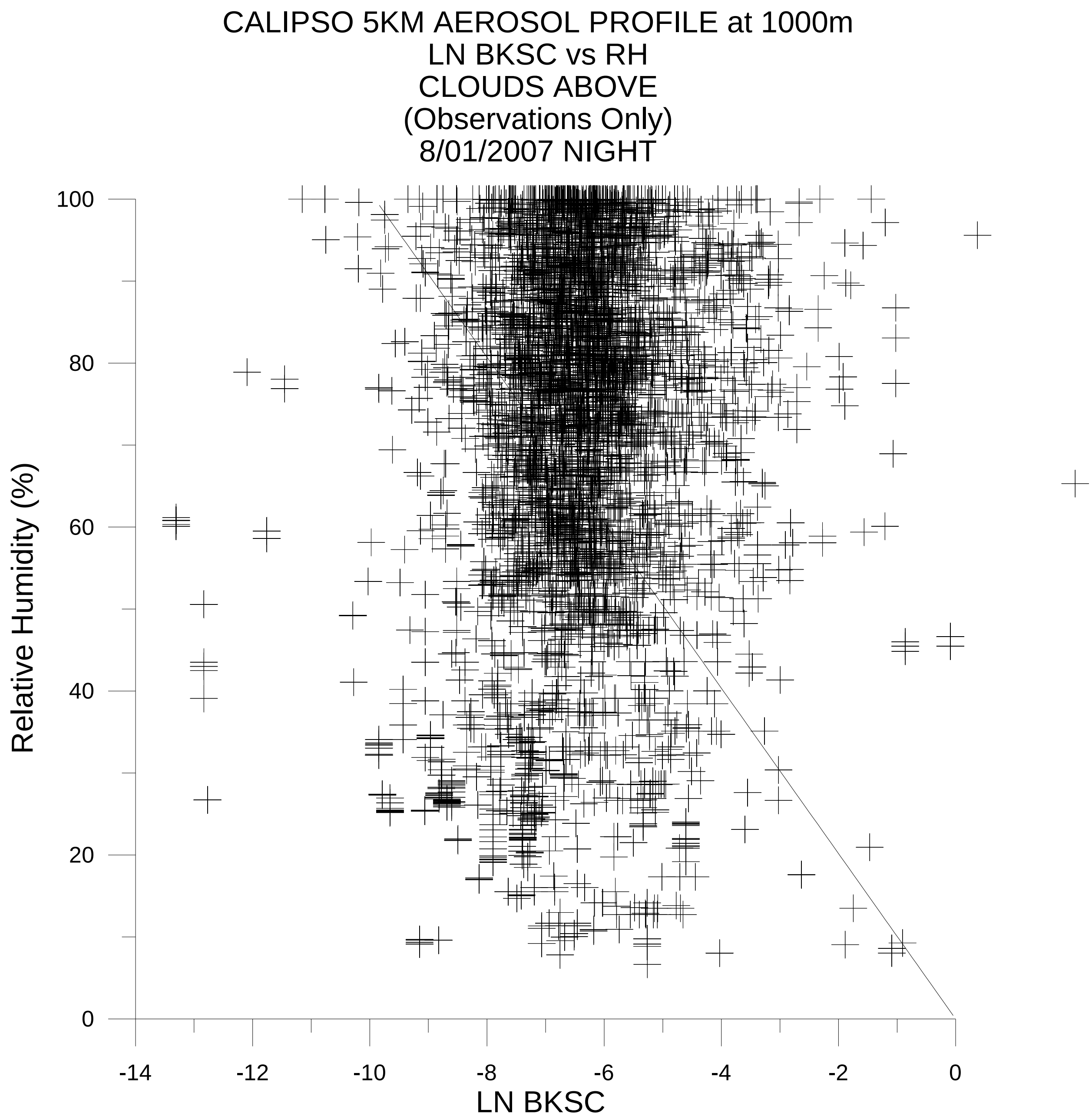

Figure 24: Scatterplot of CALISPO Level 2 5 km 532 nm backscatter coefficient (log) versus RH for at 1000 m for profile observations with clouds above.

8. ATTACHMENT 1

CALIPSO Backscatter:

Modeling, PDFs and Wavelength Conversion

ICESat and CALIPSO data for DWL Design and Data Utility Studies

Year Two: UAH Final Report

July 20, 2010

From:

Earth Systems Science Center (ESSC)

University of Alabama in Huntsville (UAH)

Subcontract SWA08-UAH

By:

David A. Bowdle

Principal Investigator, Research Scientist (Retired)

and Dr. Kirk A. Fuller

Research Scientist

To: Simpson Weather Associates (SWA)

Prime Contract: NNH08CD12C

For: the National Aeronautics and Space Administration (NASA)

ROSES 2007 - A.14 Wind Lidar Science

EXECUTIVE SUMMARY

The University of Alabama in Huntsville (UAHuntsville, hereafter UAH) has developed an aerosol scattering model that computes the volume backscatter coefficient, volume extinction coefficient, volume scattering coefficient, single-scatter albedo, and lidar ratio at a given wavelength and relative humidity, for spherical aerosol particles with arbitrary concentrations, size distributions, and compositions. The scattering model was applied to NASA's existing Cloud-Aerosol LIdar with Orthogonal Polarization (CALIOP) and NASA's prospective Global Wind Observing System (GWOS), using existing CALIOP models for the aerosol physical and chemical properties for both instruments, with CALIOP optical properties at the CALIOP wavelengths (0.532 μm, 1.064 μm) and extrapolations of those optical properties at the GWOS wavelengths (0.355 μm, 2 μm). Modeled scattering properties for the six wavelength pairs were ratioed and parameterized in terms of their wavelength dependence. These results will enable model-driven conversions between measured or derived aerosol backscatter properties at CALIOP wavelengths and predictions of these properties at the GWOS wavelengths.

To this end, UAH also examined the end-to-end uncertainties in modeled aerosol backscatter at the GWOS wavelengths, including CALIOP calibration, data processing, detection thresholds, and aerosol models; and UAH aerosol models. We also documented a long-standing philosophy at UAH and SWA, "How Good Is Good Enough", and adapted this philosophy for GWOS applications, to guide the study, and its resultant conclusions, recommendations, and priorities.

* *

The UAH study reached the following conclusions:

- Modeled aerosol backscatter color ratios fell into two classes: (a) clean, with backscatter properties dominated by coarse particles, and wavelength exponent of order unity; and (b) anthropogenic, with backscatter properties dominated by fine particles, and wavelength exponent of order 2. Color ratio dependence on these broad aerosol types was much more important than variations within these broad types.
- Color ratio dependence on the broad aerosol types was also more important than variations with relative humidity. The humidity-dependent variations fell into three classes: (a) low humidity, where backscatter color ratios showed little variability; (b) intermediate humidity, where these quantities showed rapid fluctuations (presumably related to the "optical glory phenomenon), in the clean aerosol types, and smooth monotonic growth or non-monotonic features for the other aerosol types; and (c) high humidity, with large rapid changes that varied by aerosol type. Color ratio variations in the intermediate humidity range were small enough that GWOS screening studies could treat low and intermediate humidity as a single domain for each aerosol type. Color ratio uncertainties at high humidity will not be important until free-running global numerical models can generate realistic high-humidity fields.
- Backscatter values at the GWOS wavelengths, and backscatter color ratios between CALIOP and GWOS wavelengths, could encounter very large uncertainties from unknown complex index of refraction for organic constituents at 0.355 μm, and from optical resonances in sulfate-coated dust

at 2 μm. Both uncertainties will be exacerbated by nonsphericity effects, as on organic-laden fractal soot particles, and platelet or aggregate mineral dust particles

- Therefore, uncertainties in the physical, chemical, and optical properties of the six CALIOP aerosol models were less important than uncertainties in the aerosol optical constants at GWOS wavelengths (see *Recommendations* below). These uncertainties alone do not warrant reformulating CALIOP models or reprocessing CALIOP data for GWOS applications.
- Nevertheless, aerosol backscatter conversions from CALIOP to GWOS wavelengths should use Level 1 attenuated total aerosol backscatter ratios, instead of Level 2 backscatter and extinction. The Level 1 product is calibrated from first principles. It has not undergone *a priori* algebraic thresholding that sacrifices information content when aerosol backscatter is much smaller than molecular backscatter. Equally importantly, it avoids compounding errors that assumed or derived aerosol models otherwise impose on conversions from attenuated backscatter (at CALIOP wavelengths) to extinction and backscatter (at CALIOP wavelengths), and back again to attenuated backscatter (at GWOS wavelengths).

* *

Further studies were recommended on:

- *Parameterizing Humidity Dependence*: by understanding, and, if necessary, minimizing the high-frequency oscillations that appear with increasing relative humidity in the modeled backscatter color ratios and exponents for some aerosol types; and converting all of the RH response functions to computer-efficient lookup tables or parameterizations.
- *Improving UAH Aerosol Models at GWOS Wavelengths*: by expanded theoretical studies (followed by laboratory verification) for backscatter enhancements on organic aerosols at 0.355 μm, on sulfate-coated dust at 2 μm, and on non-spherical particles at both wavelengths
- *Improving CALIOP Detection Thresholds*: by analyzing archived CALIOP data sets of attenuated total backscatter ratios in diagnosed clear-air domains, after integration over at least 4 km vertically and 200 km horizontally; thereby potentially detecting and characterizing the convective aerosol system in the middle troposphere and even the background aerosol system in the middle and upper troposphere (MUT).
- *Developing an MUT Aerosol Model for CALIOP*: by reviewing relevant atmospheric aerosol studies during the two decades since NASA's Global Backscatter Experiment (GLOBE) from the 1980's to the early 1990's (primarily for improved characterization of the MUT aerosol background for GWOS; not needed for improved CALIOP retrievals).

* *

This study has provided a logical steppingstone between two types of GWOS simulations: (a) previous studies, based on aerosol climatologies that were decoupled from nature run dynamics; and (b) future studies, based on aerosol life cycles in chemical transport models (CTM) that ingest nature-run dynamics. The ideal CTM should use isentropic advection algorithms in the middle and upper troposphere, to suppress spurious numerical diffusion that otherwise overloads the MUT by contamination from higher aerosol concentrations at lower and higher altitudes.

1. Introduction

UAH was tasked to "convert aerosol backscatter measurements at LITE, ICESat, and CALIPSO wavelengths to backscatter estimates at wavelengths pertinent to a hybrid (Doppler) wind lidar" (HDWL, 0.355 and 2.01 μm)". The laser wavelengths for the expected sources were:

- 1.064, 0.532, and 0.355 μm (LITE, Lidar Technology Experiment);
- 1.064, 0.532 μm (ICESat, was Geoscience Laser Altimeter System [GLAS]); and
- 1.064, 0.532 μm (CALIOP: Cloud-Aerosol LIdar with Orthogonal Polarization, on the CALIPSO, Cloud-Aerosol Lidar and Infrared Pathfinder Satellite Observation).

The results of this study will provide updated inputs to performance simulations for the Global Wind Observing System (GWOS), NASA's prospective version of a spaced-based HDWL.

SWA has concentrated on CALIOP as the primary backscatter data source, and deferred LITE and ICESat for later followup research. The UAH task was restructured to "Using measurements of attenuated aerosol backscatter and retrievals of aerosol backscatter and extinction coefficients at 0.532 μm and 1.064 μm from CALIOP to predict aerosol backscatter coefficients, aerosol extinction coefficients, and attenuated aerosol backscatter at the 0.355 μm and 2.01 μm wavelengths." Under this refined task, UAH used in-house aerosol scattering models to derive theoretical conversion factors for aerosol backscatter coefficients and aerosol extinction coefficients among all pairs of the four wavelengths (0.355 μm, 0.532 μm, 2.01 μm, 1.064 μm).

Section 2 describes the modeling inputs. Section 3 shows key results. Section 4 discusses the implications of these results for GWOS performance simulations. Section 5 summarizes key uncertainties and recommends followup research. The Appendices provide supporting details. Appendix A gives the conversion equations between generic backscatter lidars. Appendix B presents the CALIOP calibration equation. Appendix C describes the background aerosol system in the middle and upper troposphere. Appendix D incorporates all UAH modeling results.

2. ***Modeling Inputs***

2.1 CALIOP Data Products: CALIOP [*Winker et al.*, 2009] is a pulsed lidar that operates from sun-synchronous low earth orbit, at an altitude of approximately 705 km, as part of the A-Train satellite constellation. The CALIOP Nd:YAG laser transmits simultaneous co-aligned pulses at the 1.064 μm fundamental wavelength and the 0.532 μm doubled wavelength (parallel polarization). Pulses are short (25 ns, 6-m), near-nadir, with ~70-m diameter footprint every 335 m. CALIOP receives backscatter signals in three channels: 1.064 μm fundamental wavelength (total unpolarized), 0.532 μm (parallel polarization), and 0.532 μm (perpendicular polarization).

Through a combination of irreversible on-board analog and digital signal processing, and reversible ground-based digital processing, backscattered signals from the atmosphere are background-corrected, vertically integrated, converted to geophysical units, calibrated, and geo-registered. Appendix B presents the implicit calibration equation for these derived vertical profiles, and briefly assesses the calibration uncertainty in these profiles.

At this point in the data processing sequence, the standard CALIOP data product consists of calibrated attenuated aerosol backscatter for each combination of wavelength and polarization in the receiver train. The CALIOP team uses these three measurements, along with prescriptive aerosol/cloud models (§2.2 below), to separate aerosol and cloud features, identify aerosol subtypes, and derive particulate (aerosol and cloud) backscatter and extinction coefficients.

2.2 CALIOP Aerosol Models: CALIOP uses six distinct aerosol types (Table 1, extracted from Table 1 in *Omar et al.* (2009). Each aerosol type is represented both by physical properties (bimodal size distribution, with volume- [or mass-] weighted mean radius, R_m, and geometric standard deviation, *GSD*, for each mode; and the fractional mass, *ff*, in the fine mode) along with chemical properties (compositional mix and complex index of refraction, $m_{real} + i \cdot m_{im}$ in each mode). The CALIOP project then uses a Mie scattering model to compute the extinction-to-backscatter ratio, S_a (the so-called *lidar ratio*), for each aerosol type. If a three-dimensional pixel or feature has adequate signal-to-noise ratio, the CALIOP data processing program compares the multivariate CALIOP measurements from that feature to stored multivariate probability density functions from independent data sources, to classify the feature as cloud or aerosol, to further identify its cloud or aerosol subtype, and finally to assign the nominal lidar ratio for that subtype. The CALIOP data processing program then uses a complicated iterative lidar inversion algorithm to combine the measured profile of attenuated backscatter and the assigned lidar ratio profile, and thence to derive vertical profiles of aerosol backscatter coefficient and extinction coefficient at the CALIOP wavelengths of 0.532 μm and 1.064 μm.

A rigorous and detailed critique of the physical, chemical, and optical parameters in the CALIOP aerosol models is beyond the scope of this work. However, it is noteworthy that *Omar et al.* (2009) recognized the limitations of these models, even for retrievals in optically thin aerosol layers, in view of their statement "although we cannot know that these model S_a values correctly characterize the actual aerosol layers observed, we do know that they produce physically realistic solutions". In other words, the CALIOP retrievals are not necessary unique under these benign conditions, due largely to inadequate *a priori* information about aerosol intensive properties. By contrast, in optically thick layers, the first guess lidar ratios often had to be adjusted to generate convergent solutions, again indicating well-known deficiencies in the aerosol physicochemical models. Version 3.01 reduced some of these retrieval uncertainties by adding more variables to its multivariate PDF data processing scheme. However, this refinement does not resolve the fundamental problem that CALIOP retrievals represent a highly under-determined solution, because CALIOP can use only three measured aerosol properties to characterize aerosol populations that have far more than three free parameters.

In addition, some specific concerns should be noted about the optical constants in the CALIOP aerosol models:

1. The actual values for the complex refractive indices of aerosols probed by space-borne lidar will likely vary significantly from the simple set tabulated here.
2. For clean and polluted continental aerosols, values of m_{real} are probably closer to 1.5 (that of dry ammonium sulfate) than those used in the CALIOP retrievals.
3. The prescribed refractive indices indicate anomalous dispersion (refractive index increasing with wavelength) from 0.532 to 1.064 μm, and we are doubtful that this often is the case.
4. The literature has insufficient information to allow reliable extrapolation of these optical constants from CALIOP wavelengths to GWOS wavelengths. The imaginary part could easily vary by 100%, the real part by 10-20%, from the values estimated here. Therefore, we choose conservative approaches for estimating these values.0.

This last point is discussed in greater detail in the next subsection and in Section 4.

2.3 UAH Aerosol Models: This study uses the same aerosol models as in CALIOP, with the same size distributions, and chemical properties as in the CALIOP aerosol subtypes. We also use the CALIOP optical constants at the CALIOP wavelengths. We extrapolate these prescribed optical constants to the GWOS wavelengths using the prescribed chemical compositions, except where independent information indicates otherwise. For example, this study assumed that organics are a major component of aerosol associated with polluted air masses. Because it is suspected that many organic aerosols absorb more strongly in the near UV, m_{im} was increased by 50% for the calculations at 0.355 μm for smoke, polluted continental and polluted dust. This parameter was held constant for all of the clean air masses, and for extrapolation to 2.01 μm in all airmasses. Once again, such extrapolations are fraught with uncertainties. This approach ensures internal consistency with the measured and derived aerosol profiles from CALIOP. However, the validity of this approach depends directly on the validity of the prescribed aerosol models in the CALIOP algorithm, as discussed earlier.

2.4 Relative Humidity Growth Function and Refractive Index Mixing Rules: The radii of hygroscopic particles are determined via an iterative solution to a pair of equations that relate water activity and particle size, based on simplifying assumptions that introduce errors of only a few percent [*Hanel*, 1976]. For this study, it is assumed that water uptake by dust and polluted dust is negligible, though we recognize that dust may become hygroscopic after undergoing any appreciable atmospheric processing. After the sizes of the wet aerosol particles have been determined, the modified refractive indices are calculated as volume-weighted averages.

2.5 Mie Scattering Model: The differential scattering cross-section for a sphere illuminated by light of wavelength λ is given by:

$$\frac{d\sigma}{d\Omega} = \frac{|\mathbf{X}|^2}{k^2},$$

where $\mathbf{X}(\Omega)$ is a vector scattering amplitude that quantifies the angular distribution of scattered light, and $k = 2\pi/\lambda$. The backscatter cross-section is defined to be

$$\sigma_b = 4\pi \left. \frac{d\sigma}{d\Omega} \right|_{180°}$$

(The factor of 4π is not always included in this definition.)

The backscatter efficiency for a sphere of radius *a* may be calculated from

$$Q_b = \frac{\sigma_b}{\pi a^2} = \frac{1}{x^2} \left| \sum_{n=1}^{\infty} (2n+1)(-1)^n (a_n - b_n) \right|^2$$

with $x = ka$. This expression is derived from Mie theory. The quantities a_n and b_n are the Mie coefficients, and are functions of the sphere's size and complex refractive index. Similar expressions are used to calculate extinction and scattering efficiencies [*Bohren and Huffman,* 1983]. For a population of spheres of different sizes, the single-sphere optical properties must be averaged over all sizes to obtain the response of a volume of aerosol to illumination by a laser beam.

The code used here outputs the volume extinction, scattering and backscattering coefficients, written respectively as:

$$\beta_{ext} = \frac{\pi}{k^3} \int_0^{\infty} x^2 Q_{ext}(x) \eta(x) dx$$

$$\beta_{sca} = \frac{\pi}{k^3} \int_0^{\infty} x^2 Q_{sca}(x) \eta(x) dx$$

$$\beta_b = \frac{\pi}{k^3} \int_0^{\infty} x^2 Q_b(x) \eta(x) dx,$$

where $\eta(x)$ is the size distribution function for the aerosol population. All distribution functions in this work are assumed to be lognormal, and are specified by their mean radius R_m and geometric standard deviation (GSD). The code also allows one to input bimodal distributions in order to account for fine- and coarse-mode particles. The integrals are approximated by finite sums using Simpson's rule, in increments of 0.02 *x* over the range 0.001= $x_{min} < x <$ 50= x_{max}.

The equation for volume backscatter can be re-written as:

$$\begin{aligned} \beta_b &= \frac{\pi}{k^3} \int_0^{\infty} (ka)^2 \frac{\sigma_b(ka)}{\pi a^2} \eta(ka) d(ka) \\ &= \int_0^{\infty} \sigma_b(a) \eta(a) da \\ &= \langle \sigma_b \rangle \, (m^2 \text{per } m^3 \text{ of air}) \end{aligned}$$

Thus the volume backscatter coefficient is the average backscatter cross-section per unit volume.

For particles very small compared to the wavelength, Rayleigh scattering prevails and the scattering cross-sections are proportional to λ^{-4}. The ratio of the signal detected at λ_1 to that at λ_2 will then be $\left(\frac{\lambda_2}{\lambda_1}\right)^4$. As particle size increases, then the exponent α will decrease below 4. In general, we write the color ratio as

$$\frac{\beta_i}{\beta_j} = \langle\sigma_b\rangle_i / \langle\sigma_b\rangle_j = \left(\frac{\lambda_j}{\lambda_i}\right)^{\alpha} \text{ so that}$$

$$\ln\left(\frac{\beta_i}{\beta_j}\right) = \alpha \ln\left(\frac{\lambda_j}{\lambda_i}\right)$$

In order to estimate the expected signal in channel *i* based on a known signal in channel *j*, we have calculated

$$\beta_{ij} = \beta_i / \beta_j \text{ and}$$

$$\alpha_{ij} = \frac{\ln(\beta_i / \beta_j)}{\ln(\lambda_j / \lambda_i)} \text{ for } \lambda_j > \lambda_i$$

for 0.355, 0.532, 1.064 and 2.01 μm (numbered 1-4, respectively) channels.

Numerous light scattering models are operative in the aerosol optics community. All of these models involve complicated recursive computations in the complex variable domain. Coding errors in these models, or careless use of these models, can easily generate unstable results, or, perhaps more risky, results that look reasonable, but in fact exhibit significant errors. Users of such models must take special care to ensure proper model coding, and to validate model data output. Dr. Fuller has developed his own aerosol scattering model and has imposed extensive testing on his model to ensure reliable results. Perhaps the most stringent test involves computation of the backscatter cross-section from a large sphere with *x*>100. When the model operates properly, this computation reduces to

$$Q_b = \left|\frac{m-1}{m+1}\right|^2,$$

provided that the imaginary part of *m* is large enough to suppress internally reflected light [*Bohren and Huffman*, 1983]. We will refer to this condition as the bulk reflectance test, since this limiting value is simply the normal incidence reflectance of a bulk sample with refractive index *m*. Dr. Fuller periodically verifies that his model passes this rigorous test, and that the model is ready for high-stakes aerosol scattering research, such as the work reported here.

3. ***Results: Modeled Wavelength Dependence***

3.1 Backscatter coefficients: Appendix D provides graphical results for the backscatter modeling calculations that were performed on all CALIOP aerosol types) for each pair of wavelengths in the CALIOP + GWOS spectral set, using the assumptions, input data, and modeling methods in Section 2. Results are presented in terms of backscatter color ratios $\beta_{i,j} = \beta(\lambda_i)/\beta(\lambda_j)$ as a function of relative humidity (RH), and in terms of the color ratio parameter α, as derived from $\beta(\lambda_i)/\beta(\lambda_j) = (\lambda_j/\lambda_i)^{\alpha_{ij}}$ (§2.5), at 0% RH.

The following two figures display the color ratio plots for two representative wavelength pairs; β_{12} [$\beta(0.355\mu m)/\beta(0.532\mu m)$] and β_{24} [$\beta(0.532\mu m)/\beta(2\mu m)$]. The color ratios for clean marine and clean continental aerosol warrant special discussion. The variations of these ratios with relative humidity appear 'noisy.' While this result was somewhat unexpected, it is believed that these features can be explained in terms of interference between the electromagnetic fields that are backscattered directly from the particle surfaces and those that emerge in the backward direction after 'retroreflection' within the particle. Such effects are seen in the optical glory phenomenon [c.f. *Greenler*, 1980], where colors are preferentially scattered into narrow angles near the direct backscatter angle, even though the particle sizes are distributed over a broad range. Support for this interpretation comes from the fact that the curves are much smoother for aerosol types with larger imaginary index of refraction, wherein the internally scattered light would be suppressed, as in the case of the bulk reflectance test, which the large polluted aerosol particles easily pass. This effect does not appear in the fine mode. One might suspect an error in the size averaging algorithm. However, smoothly varying volume scattering coefficients (Appendix D, page D44) and their ratios indicates that the observed 'noise' is not likely due to such a source.

4. Discussion: GWOS Applications Issues

4.1 How good is good enough? Discussions earlier in this report have already mentioned several sources of potentially significant uncertainties in the standard backscatter products from CALIOP. When CALIOP data are combined with modeled backscatter conversion factors from CALIOP wavelengths to GWOS wavelengths, the uncertainties in the CALIOP data and in the conversion models obviously propagate directly into the predicted backscatter at GWOS wavelengths. To assess the significance of the uncertainties in the GWOS backscatter properties, it is first useful to assess how large those uncertainties must be to adversely affect GWOS performance simulations. We begin with the following qualitative generalizations, which apply to all GWOS backscatter inputs, not just to those derived from CALIOP.

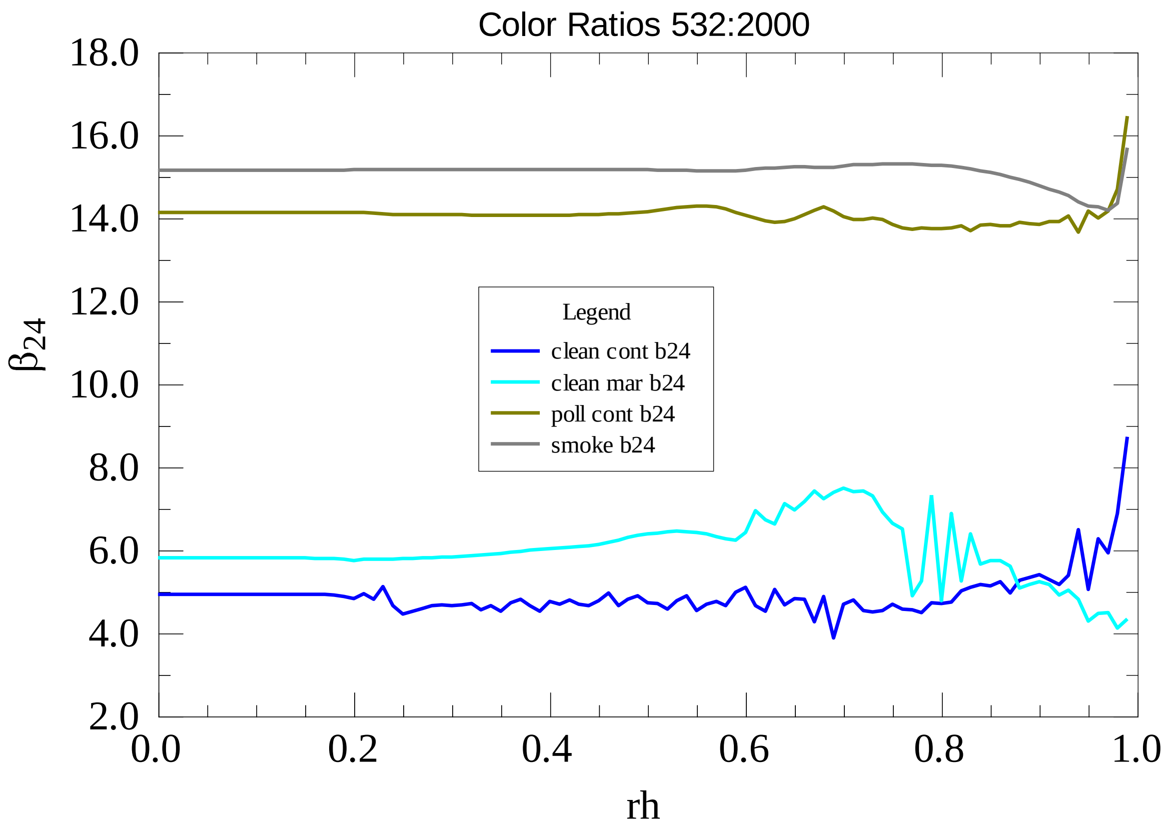
Color Ratios 532:2000
18.0
16.0
14.0
12.0
10.0
8.0
6.0
4.0
2.0
β24
0.0
0.2
0.4
0.6
0.8
1.0
rh
Legend
clean cont b24
clean mar b24
poll cont b24
smoke b24

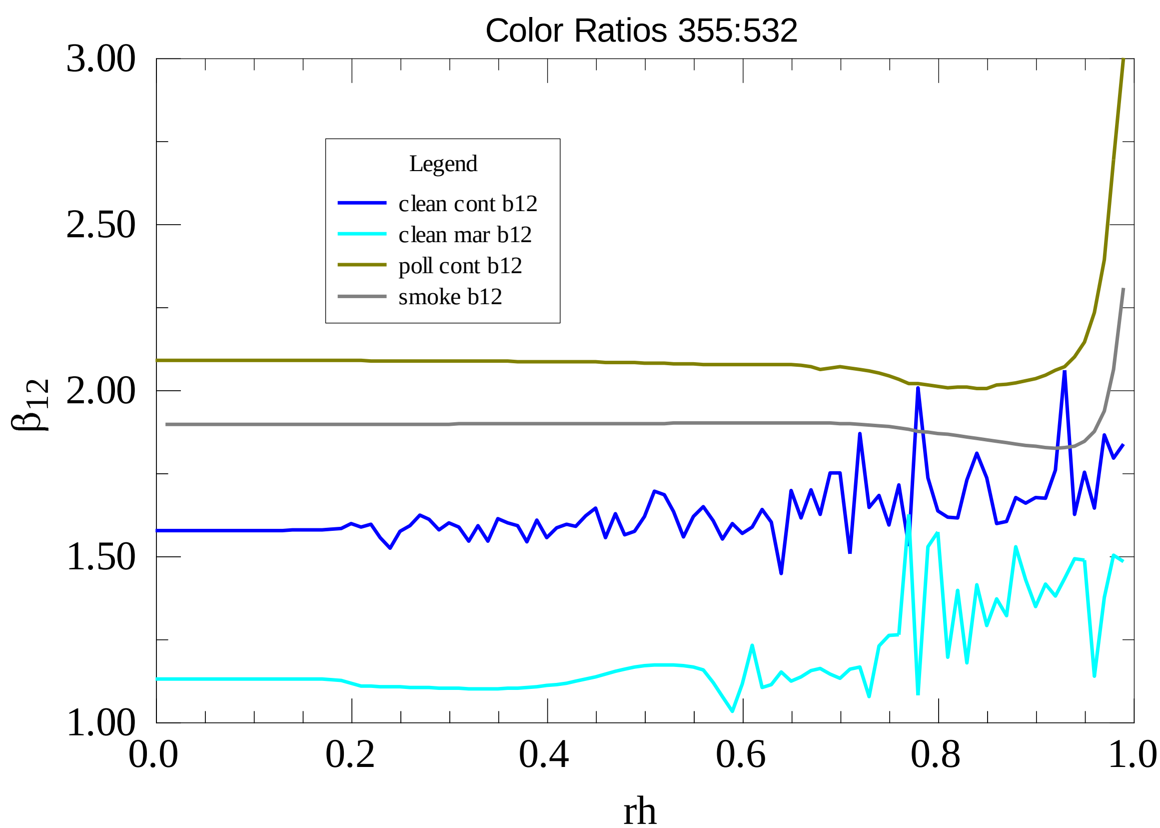
Color Ratios 355:532
3.00
2.50
2.00
1.50
1.00
β12
0.0
0.2
0.4
0.6
0.8
1.0
rh
Legend
clean cont b12
clean mar b12
poll cont b12
smoke b12

First, when the predicted backscatter at a given GWOS wavelength is far above or far below the expected detection threshold for a given GWOS configuration, we need to concentrate on spatial/temporal statistics and atmospheric correlations for those aerosol backscatter fields. We can ignore uncertainties in the measured or derived aerosol products from CALIOP. We can also ignore uncertainties in aerosol physicochemical models, complex index of refraction, relative humidity effects, and wavelength dependence in the conversion factors. However, this methodology is valid only if the combined effect of all such uncertainties is small enough to keep the predicted backscatter well above or below the GWOS threshold.

Second, when a subset of the predicted GWOS backscatter is close to the expected GWOS threshold, we need to address uncertainties in all of the above issues. The same approach holds if the uncertainty in the predicted backscatter is large enough to approach or encompass the predicted GWOS threshold. This latter condition is especially important if the backscatter uncertainties arise from aerosol measurements that fall below the detection threshold for the source data. Unfortunately, for this study, the Level 2 CALIOP backscatter data products provide the same flag for all sub-threshold measurements. Thus, we cannot assess the probability distribution of measurements just below or far below the CALIOP threshold, or the nominal magnitude and potential uncertainty in predicted GWOS backscatter from such measurements, without reaching further back into the CALIOP data processing stream. Although quantitative assessments are important here, they significantly exceed the UAH scope of work for this study.

Third, when the predicted backscatter in a given atmospheric domain (spatial, temporal, or phenomenological) is close to the expected GWOS threshold, and the GWOS simulation results are highly sensitive to the results from this domain, we must pay very careful attention to all of the uncertainties in all of the above issues. This condition also applies when the uncertainties in the predicted backscatter are large enough to approach or encompass the GWOS threshold.

The weakness in this approach is that the expected detection threshold tends to be a floating target as the GWOS mission evolves. The recent re-emergence of an ISS-based GWOS is just one more manifestation of this floating target. This kind of mission creep eventually requires modeling studies such as this to cover a very large dynamic range in backscatter coefficient.

4.2 Trends

4.2.1 Fine vs. Coarse Mode: As noted elsewhere, the backscatter at each wavelength, and the backscatter color ratios between each wavelength, represent the weighting of the backscatter cross-section by the aerosol size distribution in both the fine and coarse modes. This weighting also depends strongly on aerosol type. For example, the fine mode dominates all color ratios for polluted dust and dry smoke, while the coarse mode dominates all color ratios for clean marine, clean continental, and polluted continental. By contrast, both fine and coarse modes make significant contributions to the color ratios for dry dust. These trends provide useful guidelines about which mode to concentrate on in any future studies where a given aerosol type plays an important role in simulated GWOS performance (see also §4.1, How Good is Good Enough). Note, however, that these guidelines must be applied with due caution, because the size distribution for a given aerosol source can change significantly with increasing atmospheric residence time, due to aging processes such as coagulation and sedimentation. Thus, the size distribution of a given aerosol source type may show considerable evolution after convective lofting, cloud processing, and dilution by the clean free troposphere.

4.2.2 Relative Humidity Effects: The plots in this section and in Appendix D show that backscatter color ratios exhibit three basic regimes. At low humidity, the ratios are essentially constant for all CALIOP aerosol types, because these aerosols do not show significant condensational growth under these conditions. As the humidity increases, the color ratios change slowly but steadily for most aerosol types, but with features that differ by aerosol type. These differences arise from differences in the water uptake for the various materials, combined with complex differences in the relative weighting between the backscatter cross-sections and the growing solution droplets at different wavelengths. Exceptions are evident for clean marine and clean continental, which show significant fluctuations as the humidity increases. Section 3.1 discusses the probable causes of these fluctuations. Near saturation, color ratios rapidly increase for several aerosol types, as the aerosols grow in the abundantly available water vapor.

4.3 Uncertainties:

4.3.1 Coated Aerosols: Unpublished aerosol scattering models (*V. Srivastava*, early 1990's) predict very large backscatter enhancements (factors of ~5-20) for sulfuric acid coatings on mineral dust particles. The magnitude of the predicted enhancement varies with particle size and coating thickness.

It is important to note that neither the presence nor the magnitude of the predicted backscatter enhancements has been empirically verified in the laboratory or in the atmosphere. But is equally important to note that no experiments have yet been conducted that could provide empirical verification or refutation. Ironically, the enhancements occur only in a narrow spectral band centered approximately on the 2 μm wavelength. The enhancements disappear well above the Raman-shifted 1.5 μm wavelength at which a large set of backscatter measurements was obtained during the GLOBE flights in 1989/1990. They also disappear well above the 1.5-1.6-μm wavelength band where modern ground-based coherent DWL systems operate. In addition, these resonance-based enhancements are much stronger in 180° backscatter than in scattering at other angles, or in absorption or extinction. Therefore, empirical verification of this resonance would require differential scattering (DISC) experiments, with simultaneous or sequential backscatter measurements at 2 μm and at one or more nearby wavelengths that are close enough to 2 μm to be affected by the resonance, far enough from 2 μm to be well off the resonance peak, and free from significant interference by gaseous absorption lines.

Although the predicted enhancements have not been observed empirically, they rest on a sound theoretical basis. The imaginary index of refraction for the sulfuric acid coating and for the silicate core cross near 2 μm, and rapidly diverge on either side of 2 μm. Similar conditions for other coatings on other cores have produced prominent scattering resonances at other wavelengths. Thus, we can confidently expect prominent backscatter resonances for sulfuric acid coatings on dust particles.

However, these coated dust particles introduce some conditions that were not present for the empirically verified resonances on other coated particles. First, dust particles are highly non-spherical, unlike the spherical particles in the other studies. Non-sphericity is likely to broaden and weaken the resonance peak. Second, sulfuric acid will leach out and react with internal mineral laminae, such as aluminum and magnesium, to produce surficial and infiltrated coatings of sulfate salts. Srivastava's modeling studies did not address coatings of this type, the effects of these reactions on the optical constants of the dust core, or the effects of other water soluble coatings.

In spite of these uncertainties, we expect significant, but yet to be determined backscatter enhancements for sulfate-rich coatings on mineral dust particles at the 2 μm GWOS wavelength. We also expect that such coatings are common in the atmosphere, so they could have a dramatic effect on GWOS performance in highly diluted dust plumes. At other wavelengths, diluted dust plumes appear on the high-backscatter side of the background MUT mode. Accounting for this effect in the 2-μm GWOS channel would essentially move the GWOS threshold deeper into the high-backscatter side of the background mode, for even more dilute dust plumes. As noted above, these enhancements would not be apparent at CALIOP wavelengths, and the color ratio modeling in this study did not account for these enhancements. Future studies should examine this effect, first with expanded theoretical models, and then with carefully designed laboratory experiments.

4.3.2 Organic Aerosols: Section 2.3 noted considerable uncertainty in the imaginary index of refraction at 0.355 μm, due to the presence of organic components in polluted aerosols. The organic aerosol fraction can contain hundreds of different organic components in innumerable mass fractions, multiphase mixtures, and coatings, all combined on fractal soot particles. This variety is completely intractable, unless systematized and parameterized in a way that drastically reduces the number of free parameters. In the simple sensitivity study conducted here, the addition of organics significantly increased the aerosol backscatter at 0.355 μm. As in the case of coated dust: (a) organic-driven backscatter enhancements in polluted aerosols would not be apparent at CALIOP wavelengths; (b) the presence of such enhancements could have a significant impact on GWOS simulations at 0.355 μm, and on the corresponding NWP impacts; and (c) the potential importance of these effects warrants expanded theoretical studies with followup laboratory experiments.

4.3.3 Nonsphericity: As noted in §2.5, our backscatter modeling studies assumed spherical particles. When the lidar wavelength is much larger than the particle size, nonsphericity reduces the backscatter near the peaks of strong absorption lines, and increases the backscatter in the wings of the broadened peaks [*Huffman and Bohren*, 1979]. However, at the CALIOP and GWOS wavelengths, the particles sizes are much closer to the lidar wavelengths, and, with the possible exception of organic components, most aerosol constituents do not have strong absorption lines near these wavelengths. Although this phenomenon may be important, proper treatment requires complicated and highly specialized numerical models for nonspherical particles, which are well beyond the scope of the UAH study.

4.3.4 CALIOP Aerosol Constants: In addition to the special cases discussed above in §4.3.1 (sulfate coatings on mineral dust particles) and §4.3.2 (organic coatings on soot, dust, and sulfate particles), we have some general concerns about the aerosol constants that are used in the CALIOP backscatter retrieval algorithm. As noted in §2.2, these concerns involve normal atmospheric variation around the nominal CALIOP values, unrealistically high values for the real index of refraction in clean and polluted continental aerosols, potentially unphysical anomalous dispersion between 0.532 and 1.064 μm, and uncertainties in the modeled backscatter color ratios between CALIOP and GWOS wavelengths. In practice, we expect these uncertainties to be less important than natural variation in the aerosol size distributions.

4.3.5 Version 3.01 (V3.01) vs. Version 2 (V2): V3.01 of the CALIOP backscatter database [*Winker et al.*, 2010], which was released in spring 2010, includes several key improvements:

- Restructured profile products, more retrieved parameters, data flags, uncertainty parameters, all reported with 5-km horizontal integration and resolution.
- An improved cloud-aerosol discrimination algorithm, with a 5-dimensional (5D) probability distribution function (PDF), which now includes latitude and volume-depolarization ratio, in addition to the layer-mean attenuated aerosol backscatter at 0.532 μm, layer-integrated 0.532-μm/1.064-μm attenuated backscatter ratio, and mid-layer altitude already in the V2 3D-PDF;
- A completely new algorithm for cloud ice-water phase discrimination;
- Constrained extinction retrievals using CALIOP surface returns and CloudSat ocean surface reflectance, to estimate 2-way column transmittance; and, most importantly;
- Improving the daytime calibration (§4.3.6 below) for the 0.532-μm parallel channel.

4.3.6 Calibration Methodology: V2 and V3.01 both use the same fundamental calibration reference target [*Powell et al.*, 2009]. During nighttime, the 0.532-μm parallel channel is calibrated against molecular backscatter in the 30-km/34-km layer, assuming that this layer and all overlying layers are aerosol-free. This calibration anchors the nighttime calibration for the 0.532-μm perpendicular channel and the 1.064-μm channel. It also anchors daytime calibration for all channels, again beginning with the 0.532-μm parallel channel.

During daytime, the solar scattering background dramatically increases the noise baseline, which prevents calibration against molecular backscatter in the 30-km/34-km layer. Solar heating also creates thermal misalignment, which significantly degrades the optical efficiency in a manner that is difficult to predict and correct from first principles. *Hunt et al.* (2009) briefly discussed this thermal drift problem, which also affected the calibration transfer from the 0.532-μm parallel channel to the 1.064-μm channel.

To resolve this problem, the CALIOP team conducted an intensive study of the calibration drift for the 0.532-μm parallel channel, using the 8km/12-km layer as a surrogate calibration target. The parametric discriminator for this layer is the total attenuated aerosol backscatter ratio:

$$R'\left(\lambda_{0.532\mu m}, z_{8-12km}, k_p\right) = \left\{1 + \frac{\beta_{aer}\left(\lambda_{0.532\mu m}, z_{8-12km}, k_p\right)}{\hat{\beta}_{mol}\left(\lambda_{0.532\mu m}, z_{8-12km}, k_p\right)}\right\} \times T_{aer}^{2}\left(\lambda_1, z_{8-12km}, k_p\right),$$

where β_{aer}, β_{mol}, z, and k_p, respectively, are the volume aerosol backscatter coefficient, volume molecular backscatter coefficient, altitude, and (after three-shot onboard averaging) lidar pulse index; and the ^ symbol indicates inputs from external models (see also Appendix B, CALIOP Calibration Equation, page 1, line 1, left-hand side of the calibration equation). Using the method described in *Powell et al.* (2009), the CALIOP layer detection algorithm was first used to identify clear air regions (no aerosol or cloud features above a designated noise threshold, or, in other words, R' = unity, within statistical error) throughout each profile in the 8-12 km layer over a contiguous horizontal length of at least 200 km.

In *Powell et al.* (2009), R' was first averaged vertically from 8 km to 12 km, and then averaged horizontally for 200 km in the designated clear-air regions. The averaged quantities were then plotted as a function of time since the start of the nighttime orbit. In *Powell et al.* (2010), the nighttime averaging methodology was extended to daytime, the clear-air block averages were further averaged at each latitude over a seven-day period, and the averaged R' values were plotted as a function of latitude. The latitudinal profile for the heavily averaged nighttime R' in the surrogate calibration layer showed good repeatability over a six-month period, which confirms its utility as a surrogate calibration target. Comparisons of the latitudinal profiles for the daytime and nighttime extended averages were then used to define latitude-dependent calibration scaling factors.

Powell et al. (2008) used this method to develop a 5-point latitudinal correction, which was later incorporated in V2. *Powell et al.* (2010) refined this method with a 34-point latitudinal correction, which was later incorporated in V3.01. However, in V3.01, the baseline 34-point correction table is continually updated using the same methodology as above, except for comparing daytime and nighttime values of R' on consecutive orbits.

Extensive validations of V3.01 have been conducted against an airborne pulsed lidar, the High Spectral Resolution Lidar (HSRL, *Burton et al.*, 2010), which is self-calibrated to an accuracy of 1-2%. Results, as reported in *Powell et al.* (2010), show that the mean daytime calibration for the 0.532-μm parallel channel is now within 3.5% of the HSRL calibration. This reference does not specify the aerosol backscatter magnitudes, vertical domains, horizontal averaging distances, or variability around the mean, for the cited validation results.

4.3.7 Detection Threshold: The V3.01 database will have considerable difficulty in detecting and quantifying the weak backscatter from aerosol targets in the middle and upper tropospheric (MUT) background aerosol system (§4.3.8 below), which is of special interest to this project. MUT aerosols are challenging targets to V3.01 for several reasons:

- For nighttime data, the standard 5-km integration distance, which does not provide high enough SNR to detect much, if any, of the MUT background;
- For daytime data, further degraded detection thresholds due to increased background noise;
- For all data, the assumption that layers above 8-12 km are aerosol free;
- For all data, the assumption that 8-12 km is the optimum calibration layer at all latitudes;

- For daytime data, the assumption of negligible diurnal change in 8-12 km aerosols; and
- For daytime data, the assumption that truncates the calibration correction when $R'_{night} < 1.03$.

Under these constraints, weak scattering from MUT aerosols is difficult to distinguish from random noise, weak synchronous noise, or fluctuating violations of one or more calibration assumptions. For example, the extensive averaging in *Powell et al.* (2009) and *Powell et al.* (2010) clearly reveals statistically significant but intermittent aerosol contamination in the overlying stratosphere, especially in the tropics, as indicated where $R'_{night} < 1.0$ due to increased extinction by stratospheric aerosols. Both studies also indicate significant aerosol contamination in the 8-12 km surrogate calibration layer, as indicated where $R'_{night} > 1.0$. Contamination in this layer increases with latitude: from below, due to increased convective lofting and extensive dilution of surface-sourced aerosols; and from above, where the tropopause can drop into or below the layer boundaries, and place stratospheric aerosols in the calibration layer. In the lower layer, if aerosol backscatter values were logarithmically distributed, the heavily averaged R' quantities would be substantially biased by the largest values in that distribution.

However, for the purposes of this study, these results should be viewed as positive, rather than negative. They demonstrate that substantial increases in vertical and horizontal averaging can improve the detectability of otherwise sub-threshold aerosol backscatter in the MUT on spatial scales of 200 km, reasonably comparable to the spatial scale for independent wind estimates from GWOS. Moreover, the routine production of these block-averaged R' values for daytime calibration purposes shows that the CALIOP data processing system already has the methods, tools, and funding to create these ancillary data products, Access to these block averages, which are presumably archived, would be highly beneficial to this project.

4.3.8 Middle and Upper Tropospheric Background Aerosol System: During the 1980's and early 1990's, NASA's Global Backscatter Experiment (GLOBE) identified and characterized a global-scale background aerosol system in the middle and upper troposphere (MUT, see details in Appendix C). Background backscatter values were low enough, and occurred frequently enough, to drive the space-based DWL effort toward the HDWL concept. However, during the two decades since the completion of the GLOBE measurement program, no other aerosol measurement programs have been conducted with the resources that would be required to update the GLOBE results. It is noteworthy that this same period has also been marked by dramatic increases in surface-sourced long-distance aerosol transport from urban/industrial pollution, biomass burning, and desertification. Those increases have not been large enough to suppress the global-scale geophysical cycles that create the extremely stable and resilient MUT aerosol background, and probably not even large enough to modulate those cycles. However, the increases may well have been large enough to increase mixing contamination of the background after its original production. Based on the trends described in Appendix C, such contamination could reasonably be expected to have significantly suppressed the low-backscatter tails of the background mode and enhanced the high-backscatter tails, and possibly even to have increased its modal values. Any or all of these secular trends would be highly significant to GWOS.

The CALIOP mission has provided the global scale spatial and temporal coverage needed to characterize the background MUT aerosol system. Moreover, the discussion in §4.3.7 above suggests that extensive averaging of the CALIOP data might detect and even quantify a portion of the MUT background, especially the high-backscatter tail. Further study will be required to determine how much averaging is required, how deeply the tails can be probed, and how multiple interferents can be minimized to improve MUT characterization.

4.4 Effects of Uncertainties on GWOS Simulations

4.4.1 Aerosol Types: For dry conditions, the backscatter color ratios between 0.532 μm and 2.0 μm fall into two broad categories: anthropogenic (smoke, 15.15; polluted continental, 14.14, and polluted dust, 10.0) and clean (clean marine, 5.81; clean continental, 4.93; and dust, 5.74). For the aerosol types within each category, the relative humidity response curves also show considerable similarity. (Dust and polluted dust are missing because those aerosol types are initially treated as non-hygroscopic.) Except for dust, trends are even more similar for the color ratios between 0.355 μm and 0.532 μm (anthropogenic: smoke, 1.90; polluted continental, 2.09; polluted dust, 2.19; and clean: clean marine, 1.13; clean continental, 1.58; dust, 2.36). In general, differences within categories are undoubtedly smaller than the propagated uncertainties in the physical, chemical, and optical parameters for each aerosol type. GWOS simulations that are based on conversion of CALIOP data to 2.0 μm might consider only the two broad aerosol types, anthropogenic and clean, and their associated color ratios, except for potential backscatter enhancements at 2.0 μm due to coated dust. Similarly, GWOS simulations that are based on conversion of CALIOP data to 0.355 μm might even consider only one color ratio, unless accurate accounting for organic aerosols made a significant difference in the color ratios for polluted aerosols. These simplified aerosol types and color ratios could be used for screening simulations; the full set of aerosol types and color ratios should be used for refined simulations, where the differences in such details could be significant. See §4.1 (How Good is Good Enough?), for guidance on the importance of aerosol model uncertainties.

4.4.2 Relative Humidity Effects: As noted in §4.2.2, backscatter color ratios have three basic regimes: (a) low humidity, where each CALIOP aerosol type shows essentially constant ratios; (b) increasing humidity, where the ratios change slowly but steadily for most aerosol types (except for curious fluctuations for some aerosols); and (c) near saturation, where the ratios change rapidly for most aerosol types. Using the same rationale as in §4.4.1 above, the second regime could be combined with the first for most aerosol types, with each combined regime having a roughly constant color ratio.

The third regime, where some color ratios have a much larger dynamic range, could be more problematic. However, in GWOS simulations that are based on currently available nature runs (see §4.4.4), the meteorological models that generate the global wind fields have considerable difficulty in generating humidity fields near saturation. Under these conditions, the GWOS simulations might not encounter high humidity often enough for the color-ratio uncertainty in this area to have a significant effect on the simulated performance or the simulated NWP impact. This issue should be revisited for global models that can develop realistic high-humidity fields.

4.4.3 CALIOP-Driven Simulations: GWOS simulations can ingest aerosol data from several sources. For example, CALIOP-driven simulations would use CALIOP-derived backscatter values and spatial/temporal distributions that are embedded in the diagnosed meteorological fields for the time periods when the CALIOP measurements were obtained. This approach ensures internal consistency between the input aerosol fields and the meteorological conditions that generated the aerosol fields. However, CALIOP data are available only in widely-spaced vertical curtains under the CALIOP ground track. The resulting aerosol fields would be suitable only for GWOS simulations that had similar ground coverage, as from a single track of fore and aft shots. From this perspective, it is noteworthy that some research groups have attempted to assimilate CALIOP data into chemical transport models (CTM) for atmospheric aerosols (*Sekiyama et al.*, 2009, 2010*; Campbell et al.*, 2009). The gridded 4-dimensional aerosol fields from these CALIOP-driven CTM's could be used to generate gridded 4-dimensional aerosol backscatter fields for inputs to GWOS simulations that required greater spatial/temporal coverage. However, CALIOP-driven simulations are not always possible, as explained in the next paragraph.

4.4.4 CALIOP-Informed Simulations: Most GWOS simulations will operate on meteorological fields that are generated in so-called "nature runs". In the absence of an aerosol-based CTM that operates on meteorological fields from the nature run, aerosol fields in the GWOS simulations will be decoupled, and eventually decorrelated, from the meteorological fields in which they are embedded. Under these conditions, most of the rigorous simulations for GWOS and its predecessor DWL concepts have been based on aerosol climatologies or limiting-case aerosol models (background and enhanced) derived from the GLOBE program, with backscatter variability statistically slaved to variability in the water vapor fields in the nature run. CALIOP-informed simulations use CALIOP-derived statistics, trends, and phenomenological correlations to generate aerosol backscatter fields that exhibit improved coupling with the meteorological fields in the nature run. These CALIOP-informed simulations would undoubtedly generate more realistic GWOS simulations and NWP impact assessments.

5. Summary and Conclusions

5.1 Key results: UAH has developed an aerosol scattering model that computes volume backscatter coefficient, volume extinction coefficient, volume scattering coefficient, single-scatter albedo, and lidar ratio at a given wavelength and relative humidity, for a given aerosol concentration, size distribution, and composition. We have applied the scattering model to the physical, chemical, and optical properties in the six CALIOP aerosol models at the two CALIOP wavelengths. We have also applied the scattering model to the CALIOP aerosol models with aerosol optical constants extrapolated to the two GWOS wavelengths. We have used the computed scattering properties at the four wavelengths to derive color ratios for each aerosol parameter for each pair of the four wavelengths in the study. We have presented detailed results of these computations for the volume backscatter coefficients from each pair of wavelengths, in terms of the backscatter color ratio and wavelength exponent as a function of relative humidity, in graphical form, and the wavelength exponent for dry aerosols, in tabular form. We have also included selected samples of other computed scattering parameters, to clarify and explain the observed trends.

The modeled backscatter color ratios and their wavelength exponents show considerable variability with aerosol type, relative humidity, and wavelength pairs. However, much of that variability can be parameterized simply by the color ratio exponent α. From this perspective, for most wavelength pairs the backscatter variability at low relative humidity falls into two basic classes: *clean*, with α of order unity, and *anthropogenic*, with α of order 2. Relative humidity growth curves show three rough classes: low humidity, where backscatter values, color ratios, and exponents show little or no variability; intermediate humidity, where these quantities show significant trends that are difficult to generalize or explain; and high humidity, where backscatter ratios for some aerosol types increased or decreased rapidly, but remained relatively flat for other aerosol types. However, α values generally showed less dependence on relative humidity than on aerosol type. These results suggest that aerosol source classification will be much less important than other factors in GWOS simulations, for conditions with moderate to high backscatter.

5.2 Key uncertainties: This study identified key uncertainties in the CALIOP data processing, in the preliminary UAH aerosol model, and, to a lesser extent, in the CALIOP aerosol models. The most important data processing uncertainties were due to assumptions that degraded the end-to-end detection sensitivity for CALIOP, especially the assumptions that were required for empirical corrections to the thermal misalignment problem. The most important uncertainties in the UAH aerosol model arose from the necessarily incomplete treatment of potential backscatter enhancements at 2 μm due to coated dust and at 0.355 μm due to complex organic mixtures in polluted airmasses. The CALIOP aerosol models used some questionable optical constants, but we believe that these assumptions were generally not critical. Additional details on these issues are discussed below in §5.4, Need for New Work.

5.3 Key GWOS implications: The results of this study will provide valuable inputs to GWOS simulations. The modeled color ratios for aerosol backscatter and extinction can be applied to the CALIOP database at either of two levels: (a) measured attenuated backscatter; or (b) derived backscatter and extinction. In both cases, the conversions can be applied to the diagnosed aerosol subtypes in the backscatter and extinction database. However, it is noteworthy that conversions applied directly to attenuated backscatter can use UAH-provided improvements to the CALIOP aerosol models, instead of using the CALIOP aerosol models as is, because the CALIOP models are not needed to derive the attenuated backscatter. Color ratios for certain groupings of aerosol subtypes show enough similarity that the six aerosol types could be reduced to two (clean and polluted) for conversion to backscatter at 2 μm, and possibly even to one composite aerosol type for conversion to backscatter at 0.355 μm, if desired for rapid GWOS screening runs. However, GWOS simulations that require rigorous justification, and simulations that explore more subtle NWP impacts, should use the full set of aerosol types and conversion factors.

5.4 Need for new work: This study shows that additional work is needed to reduce the uncertainties in CALIOP-driven aerosol backscatter and extinction models at GWOS wavelengths near the GWOS threshold. The needed studies fall into three general categories, as summarized below, with embedded assessments of relative priority.

5.4.1 Improved CALIOP Detection Threshold: The current study showed promising but inconclusive evidence that the CALIOP database might have valuable information content that is yet untapped in the large domains that are currently characterized by a high percentage of data dropouts. To explore this untapped domain, we recommend investigations in the following areas:

- Improve the CALIOP detection threshold by extensive vertical and horizontal averaging in the data dropout domain. Ensure that upstream assumptions and data processing methods (such as the empirical correction for thermal misalignment in the new Version 3.01 database) do not invalidate the value gained by extended averaging in these challenging regions.
- Explore the potential information content in CALIOP data dropouts that might remain in the objectively processed data, even after extensive horizontal and vertical averaging.
- Begin this exploration by analyzing the database of block averages for total attenuated aerosol backscatter in the 8-12 km layer. These data have recently been created to enable routine calibration transfer from nighttime to daytime data products in V3.01.

5.4.2 Improved CALIOP Aerosol Models: The UAH study revealed some significant limitations in the CALIOP aerosol models. Using the guidelines in §4.1 (How Good is Good Enough?), we expect that further research in this area would be useful only to the extent that it reduces systematic errors in the backscatter retrievals that are near but above the current backscatter detection threshold, and in future backscatter retrievals that are currently near but below the CALIOP threshold. We base this conclusion on the backscatter conversion equations in Appendix A, which show that we do not have to perform backscatter conversions on retrieved backscatter values; we can also perform those conversions on the attenuated backscatter values.

Under these conditions, we expect that updating the CALIPSO aerosol models, and reprocessing the attenuated backscatter solely for the benefit of those updated models, would probably not be necessary, realistic, or productive. However, if the CALIPSO data are reprocessed for other reasons, such as for improved detection thresholds as recommended in §5.4.1 above, then the reprocessing could use improved aerosol models that incorporate the critique elsewhere in this report.

If extensive integration does indeed improve the detection threshold, then CALIOP data might begin to include the high-backscatter tail of the MUT aerosol background system. The CALIOP aerosol models do not currently include an MUT aerosol model, which has radically different physical, chemical, and optical properties than all of the other CALIOP models. So, in principle, an MUT aerosol model might be needed for the backscatter retrieval algorithm and related data processing. UAH has a long heritage of experience in the measurement and modeling of MUT background aerosols. However, MUT aerosol concentrations are so low that MUT aerosol extinction is very weak, and explicit MUT models might not be required.

5.4.3 Improved UAH Aerosol Models: The UAH aerosol models were based on the CALIOP aerosol models, to ensure consistency with CALIOP backscatter retrievals. Although these models were useful, the study showed that several improvements are warranted, especially because aerosol modeling at the GWOS wavelengths involves the potential for significant aerosol backscatter enhancements that are not active at CALIOP wavelengths, and, therefore, did not need to be considered in the CALIOP aerosol models. Thus, the UAH model needs additional work in the effects of organic aerosols on backscatter enhancements at 0.355 μm and the effects of sulfate-coated dust at 2 μm. These studies should also investigate nonsphericity effects. These enhancements, if verified first with expanded theoretical studies, and then validated in the laboratory, could have significant effects on GWOS performance in elevated dust and pollution plumes that have been heavily diluted by MUT background airmasses.

The UAH models currently show the effects of relative humidity on backscatter, extinction, and CALIOP-to-GWOS color ratios, in terms of simple line graphs. For several important aerosol types, these graphs show large high-frequency oscillations. We need to understand the source of these oscillations, and, in particular, to determine whether they are spurious computational artifacts, or whether they do, indeed, originate from complex “optical glory” phenomena. In either case, the final RH curves then need to be converted either to lookup tables or to simple parameterizations for optimal use in GWOS simulations.

Although an MUT aerosol model is probably not required for improved CALIOP data processing, such a model is needed for improved GWOS simulations. Development of such a model would require intensive literature surveys on aerosol research programs conducted after the GLOBE flights in 1989/1990, to search for and synthesize any evidence that the MUT background might have undergone small but important changes during the past two decades. The updated MUT model must also account for any backscatter enhancements due to organics at 0.355 μm and to coated dust at 2 μm, in elevated but heavily diluted plumes.

Overall, the improved UAH aerosol model would provide improved color ratios between CALIOP and GWOS wavelengths for CALIOP-driven and CALIOP-informed GWOS simulations. Equally importantly, it would also provide improved direct inputs to GWOS simulations that do not need to use CALIOP data.

5.5 Next Generation Aerosol Modeling for GWOS Simulations: As noted in §4.4.3 and §4.4.4, the ideal GWOS simulation should use aerosol backscatter fields that are consistent with the wind fields and other gridded meteorological fields that the GWOS lidars probe. Most of these simulations operate on nature runs, so the aerosol backscatter fields should be physically, chemically, and optically consistent with the nature runs. Since the nature runs are decoupled from and decorrelated with any real atmosphere, the meteorological fields in the nature runs would also be decoupled from and decorrelated with any gridded aerosol backscatter fields from the real atmosphere. Previous studies have used global-scale statistics and climatologies for aerosol backscatter from GLOBE and other atmospheric field programs, with physically reasonable but not rigorous attempts to correlate those climatologies to the meteorological fields in the nature run. The objective of the current study is to replace previous climatologies with phenomenological correlations and statistical climatologies derived from CALIOP.

The next logical step would be to replace prescribed phenomenological correlations with aerosol fields that are created by a chemical transport model (CTM), which continually uses the meteorological fields from the nature run. The ideal CTM should employ advection algorithms that minimize spurious numerical diffusion, which would otherwise overwhelm and suppress the background aerosol system in the MUT. Previous studies on trace constituent transport have shown that Eulerian, spectral, and Lagrangian bubble models are inadequate for this task, due to extreme and highly unphysical numerical diffusion and the very large dynamic range that aerosol backscatter exhibits in the atmosphere . The ideal CTM candidate would be a hybrid isentropic model, which uses isentropic transport above the PBL and Eulerian transport in the PBL, and which preserves global entropy. These models have been shown to preserve the large dynamic range in trace constituent concentrations that are needed to generate and maintain a realistic MUT background aerosol system. GWOS simulations could be conducted with aerosol fields generated by non-ideal advection algorithms, but only if all parties clearly understood that these algorithms would almost certainly generate unrealistically high aerosol concentrations in the free troposphere.

After the CTM has generated realistic fields of aerosol concentration and composition, the final step is to convert these modeled fields to aerosol backscatter and extinction coefficients, and thence to attenuated backscatter, at the GWOS wavelengths. This step would probably use lookup tables or simple parameterizations of aerosol backscatter and extinction per unit mass for each aerosol subtype, rather than explicit Mie scattering computations, which would require unrealistically large CPU burdens. UAH aerosol expertise could contribute to such studies.

The current CALIOP-based study has been a logical and useful steppingstone to the next generation aerosol of aerosol inputs for realistic GWOS simulations. Preliminary studies of this kind are underway elsewhere; and the UAH model can also be used in those studies.

m_{real}	m_{im}	R_m	*GSD*	type		ff	m_{real}	m_{im}	R_m	*GSD*	type	
1.414	0.0036	0.1165	1.4813	dust		0.223	1.414	0.0036	2.8329	1.9078	dust	
1.517	0.0234	0.1436	1.5624	smoke		0.329	1.517	0.0234	3.7260	2.1426	smoke	
1.380	0.0001	0.2056	1.6100	Clean cont	**F532**	0.05	1.380	0.0001	2.6334	1.8987	Clean cont	**C532**
1.404	0.0063	0.1577	1.5257	Poll cont		0.531	1.404	0.0063	3.5470	2.0650	Poll cont	
1.400	0.0050	0.1500	1.6000	Clean Mar		0.025	1.400	0.0050	1.2160	1.6000	Clean Mar	
1.452	0.0109	0.1265	1.5112	Poll dust		0.241	1.452	0.0109	3.1617	1.9942	Poll dust	

m_{real}	m_{im}	R_m	*GSD*	type		density	m_{real}	m_{im}	R_m	*GSD*	type	
1.495	0.0043	0.1165	1.4813	dust		2.5 g/cc	1.495	0.0043	2.8329	1.9078	dust	
				8.48E+00							**9.84E-04**	
1.541	0.0298	0.1436	1.5624	smoke		1.1	1.541	0.0298	3.7260	2.1426	smoke	
				1.33E+01							**6.41E-04**	
1.380	0.0001	0.2056	1.6100	Clean cont		1.8	1.380	0.0001	2.6334	1.8987	Clean cont	
				3.87E-01	**F1064**						**2.11E-03**	**C1064**
1.439	0.0073	0.1577	1.5257	Poll cont		1.8	1.439	0.0073	3.5470	2.0650	Poll cont	
				1.05E+01							**3.42E-04**	
1.400	0.0050	0.1500	1.6000	Clean Mar		2.5	1.400	0.0050	1.2160	1.6000	Clean Mar	
				3.65E-01							**2.67E-02**	
1.512	0.0137	0.1265	1.5112	Poll dust		2.5	1.512	0.0137	3.1617	1.9942	Poll dust	
				6.82E+00							**6.12E-04**	

Table 1: Aerosol parameters from *Omar et al*, 2009, that were fed into the bimodal aerosol optics model. Shown are the real and imaginary parts of the complex refractive index, m_{real} and m_{im}, along with mean radius R_m, and geometric standard deviation GSD of the distributions for fine and coarse modes. The fractional mass of the fine modes is given in the ff column. The numbers in blue are the number concentrations (#/cc) for the respective modes, as derived from ff and the assumed densities (g/cc, also shown) of the aerosol materials.

References

1. Bohren, C.F., and D.R. Huffman, 1983: Absorption and Scattering of Light by Small Particles. John Wiley and Sons. New York. 530 pp.

2. Burton, S. P., R. A. Ferrare, C. A. Hostetler, J. W. Hair, C. Kittaka, M. A. Vaughan, M. D. Obland, R. R. Rogers, A. L. Cook, D. B. Harper, and L. A. Remer, 2010: "Using Airborne High Spectral Resolution Lidar Data to Evaluate Combined Active Plus Passive Retrievals of Aerosol Extinction Profiles", *J. Geophys. Res.*, doi:10.1029/2009JD012130.

3. Campbell, J. R., J. S. Reid, D. L. Westphal, J. Zhang, E. J. Hyer, and E. J. Welton, 2009: CALIOP aerosol subset processing for global aerosol transport model data assimilation, *J. Selected Topics Appl. Earth Obs. Rem. Sens.*, in press.

4. Greenler, R., 1980: Rainbows, Haloes, and Glories. Cambridge University Press. New York.

5. Huffman, D. R. and C. F. Bohren, 1979: "Infrared Absorption Spectra of Non-Spherical Particles Treated in the Rayleigh-Ellipsoid Approximation". In: Light scattering by irregularly shaped particles; Proceedings of the International Workshop, Albany, N.Y., June 5-7, 1979. (A80-49156 21-70) New York, Plenum Press, 1980, p. 103-111.

6. Hunt, W. H, D. M. Winker, M. A. Vaughan, K. A. Powell, P. L. Lucker, and C. Weimer, 2009: "CALIPSO Lidar Description and Performance Assessment", *J. Atmos. Oceanic Technol.*, **26**, 1214-1228, doi:10.1175/2009JTECHA1223.1.

7. Omar, A., D. Winker, C. Kittaka, M. Vaughan, Z. Liu, Y. Hu, C. Trepte, R. Rogers, R. Ferrare, R. Kuehn, C. Hostetler, 2009: "The CALIPSO Automated Aerosol Classification and Lidar Ratio Selection Algorithm", *J. Atmos. Oceanic Technol.*, **26**, 1994-2014, doi:10.1175/2009-JTECHA1231.1.

8. Powell, K. A., C. A. Hostetler, Z. Liu, M. A. Vaughan, R. E. Kuehn, W. H. Hunt, K. Lee, C. R. Trepte, R. R. Rogers, S. A. Young, and D. M. Winker, 2009: "CALIPSO Lidar Calibration Algorithms: Part I - Nighttime 532 nm Parallel Channel and 532 nm Perpendicular Channel", *J. Atmos. Oceanic Technol.*, **26**, 2015-2033, doi:10.1175/2009-JTECHA1242.1.

9. Powell, K. A., M. A. Vaughan, R. E. Kuehn, W. H. Hunt, and K-P. Lee, 2008: "Revised Calibration Strategy for the CALIOP 532-nm Channel – Part II - Daytime". ***Reviewed and Revised Papers Presented at the 24th International Laser Radar Conference*****, 1177-1180, ISBN 978-0-615-21489-4.**

10. Powell, K. A., M. A. Vaughan, R. R. Rogers, R. E. Kuehn, W. H. Hunt, K-P. Lee, and T. D. Murray, 2010: "The CALIOP 532-nm Channel Daytime Calibration: Version 3 Algorithm". ***25th International Laser Radar Conference: St. Petersburg, Russia*****.**

11. Winker, D. M., M. A. Vaughan, A. H. Omar, Y. Hu, K. A. Powell, Z. Liu, W. H. Hunt, and S. A. Young, 2009: "Overview of the CALIPSO Mission and CALIOP Data Processing Algorithms", *J. Atmos. Oceanic Technol.*, **26**, 2310-2323, doi:10.1175/2009JTECHA1281.1.

12. Rothermel, J., D.A. Bowdle, J.M. Vaughan, and M.J. Post, 1989: "Evidence of a tropospheric aerosol backscatter background mode". *Appl. Opt*., **28**, 1040-1042 (1989).

13. Sekiyama, T. T., T. Y. Tanaka, A. Shimizu, and T. Miyoshi, 2009: "Data assimilation of CALIPSO aerosol observations", *Atmos. Chem. Phys. Discuss.*, **9**, 5785-5808.

14. Sekiyama, T. T., T. Y. Tanaka, A. Shimizu, and T. Miyoshi, 2010: "Data assimilation of CALIPSO aerosol observations", Atmos. Chem. Phys., 10, 39–49.

15. Winker, D., Y. Hu, M. Pitts, J. Tackett, C. Kittaka, Z. Liu and M. Vaughan, 2010: "CALIPSO at Four: Results and Progress". ***25th International Laser Radar Conference: St. Petersburg, Russia.***

APPENDIX A: Aerosol Backscatter Wavelength Conversion Equation

David A. Bowdle

Earth Systems Science Center

University of Alabama in Huntsville

Expressing wavelength conversions in a non-dimensional manner allows cancellation of terms that are unknown or difficult to estimate. It also avoids unit conversion errors, because the units also cancel.

$$
\begin{aligned}
&\beta(\lambda_{GWOS}, S_{both})\, T^2(\lambda_{GWOS}, \theta_{GWOS}, \Delta\Omega_{GWOS}, S_{both}) \\
&= \beta(\lambda_{CAL}, S_{both})\, T^2(\lambda_{CAL}, \theta_{CAL}, \Delta\Omega_{CAL}, S_{both}) \\
&\times \left\{ \frac{\beta(\lambda_{GWOS}, S_{both})}{\beta(\lambda_{CAL}, S_{both})} \right\} \cdot \left\{ \frac{T^2(\lambda_{GWOS}, \theta_{GWOS}, \Delta\Omega_{GWOS}, S_{both})}{T^2(\lambda_{CAL}, \theta_{CAL}, \Delta\Omega_{CAL}, S_{both})} \right\}
\end{aligned}
\quad ,
$$

where

β	= Aerosol volume backscatter coefficient
T	= Atmospheric transmission, all constituents, slant path, single pass
λ	= Lidar wavelength
θ	= Lidar nadir angle
$\Delta\Omega$	= Lidar field of view (FOV)
S	= Lidar scene (ignoring differences in θ and $\Delta\Omega$)
GWOS	= Global Wind Observing System (Hybrid Doppler Wind Lidar)
CAL	= CALIOP on CALIPSO
both	= Applies to both GWOS and CALIOP

$$\left\{\frac{T^2(\lambda_{GWOS},\theta_{GWOS},\Delta\Omega_{GWOS},S_{both})}{T^2(\lambda_{CAL},\theta_{CAL},\Delta\Omega_{CAL},S_{both})}\right\}=$$

$$\left\{\frac{T^2(\lambda_{GWOS},\theta_{GWOS},\Delta\Omega_{GWOS},S_{both})}{T^2(\lambda_{CAL},\theta_{GWOS},\Delta\Omega_{GWOS},S_{both})}\right\}\times\left\{\frac{T^2(\lambda_{CAL},\theta_{GWOS},\Delta\Omega_{GWOS},S_{both})}{T^2(\lambda_{CAL},\theta_{CAL},\Delta\Omega_{CAL},S_{both})}\right\}$$

Conversion factor for atmospheric transmission, including clouds, aerosols, and trace gases, evaluated at the GWOS nadir angle and field of view, but assumed to be independent of θ and $\Delta\Omega$	Conversion factor for nadir angle slant-path, cloud-free line of sight (CFLOS), and differential field of view, evaluated at CALIOP wavelength, but assumed to be wavelength-independent

$$\left\{\frac{\beta(\lambda_{GWOS},S_{both})}{\beta(\lambda_{CAL},S_{both})}\right\}=$$

$$\frac{\left\{\int\limits_{fine}\left\{\frac{\sigma(a,\lambda_{GWOS},S_{both})}{v(a)}\right\}\cdot\left\{\frac{dV(a)}{d\log a}\right\}_{fine}d\log a\right\}+\left\{\int\limits_{coarse}\left\{\frac{\sigma(a,\lambda_{GWOS},S_{both})}{v(a)}\right\}\cdot\left\{\frac{dV(a)}{d\log a}\right\}_{coarse}d\log a\right\}}{\left\{\int\limits_{fine}\left\{\frac{\sigma(a,\lambda_{CAL},S_{both})}{v(a)}\right\}\cdot\left\{\frac{dV(a)}{d\log a}\right\}_{fine}d\log a\right\}+\left\{\int\limits_{coarse}\left\{\frac{\sigma(a,\lambda_{CAL},S_{both})}{v(a)}\right\}\cdot\left\{\frac{dV(a)}{d\log a}\right\}_{coarse}d\log a\right\}}$$

where

σ	= Aerosol backscatter cross-section, single particle
a	= Particle radius
v	= Aerosol volume, single particle
V	= Aerosol volume, cumulative
fine	= Fine mode of the aerosol size distribution
coarse	= Coarse mode of the aerosol size distribution

In this form of the backscatter estimation integral, the bracketed volume- (or mass-) weighted products in each integrand have a much smaller dynamic range than do their counterparts in the traditional number-weighted integral shown in §2.5. At each wavelength, the backscatter cross-section per unit particle volume has three basic domains:

$\propto a^3$ for $a \ll \lambda$,

$$\propto a^{-1} \text{ for } a >> \lambda,$$

roughly constant for some intermediate values.

For each mode (fine and coarse), the volume-weighted aerosol size distribution is often approximated as a lognormal distribution, as in §2.5. Thus, each integrand above is the product of two strongly peaked functions, where both peaks occur near the same range of particle sizes. The backscatter color ratio for the bimodal size distribution arises from the wavelength dependence of the peak in the backscatter cross-section per unit particle volume, with respect to the peak in the volume-weighted aerosol size distribution, across each mode in the aerosol size distribution.

APPENDIX B: CALIOP Calibration Equation

David A. Bowdle

Earth Systems Science Center

University of Alabama in Huntsville

$$\left\{1+\frac{\beta_{aer}(\lambda_1,\phi_\parallel,z,y_p)}{\beta_{mol}(\lambda_1,\phi_\parallel,z,y_p)}\right\}\times T_{aer}^2\left[\lambda_1,\phi_\parallel,r\left[z,\theta(\lambda_1,\phi_\parallel,y_p)\right]\right]=$$

$$\left\{\begin{aligned}
&\left\{\frac{1}{27}\right\}\sum_{k-13}^{k+13}\left\{\frac{1}{j_{30km}-j_{34km}+1}\right\}\sum_{j=j_{30km}}^{j=j_{34km}}\left\{\frac{1}{11}\right\}\sum_{i=11k-5}^{i=11k+5}\times\left\{\frac{\hat{\eta}(\lambda_1,\phi_\parallel,z,\theta[\lambda_1,\phi_\parallel,y_p])}{\ddot{\eta}(\lambda_1,\phi_\parallel,z_j,\theta[\lambda_1,\phi_\parallel,y_i])}\right\}\\
&\left[\left\{1+\frac{\hat{\beta}_{aer}(\lambda_1,\phi_\parallel,z_j,y_k)}{\hat{\beta}_{mol}(\lambda_1,\phi_\parallel,z_j,y_k)}\right\}^{-1}\times\hat{T}_{aer}^2\left[\lambda_1,\phi_\parallel,r\left[z_j,\theta(\lambda_1,\phi_\parallel,y_k)\right]\right]\right]\times\left\{\frac{\hat{\beta}_{mol}(\lambda_1,\phi_\parallel,z,y_p)}{\hat{\beta}_{mol}(\lambda_1,\phi_\parallel,z_j,y_k)}\right\}\\
&\times\left\{\frac{\hat{T}_{mol}\left[\lambda_1,\phi_\parallel,r\left[z,\theta(\lambda_1,\phi_\parallel,y_p)\right]\right]}{\hat{T}_{mol}\left[\lambda_1,\phi_\parallel,r\left[z_j,\theta(\lambda_1,\phi_\parallel,y_k)\right]\right]}\right\}^2\times\left\{\frac{\hat{T}_{O_3}\left[\lambda_1,\phi_\parallel,r\left[z,\theta(\lambda_1,\phi_\parallel,y_p)\right]\right]}{\hat{T}_{O_3}\left[\lambda_1,\phi_\parallel,r\left[z_j,\theta(\lambda_1,\phi_\parallel,y_k)\right]\right]}\right\}^2\\
&\times\left\{\frac{S(\lambda_1,\phi_\parallel,z_j,y_i)-S^0(\lambda_1,\phi_\parallel,z_j,y_i)}{S(\lambda_1,\phi_\parallel,z,y_p)-S^0(\lambda_1,\phi_\parallel,z,y_p)}\right\}\times\left\{\frac{r(z_j,y_i)}{r(z,y_p)}\right\}^2\\
&\times\left\{\frac{E(\lambda_1,\phi_\parallel,y_p)}{E(\lambda_1,\phi_\parallel,y_i)}\right\}\times\left\{\frac{G(\lambda_1,\phi_\parallel,z,y_p)}{G(\lambda_1,\phi_\parallel,z_j,y_i)}\right\}
\end{aligned}\right\}^{-1}$$

Lidar equation, with implicit calibration, in the form used to detect statistically significant aerosol and cloud layers. The detection algorithm iteratively searches for departures from unity in the profile term on the left-hand side, working from the highest altitude and moving down.

β = volume backscatter coefficient	*y* = ground- track coordinate
T = one-way slant-path transmittance	θ = lidar pointing direction
G = amplifier gain	*aer* = aerosol
η = optical system efficiency	*mol* = molecular

λ_1 = laser wavelength – 0.532 μμm	O_3 = ozone
$\phi_{\|\|}$ = polarization - parallel	*i* = index, dummy, ground track
S = digitized signal; ^{0} = background	*j* = index, dummy, altitude
r = range from lidar	*k* = index, 5-km block
z = altitude	k_p = index, laser pulse

$\left\{1+\frac{\beta_{aer}(\lambda_1,\phi_\parallel,z,y_p)}{\beta_{mol}(\lambda_j,\phi_n,z,y_p)}\right\}\times\left[T_{aer}(\lambda_1,\phi_\parallel,r),\theta(\lambda_1,\phi_\parallel,y_p)\right]^2$	$\left\{\frac{S(\lambda_1,\phi_\parallel,z_j,y_i)-S^0(\lambda_1,\phi_\parallel,z_j,y_i)}{S(\lambda_1,\phi_\parallel,z,y_p)-S^0(\lambda_1,\phi_\parallel,z,y_p)}\right\}$
Derived Atmospheric Quantities	Measured Signals, with Background Correction

The data processing algorithm assumes that offset removal in the digitized signal removes detector dark noise, scene radiance, and offsets in the detector/amplifier/digitizer chain. This top-level assumption requires several underlying assumptions, some explicitly stated, and some implicit.	
Each detector/amplifier/digitizer chain is linear over its entire dynamic range, so the ADC operator is distributive.	The electronically subtracted background and added DC offset are constant throughout the profile (except for random noise).
Each detector/amplifier/digitizer chain has an offset that is constant throughout the profile (except for random noise).	Aerosol and molecular scattering are negligible in the altitude range from 97-112 km (analog background subtraction layer).
Detector dark noise and scene radiance are constant throughout the entire profile (except for random noise).	Aerosol and molecular scattering are negligible in the altitude range from 65-80 km (offset measurement layer).

$\left\{\frac{\hat{\beta}_{mol}(\lambda_1,\phi_\|,z,y_p)}{\hat{\beta}_{mol}(\lambda_1,\phi_\|,z_j,y_k)}\right\}$ $\left\{\frac{\hat{T}_{mol}(\lambda_1,\phi_\|,r(z),\theta(\lambda_1,\phi_\|,y_p))}{\hat{T}_{mol}(\lambda_1,\phi_\|,r(z_j),\theta(\lambda_1,\phi_\|,y_k))}\right\}^2$ $\left\{\frac{\hat{T}_{O_3}(\lambda_1,\phi_\|,r(z),\theta(\lambda_1,\phi_\|,y_p))}{\hat{T}_{O_3}(\lambda_1,\phi_\|,r(z_j),\theta(\lambda_1,\phi_\|,y_k))}\right\}^2$	$\left\{1+\frac{\hat{\beta}_{aer}(\lambda_1,\phi_\|,z_j,y_k)}{\hat{\beta}_{mol}(\lambda_1,\phi_\|,z_j,y_k)}\right\}^{-1}$ $\left\{\hat{T}_{aer}(\lambda_1,\phi_\|,r(z_j),\theta(\lambda_1,\phi_\|,y_k))\right\}^2$ $\left\{\frac{\eta(\lambda_1,\phi_\|,z,\theta(\lambda_1,\phi_\|,y_p))}{\eta(\lambda_1,\phi_\|,z_j,\theta(\lambda_1,\phi_\| y_i))}\right\}$ $\left\{\frac{E(\lambda_1,\phi_\|,y_p)}{E(\lambda_1,\phi_\|,y_i)}\right\}$ $\left\{\frac{r(z_j,y_i)}{r(z,y_p)}\right\}^2 \times \left\{\frac{G(\lambda_1,\phi_\|,z,y_p)}{G(\lambda_1,\phi_\|,z_j,y_i)}\right\}$
<u>GMAO model</u> Bracketed terms, in general, are not unity All terms subject to NWP/CTM modeling errors	**<u>Terms of Order Unity</u>** Lines 1-2 assumed to be identically unity; stratospheric aerosols violate this assumption Line 3 assumed to be unity in Version 2; mismatched laser frequency and etalon passband; corrected for thermal misalignment in Version 3.01 Line 4 terms all known to high accuracy

UAH conducted a technical review on a series of CALIOP papers in the *Journal of Atmospheric and Oceanic Technology*. This review identified two types of errors: (a) effects that are irreversible due to instrument problems, problematic instrument settings, or onboard signal processing and data processing prior to downloading, and (b) effects that are potentially reversible on the ground after reprocessing.

Irreversible effects include:

- Long-term increase in the percentage of low energy laser shots (0.006% of total shots as of June 1, 2008), with the highest frequency of occurrence over the South Atlantic Anomaly.
- Long-term pulse energy decay in the primary laser (6% over two years) until the backup laser began operating in early 2009.
- Long-term alignment drift, which had decreased the 532 nm calibration coefficient by 13% up to late 2007, with restoration within 3% of its original value after realignment in February 2008.
- Long-term SNR decrease in the 1064 nm detector (SNR was 65% of original by June 1, 2008) due to cumulative radiation exposure.
- Large noise spikes, which were edited out when infrequent, but required historic calibrations when frequent, especially when radiation-induced over the South Atlantic Anomaly.
- Degradation of the minimum detectable backscatter due to solar background scene radiance.
- Degradation of retrievals below clouds due to transient response artifacts in the 532 nm detector.
- Potential degradation of interchannel calibrations (532 nm $\rightarrow$ 1064 nm) using backscatter from high-altitude cirrus clouds at an off-nadir angle of only 0.3° until November 2007 (not discussed in the JTech series).
- Potential degradation of retrievals for low aerosol backscatter due to minor non-linearity in the detector/amplifier/digitizer chain, where each detector has two independent amplifier/digitizer pairs to cover a very large dynamic range, including widely differing offset and gain settings for daytime and nighttime operations (not discussed in the JTech series).
- Potential degradation of electronic background removal and digital background measurement due to lightning events in the field of view. Could lightning also be responsible for some of the large noise spikes outside of the SAA 2007? (not discussed in the JTech series)

Potentially reversible effects include:

- Errors in backscatter calibration due to undiagnosed aerosol backscatter and extinction in the 30-35-km calibration layer. Known to occur in Version 2, especially in and near the tropics. Fixes were under development for future versions.
- Errors in backscatter calibration due to undiagnosed aerosol backscatter and extinction in the 8-12 km daylight calibration layer. Known to occur in Version 3.01, especially at middle and higher latitudes.
- Biases as large as 30% in the 532 nm calibration and the inter-channel calibrations (532 nm $\rightarrow$ 1064 nm) on orbital time scales, especially during the night$\rightarrow$day transition, due to thermal misalignment (analyzed and modeled, in part, for Version 2; improved in Version 3.01).
- Large biases in the inter-channel calibrations (532 nm $\rightarrow$ 1064 nm) on seasonal time scales and latitudinal spatial scales, due to as-yet undiagnosed and uncorrected effects.
- Errors in retrieving weak aerosol backscatter, due to GMAO model errors in ozone concentrations and in air temperature and pressure (air density) at the CALIPSO spatial and temporal resolution.
- Addition of a cloud-clearing index to the 80-km layer-average database.

- Addition of an aerosol model for the middle and upper troposphere, if the detection sensitivity can be improved enough to detect the high-backscatter tail of this feature.
- Improvements in the detection sensitivity by increased averaging in the vertical and horizontal (under study in this project (already used for daylight calibration in Version 3.01).
- Incorporation of new insights from a recently published paper on CALIPSO-HSRL comparisons.

APPENDIX C: Background Aerosol System in the Middle and Upper Troposphere

David A. Bowdle

Earth Systems Science Center

University of Alabama in Huntsville

1. Global Backscatter Experiment

During the 1980's and early 1990's, NASA conducted a comprehensive Global Backscatter Experiment (GLOBE, to provide improved inputs into performance simulations for the Laser Atmospheric Wind Sounder (LAWS), an early concept for a space-based Doppler wind lidar. The GLOBE program concentrated on the middle and upper troposphere (MUT), where wind measurements from LAWS were expected to have the greatest impact on global-scale numerical weather prediction models, but also where aerosol backscatter was expected to be low enough that those wind measurements might be most difficult to obtain. To properly characterize aerosol backscatter in the MUT, GLOBE required sensor platforms that provided direct access to the MUT; measurement programs that provided global-scale spatial and/or temporal coverage to ensure representative statistics in the MUT; aerosol sensors with low detection thresholds to minimize data dropouts; and multiple synergistic sensors to ensure that the observed statistical features represented real geophysical features, rather than measurement artifacts from a single sensor or class of sensors.

2. Generic Background Parameterization

The GLOBE program identified and quantified a global-scale background aerosol system in the MUT (*e.g.*, *Rothermel et al.*, 1989). To first order, the MUT background could be parameterized as follows:

$$PDF(M_{aer} \parallel \sigma_g, z, z_{\max}, z_{\min}) = \left\{ \frac{1}{\sqrt{2\pi}\ln(\sigma_g)} \right\} \exp\left\{ -\frac{1}{2} \left(\frac{\ln\left[R(M_{aer}, z) / R_0(z_{\max}, z_{\min})\right]}{\ln(\sigma_g)} \right)^2 \right\},$$

where *PDF* is the probability density function, M_{aer} is the aerosol mass concentration, σ_g is the geometric standard deviation, $R(M_{aer}, z) = M_{aer}(z)/\rho_{air}(z)$ is the aerosol mass mixing ratio, R_0 is the geometric mean of the aerosol mass mixing ratio, ρ_{air} is air density, *z* is altitude, and z_{max} and z_{min} are the maximum and minimum altitudes at which the parameterization is valid. In other words, the aerosol mass mixing ratio varied log-normally about a constant mass mixing ratio R_0 within the altitude layer from z_{max} to z_{min}. This feature is consistent with, and very likely originated from, gas-to-particle conversion from a widespread source with log-normally distributed source strength, followed by coagulation toward a temporally stable size distribution during subsidence and global distribution, in the absence of sources and sinks.

The atmospheric layer below z_{min} was characterized by a log-normal distribution around an aerosol mass mixing ratio that decreased exponentially with altitude, at vertical decay rates that varied with season, latitude, and underlying or upwind earth surface type. The layer above z_{max} was characterized by stratospheric aerosols. The layer boundaries, z_{max} and z_{min}, also varied with season, latitude, underlying or upwind earth surface type, and with local weather conditions. Background conditions normally dominated the MUT. However, it is noteworthy that the MUT could sometimes be occupied locally and temporarily by non-background features, including clouds, stratospheric aerosols, and surface-sourced aerosols. Recognizing the background as a Lagrangian airmass feature, rather than an Eulerian climatological feature, resolves this problem.

Again, to first order, the MUT background mode can also be expressed in terms of generic aerosol variables, ξ_{aer}, using the following expression:

$$PDF(\zeta_{aer} \,\|\, \sigma_g, z_{\max}, z_{\min}) = \left\{ \frac{1}{\sqrt{2\pi}\,\ln\left[\sigma_g\left(\zeta_{aer}\right)\right]} \right\} \exp\left\{ -\frac{1}{2} \left(\frac{\ln\left[R\left(\zeta_{aer}\right)/R_0\left(z_{\max}, z_{\min}\right)\right]}{\ln\left[\sigma_g\left(\zeta_{aer}\right)\right]} \right)^2 \right\},$$

where R now represents the mixing ratio for ξ_{aer}. This generic equation is strictly valid if, and only if, $d\zeta_{aer}/dM_{aer} = K_{\zeta_{aer}}$, where K is a constant. Under these conditions, the generic aerosol mixing ratio, $R(\xi_{aer})$, is also lognormally distributed, within the same layer boundaries as the aerosol mass mixing ratio.

3. Background Backscatter Parameterization

However, GLOBE measurement and modeling results showed that:

$$d\beta_{aer}/dM_{aer} = K_{\beta_{aer}}\, f\left(\beta_{aer}\right),$$

where β_{aer} is the volume aerosol backscatter coefficient, truncated from β_b for brevity. The correction term, $f\left(\beta_{aer}\right)$ is usually of order unity, and often very close to unity. The correction actually includes the influence of other variables, but for brevity we ignore those terms. Under these conditions, the generic parameterization can be applied to aerosol backscatter as follows:

$$PDF(\beta_{aer} \,\|\, \sigma_g, z_{\max}, z_{\min}) = F\left(\beta_{aer}\right) \times \left\{ \frac{1}{\sqrt{2\pi}\,\ln\left[\sigma_g\left(\beta_{aer}\right)\right]} \right\} \exp\left\{ -\frac{1}{2} \left(\frac{\ln\left[R\left(\beta_{aer}\right)/R_0\left(z_{\max}, z_{\min}\right)\right]}{\ln\left[\sigma_g\left(\beta_{aer}\right)\right]} \right)^2 \right\},$$

where $F\left(\beta_{aer}\right)$ is again of order unity and influenced by other variables.

For example, in MUT airmasses that had little or no exposure to stratospheric or surface-sourced contamination, B_0 decreased slightly, the low-backscatter side of the distribution had more of a tail, and the high-backscatter side of the distribution decreased more sharply, than in a lognormal distribution (i.e., a log-normal distribution except for skewing toward the low backscatter side of the mode). These conditions were more likely during fall and winter, in the southern hemisphere, over the remote oceans, at higher altitudes, and at sub-polar latitudes. Similarly, in airmasses that had increasing exposure to external contamination, B_0 increased slightly, the high-backscatter side of the distribution had more of a tail, and the low-backscatter side of the distribution decreased more sharply, than in a lognormal distribution (i.e., a log-normal distribution except for skewing toward the high backscatter side of the mode). These conditions were more likely during spring and summer, in the northern hemisphere, over and downwind from continents, at lower altitudes (but still well above local and upwind planetary boundary layers), and in subpolar latitudes.

Backscatter distributions at longer wavelengths (near-infrared to mid-infrared) were more likely to exhibit deviations similar to those described for cleaner airmasses. In addition, backscatter distributions at shorter wavelengths (near-infrared, to visible, to near ultraviolet) were more likely to exhibit deviations similar to those described for weakly contaminated airmasses; and, in otherwise clean airmasses, to exhibit higher B_0 at higher altitudes and lower B_0 at lower altitudes. These wavelength-dependent features were consistent with condensational growth of submicron particles at high relative humidities and high altitudes.

APPENDIX D: Modeling Results

Dr. Kirk A. Fuller
Earth Systems Science Center
University of Alabama in Huntsville

This Appendix includes all of the backscatter conversion modeling results that were obtained during the UAH study. These results are presented here in terms of the backscatter color ratio, $\beta_{i,j} = \beta(\lambda_i)/\beta(\lambda_j)$, and the parameterization of the color ratio by its wavelength dependence, in the form $\beta(\lambda_i)/\beta(\lambda_j) = (\lambda_j/\lambda_i)^{\alpha_{i,j}}$, for each pair of wavelengths in the CALIOP + GWOS spectral set, and for each aerosol type in the CALIOP data processing algorithm. These results were obtained using the assumptions, input data, and modeling methods described in Section 2. Following is a table of contents for these results.

General Format for 'Angstrom Exponent'

Channel	1	2	3	4
1	0.0	α_{12}	α_{13}	α_{14}
2	$-\alpha_{12}$	0.0	α_{23}	α_{24}
3	$-\alpha_{13}$	$-\alpha_{23}$	0.0	α_{34}
4	$-\alpha_{14}$	$-\alpha_{24}$	$-\alpha_{34}$	0.0

Channel	wavelength (nm)
1	355
2	532
3	1064
4	2000

Figure D1

General Format for Color Ratios

Channel	1	2	3	4
1	1.0	β_{12}	β_{13}	β_{14}
2	$1/\beta_{12}$	1.0	β_{23}	β_{24}
3	$1/\beta_{13}$	$1/\beta_{23}$	1.0	β_{34}
4	$1/\beta_{14}$	$1/\beta_{24}$	$1/\beta_{34}$	1.0

Figure D2

α_{ij} for Fine Dust

Channel	1	2	3	4
1	0.0	2.37	1.87	2.33
2		0.0	1.59	2.32
3			0.0	3.13
4				0.0

Figure D3

α_{ij} for Coarse Dust

Channel	1	2	3	4
1	0.0	0.058	0.175	0.099
2		0.0	0.24	0.11
3			0.0	0.033
4				0.0

Figure D4

α_{ij} for Bimodal Dust

Channel	1	2	3	4
1	0.0	2.12	1.59	1.51
2		0.0	1.27	1.32
3			0.0	1.37
4				0.0

Figure D5

β_i / β_j for Fine Dust

Channel	1	2	3	4
1	1.0	2.60	7.81	56.40
2		1.0	3.00	21.66
3			1.0	7.22
4				1.0

Figure D6

β_i / β_j for Coarse Dust

Channel	1	2	3	4
1	1.0	1.02	1.21	1.19
2		1.0	1.18	1.16
3			1.0	0.98
4				1.0

Figure D7

β_i / β_j for Bimodal Dust

Channel	1	2	3	4
1	1.0	2.36	5.70	13.54
2		1.0	2.42	5.74
3			1.0	2.37
4				1.0

Figure D8

α_{ij} for Fine Polluted Dust

Channel	1	2	3	4
1	0.0	1.99	1.82	2.17
2		0.0	1.72	2.22
3			0.0	2.77
4				0.0

Figure D9

α_{ij} for Coarse Polluted Dust

Channel	1	2	3	4
1	0.0	-0.89	-0.65	-0.57
2		0.0	-0.52	-0.48
3			0.0	-0.43
4				0.0

Figure D10

α_{ij} for Bimodal Polluted Dust

Channel	1	2	3	4
1	0.0	1.94	1.72	1.78
2		0.0	1.59	1.74
3			0.0	1.90
4				0.0

Figure D11

β_i / β_j for Fine Polluted Dust

Channel	1	2	3	4
1	1.0	2.23	7.35	42.23
2		1.0	3.29	18.91
3			1.0	5.74
4				1.0

Figure D12

β_i / β_j for Coarse Polluted Dust

Channel	1	2	3	4
1	1.0	0.70	0.49	0.37
2		1.0	0.70	0.53
3			1.0	0.76
4				1.0

Figure D13

β_i / β_j for Bimodal Polluted Dust

Channel	1	2	3	4
1	1.0	2.19	6.59	21.84
2		1.0	3.00	10.00
3			1.0	3.32
4				1.0

Figure D14

α_{ij} for Fine Clean Marine

Channel	1	2	3	4
1	0.0	2.02	2.10	2.17
2		0.0	2.14	2.22
3			0.0	2.30
4				0.0

Figure D15

α_{ij} for Coarse Clean Marine

Channel	1	2	3	4
1	0.0	0.12	0.64	1.02
2		0.0	0.95	1.29
3			0.0	1.67
4				0.0

Figure D16

α_{ij} for Bimodal Clean Marine

Channel	1	2	3	4
1	0.0	0.30	0.74	1.09
2		0.0	1.00	1.33
3			0.0	1.68
4				0.0

Figure D17

β_i / β_j for Fine Clean Marine

Channel	1	2	3	4
1	1.0	2.26	10.00	42.71
2		1.0	4.42	18.87
3			1.0	4.27
4				1.0

Figure D18

β_i / β_j for Coarse Clean Marine

Channel	1	2	3	4
1	1.0	1.05	2.03	5.81
2		1.0	1.93	5.53
3			1.0	2.87
4				1.0

Figure D19

β_i / β_j for Bimodal Clean Marine

Channel	1	2	3	4
1	1.0	1.13	2.26	6.56
2		1.0	2.00	5.81
3			1.0	2.90
4				1.0

Figure D20

α_{ij} for Fine Clean Continental

Channel	1	2	3	4
1	0.0	1.97	2.09	2.12
2		0.0	2.17	2.16
3			0.0	2.15
4				0.0

Figure D21

α_{ij} for Coarse Clean Continental

Channel	1	2	3	4
1	0.0	0.919	0.964	1.06
2		0.0	0.99	1.10
3			0.0	1.23
4				0.0

Figure D22

α_{ij} for Bimodal Clean Continental

Channel	1	2	3	4
1	0.0	1.13	1.13	1.19
2		0.0	1.13	1.21
3			0.0	1.29
4				0.0

Figure D23

β_i / β_j for Fine Clean Continental

Channel	1	2	3	4
1	1.0	2.21	9.99	38.74
2		1.0	4.50	17.50
3			1.0	3.89
4				1.0

Figure D24

β_i / β_j for Coarse Clean Continental

Channel	1	2	3	4
1	1.0	1.45	2.88	6.26
2		1.0	1.99	4.32
3			1.0	2.17
4				1.0

Figure D25

β_i / β_j for Bimodal Clean Continental

Channel	1	2	3	4
1	1.0	1.58	3.45	7.78
2		1.0	2.19	4.93
3			1.0	2.25
4				1.0

Figure D26

α_{ij} for Fine Polluted Continental

Channel	1	2	3	4
1	0.0	1.84	1.88	2.04
2		0.0	1.90	2.10
3			0.0	2.33
4				0.0

Figure D27

α_{ij} for Coarse Polluted Continental

Channel	1	2	3	4
1	0.0	-2.31	-0.54	-0.33
2		0.0	0.50	0.28
3			0.0	0.034
4				0.0

Figure D28

α_{ij} for Coarse Polluted Continental, Flat Absorption into UV

Channel	1	2	3	4
1	0.0	-0.27	-0.083	-0.040
2		0.0	0.025	0.029
3			0.0	0.034
4				0.0

Figure D29

α_{ij} for Bimodal Polluted Continental

Channel	1	2	3	4
1	0.0	1.82	1.85	1.96
2		0.0	1.86	2.00
3			0.0	2.15
4				0.0

Figure D30

β_i / β_j for Fine Polluted Continental

Channel	1	2	3	4
1	1.0	2.10	7.85	34.11
2		1.0	3.73	16.21
3			1.0	4.35
4				1.0

Figure D31

β_i / β_j for Coarse Polluted Continental

Channel	1	2	3	4
1	1.0	0.39	0.55	0.57
2		1.0	1.41	1.44
3			1.0	1.02
4				1.0

Figure D32

β_i / β_j for Bimodal Polluted Continental

Channel	1	2	3	4
1	1.0	2.09	7.58	29.53
2		1.0	3.63	14.14
3			1.0	3.89
4				1.0

Figure D33

α_{ij} for Fine Dry Smoke

Channel	1	2	3	4
1	0.0	1.59	1.85	2.00
2		0.0	2.00	2.13
3			0.0	1.27
4				0.0

Figure D34

α_{ij} for Coarse Dry Smoke

Channel	1	2	3	4
1	0.0	0.44	0.372	0.02
2		0.0	0.33	-0.11
3			0.0	-0.59
4				0.0

Figure D35

α_{ij} for Bimodal Dry Smoke

Channel	1	2	3	4
1	0.0	1.58	1.83	1.94
2		0.0	1.98	2.05
3			0.0	2.13
4				0.0

Figure D36

β_i / β_j for Fine Dry Smoke

Channel	1	2	3	4
1	1.0	1.90	7.60	31.84
2		1.0	4.00	16.76
3			1.0	4.19
4				1.0

Figure D37

β_i / β_j for Coarse Dry Smoke

Channel	1	2	3	4
1	1.0	1.19	1.50	1.04
2		1.0	1.26	0.87
3			1.0	0.69
4				1.0

Figure D38

β_i / β_j for Bimodal Dry Smoke

Channel	1	2	3	4
1	1.0	1.90	7.49	28.73
2		1.0	3.95	15.15
3			1.0	3.84
4				1.0

Figure D39

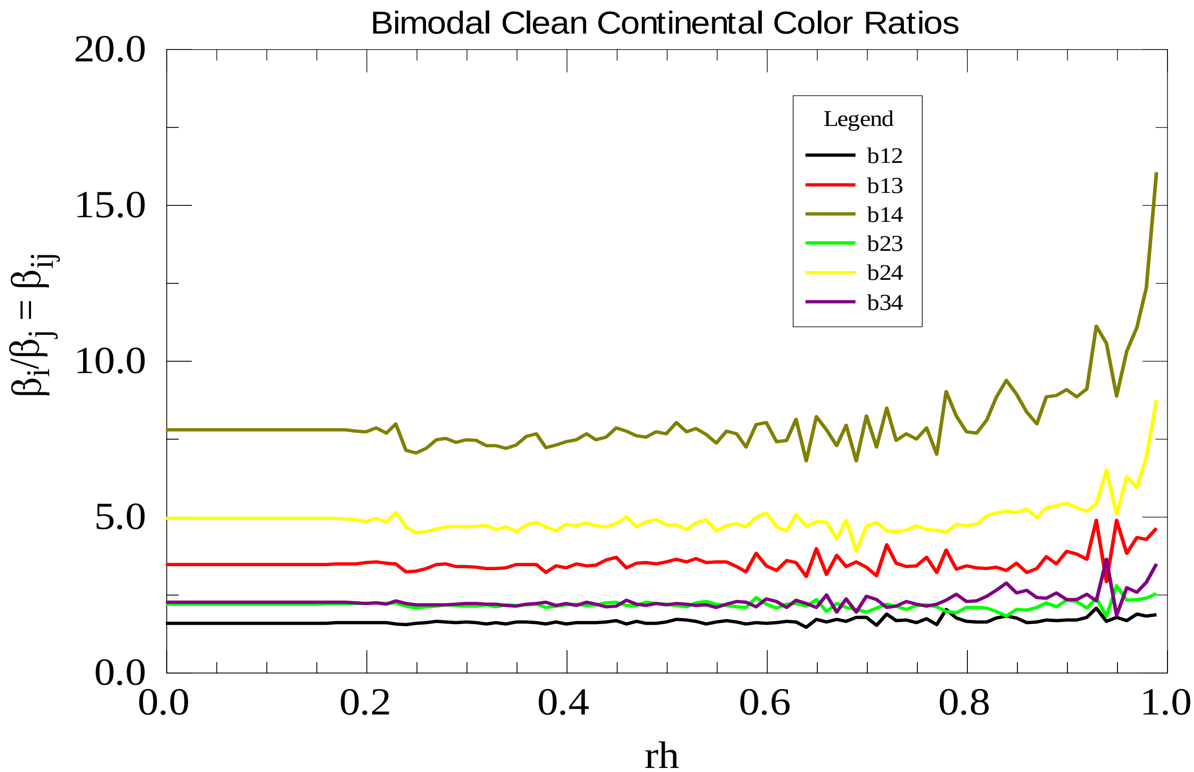
Bimodal Clean Continental Color Ratios
Legend
b12
b13
b14
b23
b24
b34
20.0
15.0
10.0
5.0
0.0
0.0
0.2
0.4
0.6
0.8
1.0
rh
$\beta_i/\beta_j = \beta_{ij}$

Figure D40

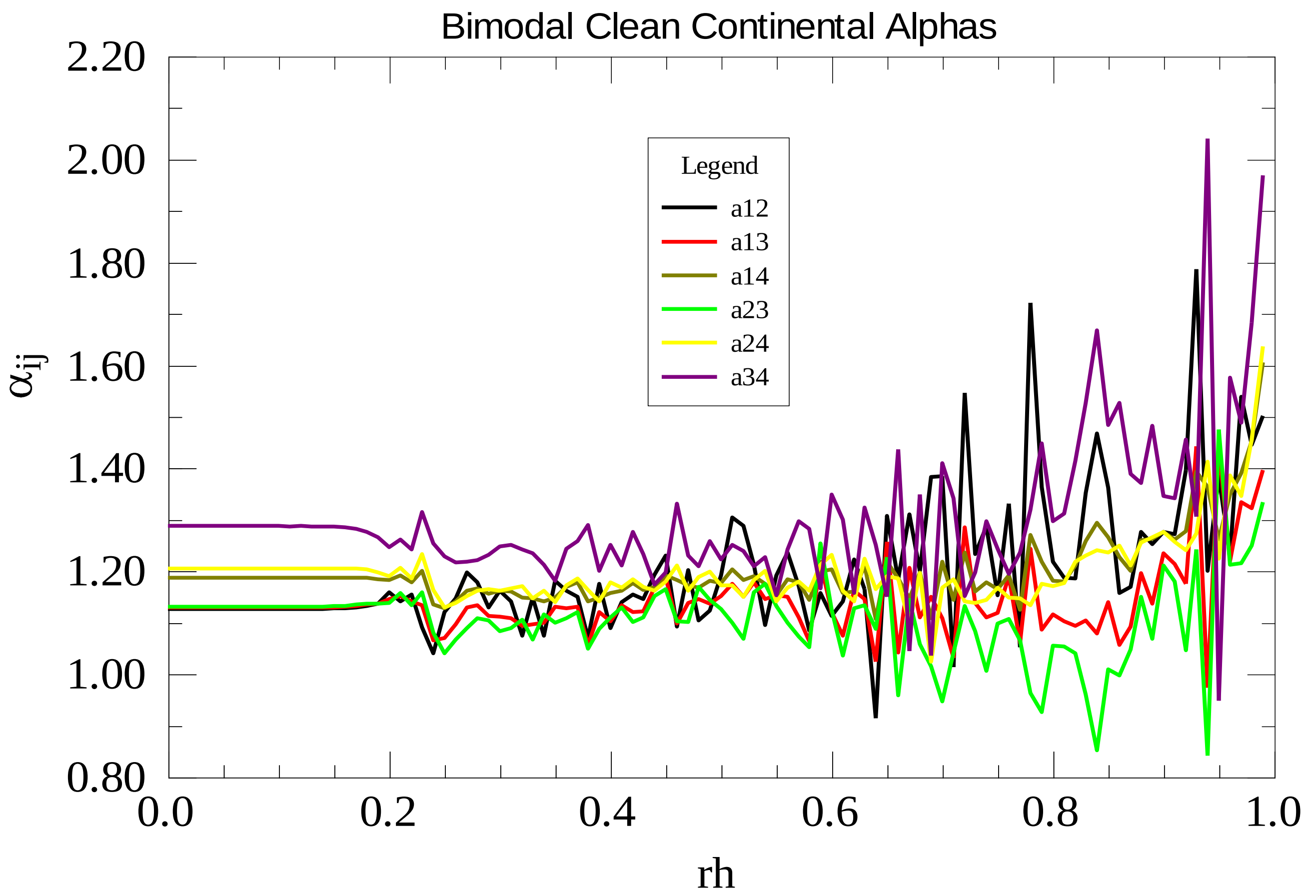
Bimodal Clean Continental Alphas
2.20
2.00
1.80
1.60
1.40
1.20
1.00
0.80
0.0
0.2
0.4
0.6
0.8
1.0
rh
α_{ij}
Legend
a12
a13
a14
a23
a24
a34

Figure D41

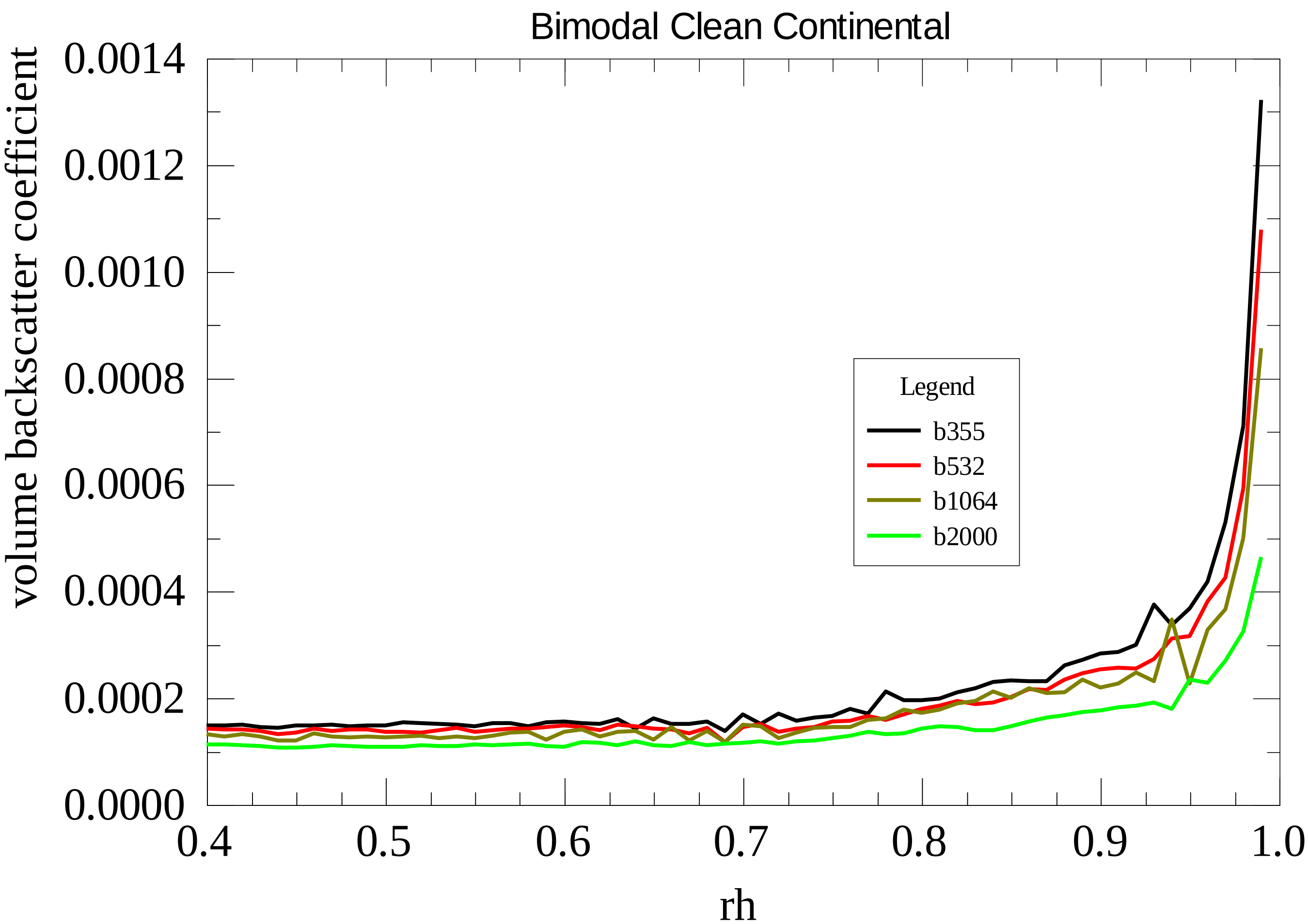

Bimodal Clean Continental
volume backscatter coefficient
0.0014
0.0012
0.0010
0.0008
0.0006
0.0004
0.0002
0.0000
0.4
0.5
0.6
0.7
0.8
0.9
1.0
rh
Legend
b355
b532
b1064
b2000

Figure D42

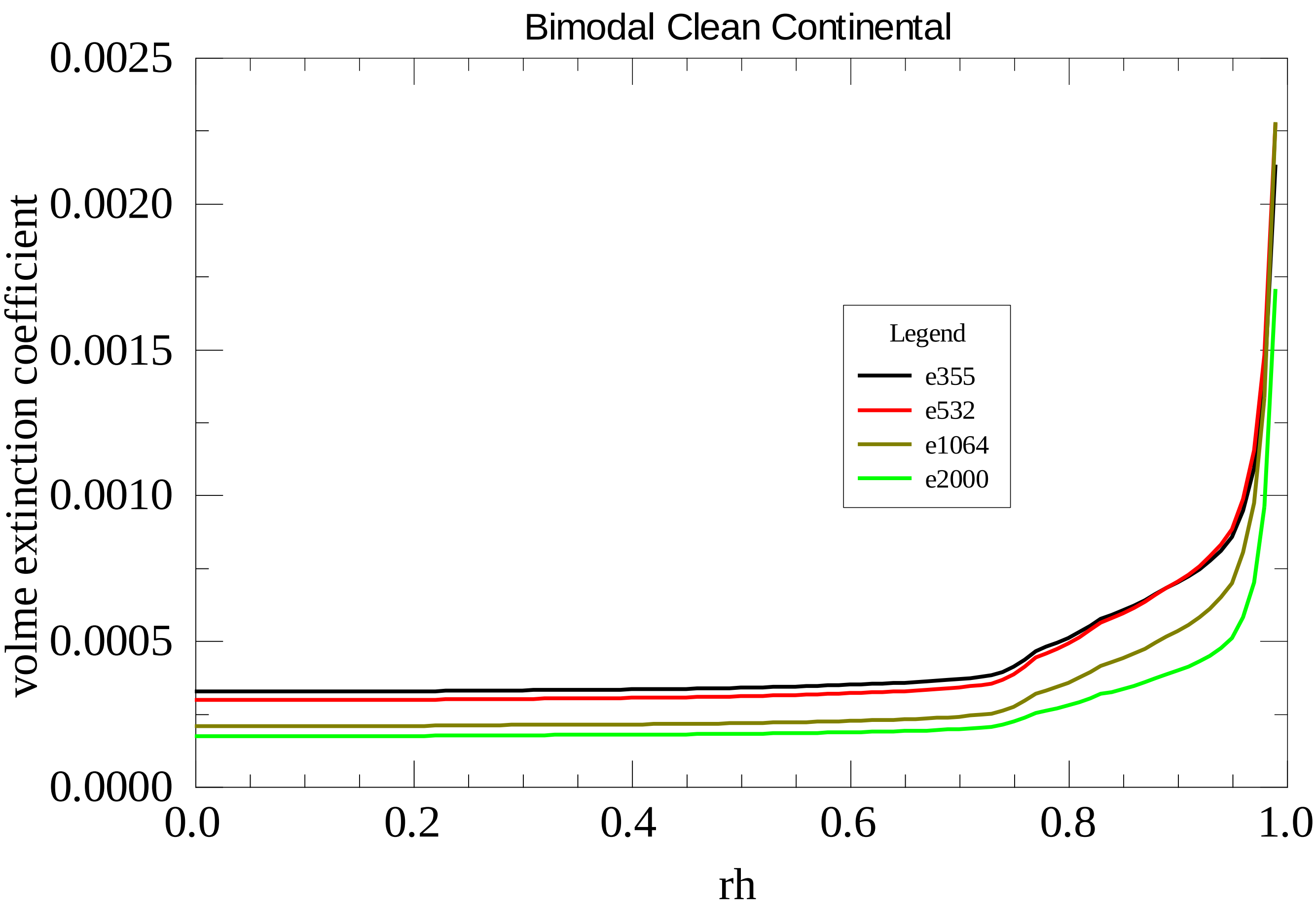
Bimodal Clean Continental
volme extinction coefficient
0.0025
0.0020
0.0015
0.0010
0.0005
0.0000
0.0
0.2
0.4
0.6
0.8
1.0
rh
Legend
e355
e532
e1064
e2000

Figure D43

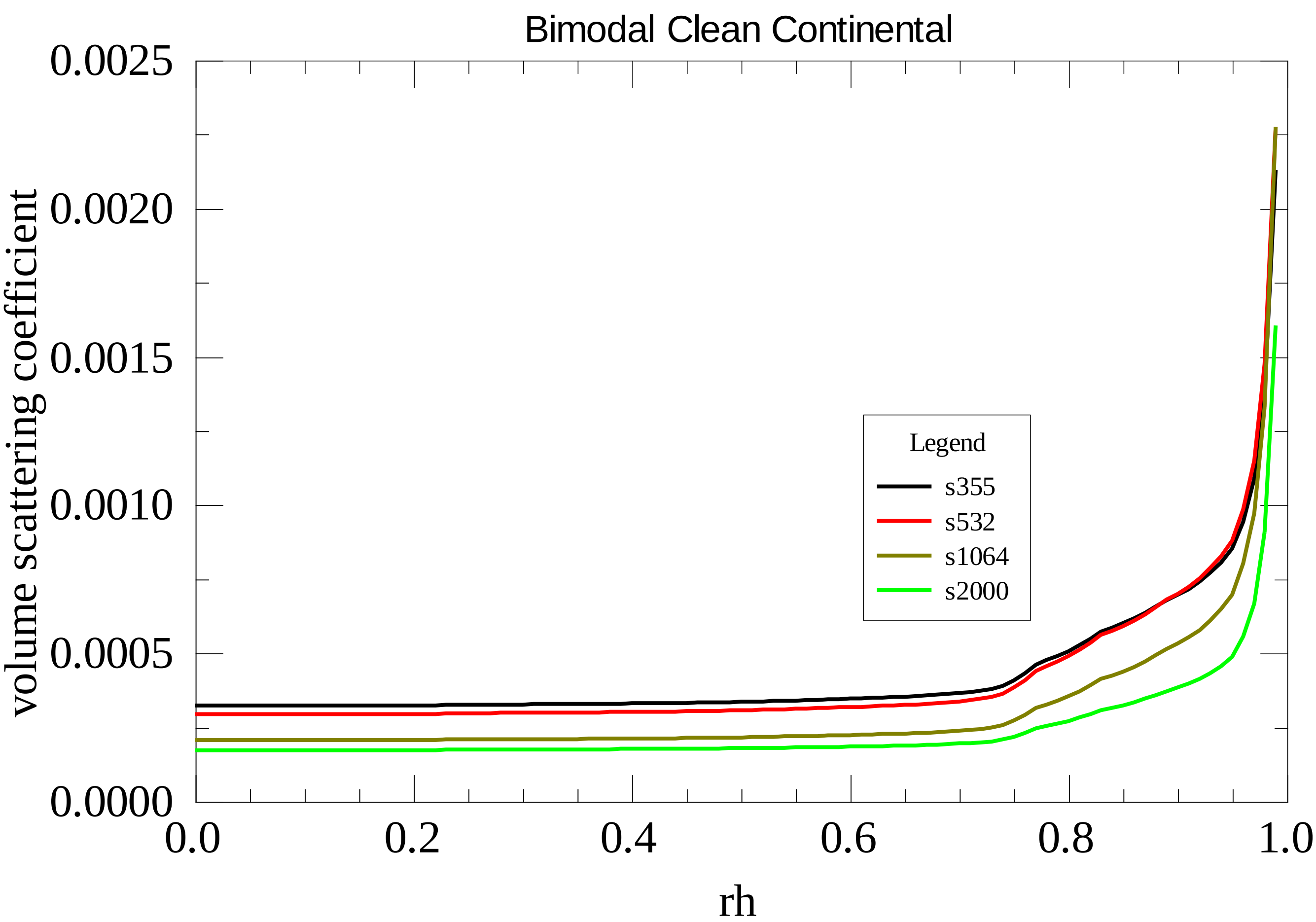
Bimodal Clean Continental
0.0025
0.0020
0.0015
0.0010
0.0005
0.0000
volume scattering coefficient
0.0
0.2
0.4
0.6
0.8
1.0
rh
Legend
s355
s532
s1064
s2000

Figure D44

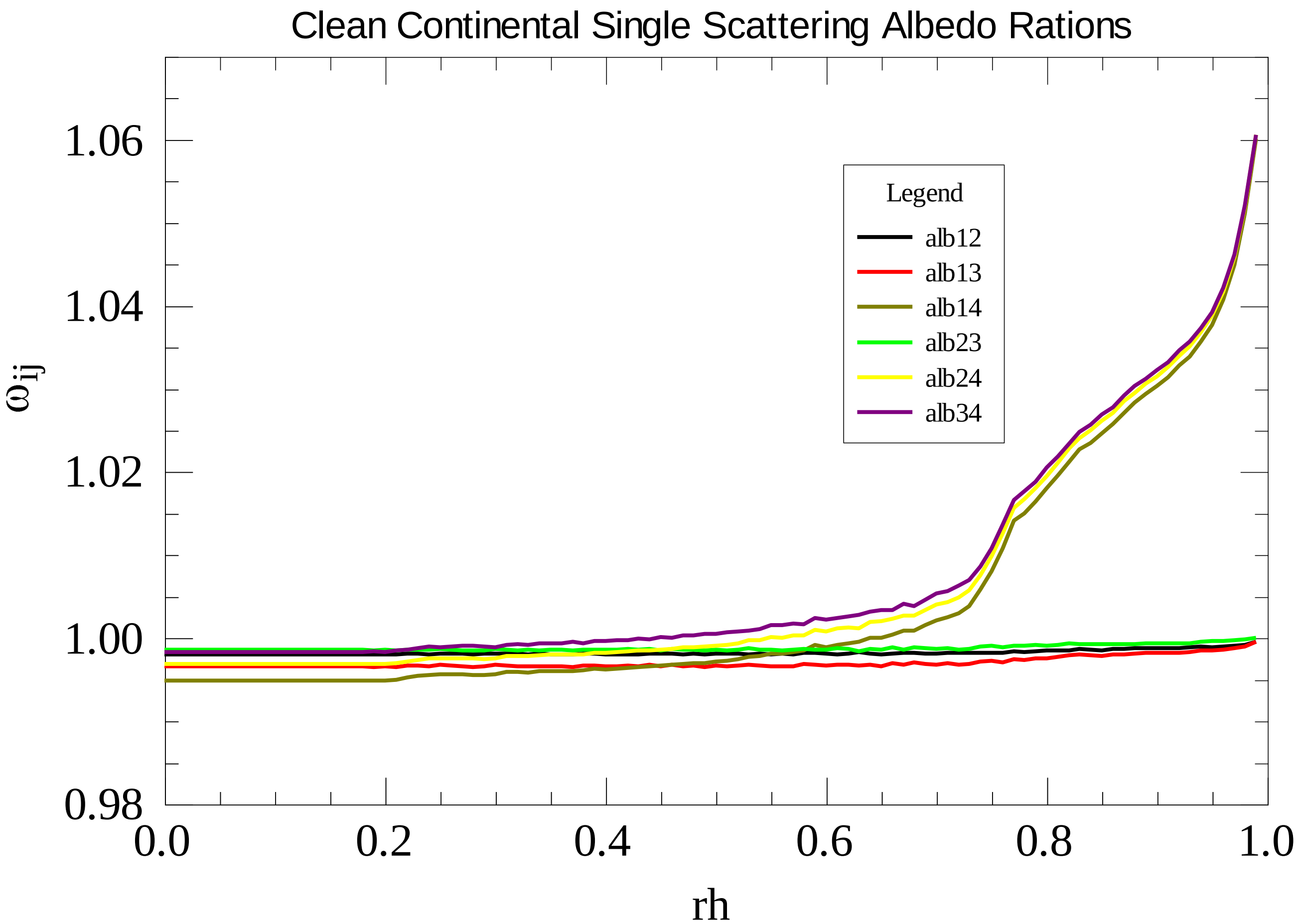

Clean Continental Single Scattering Albedo Rations
1.06
1.04
1.02
1.00
0.98
ω_{ij}
0.0
0.2
0.4
0.6
0.8
1.0
rh
Legend
alb12
alb13
alb14
alb23
alb24
alb34

Figure D45

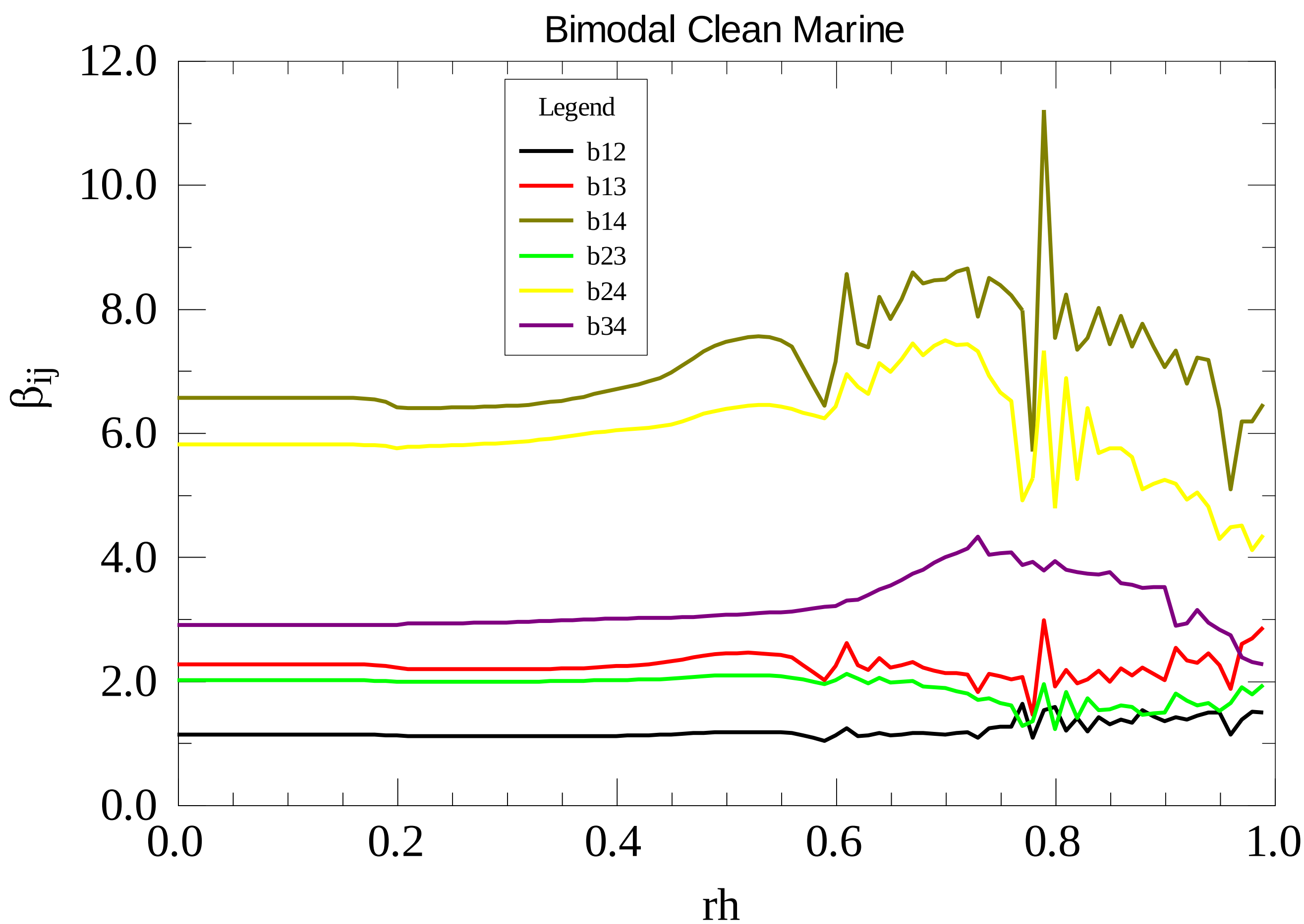
Bimodal Clean Marine
Legend
b12
b13
b14
b23
b24
b34
12.0
10.0
8.0
6.0
4.0
2.0
0.0
βij
0.0
0.2
0.4
0.6
0.8
1.0
rh

Figure D46

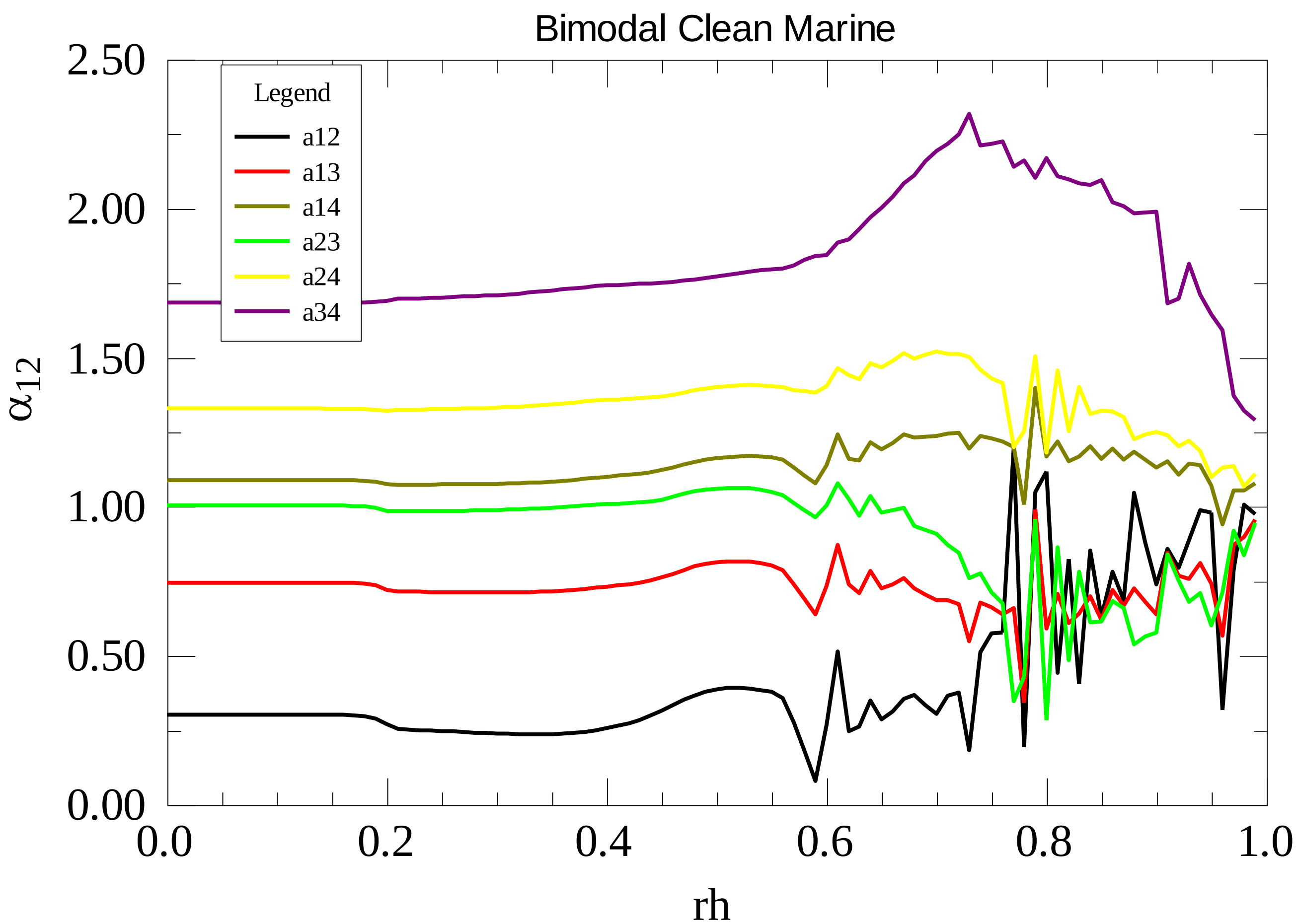

Bimodal Clean Marine
Legend
a12
a13
a14
a23
a24
a34
2.50
2.00
1.50
1.00
0.50
0.00
0.0
0.2
0.4
0.6
0.8
1.0
rh
α12

Figure D47

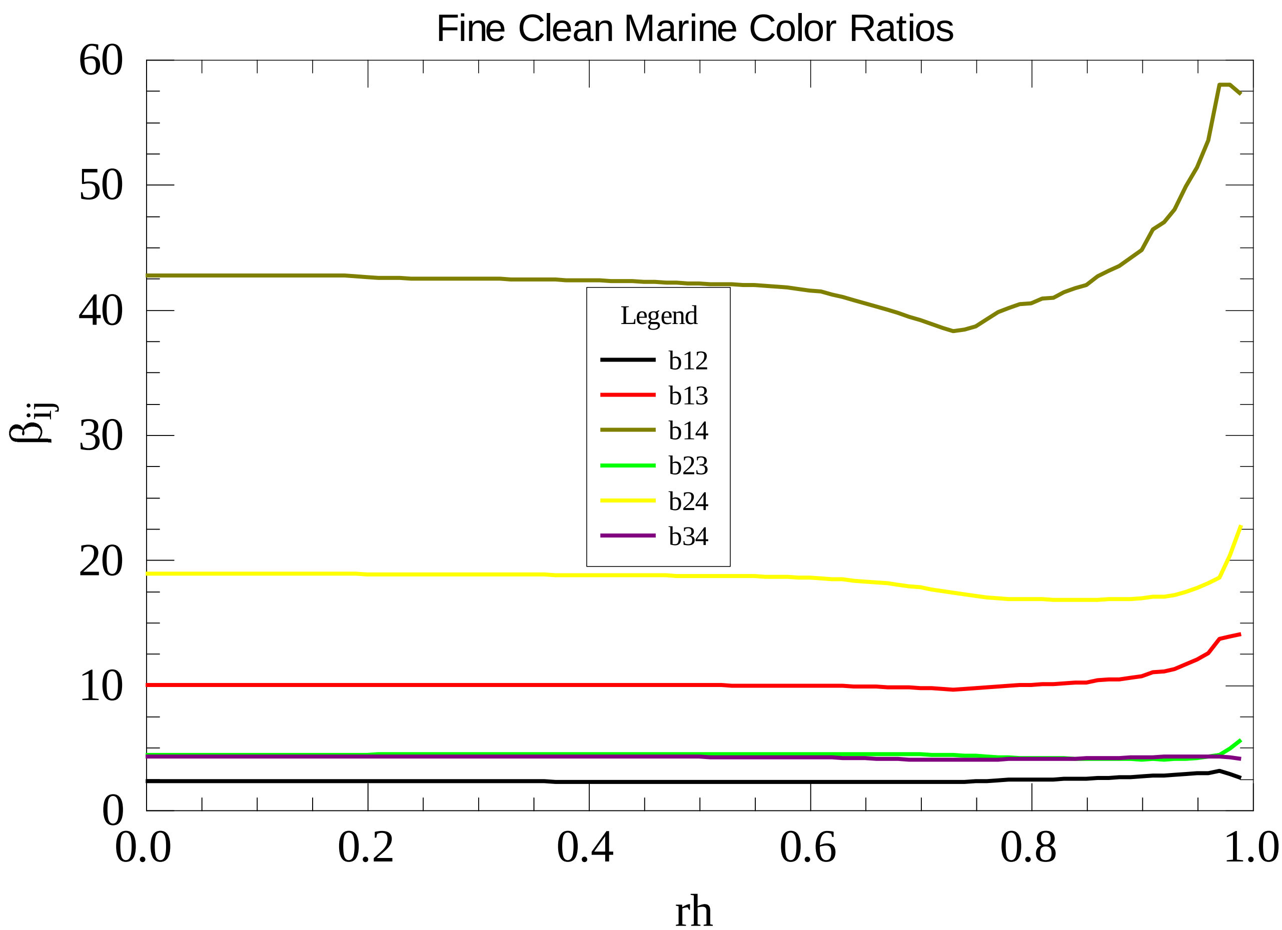

Fine Clean Marine Color Ratios
60
50
40
30
20
10
0
0.0
0.2
0.4
0.6
0.8
1.0
rh
βij
Legend
b12
b13
b14
b23
b24
b34

Figure D48

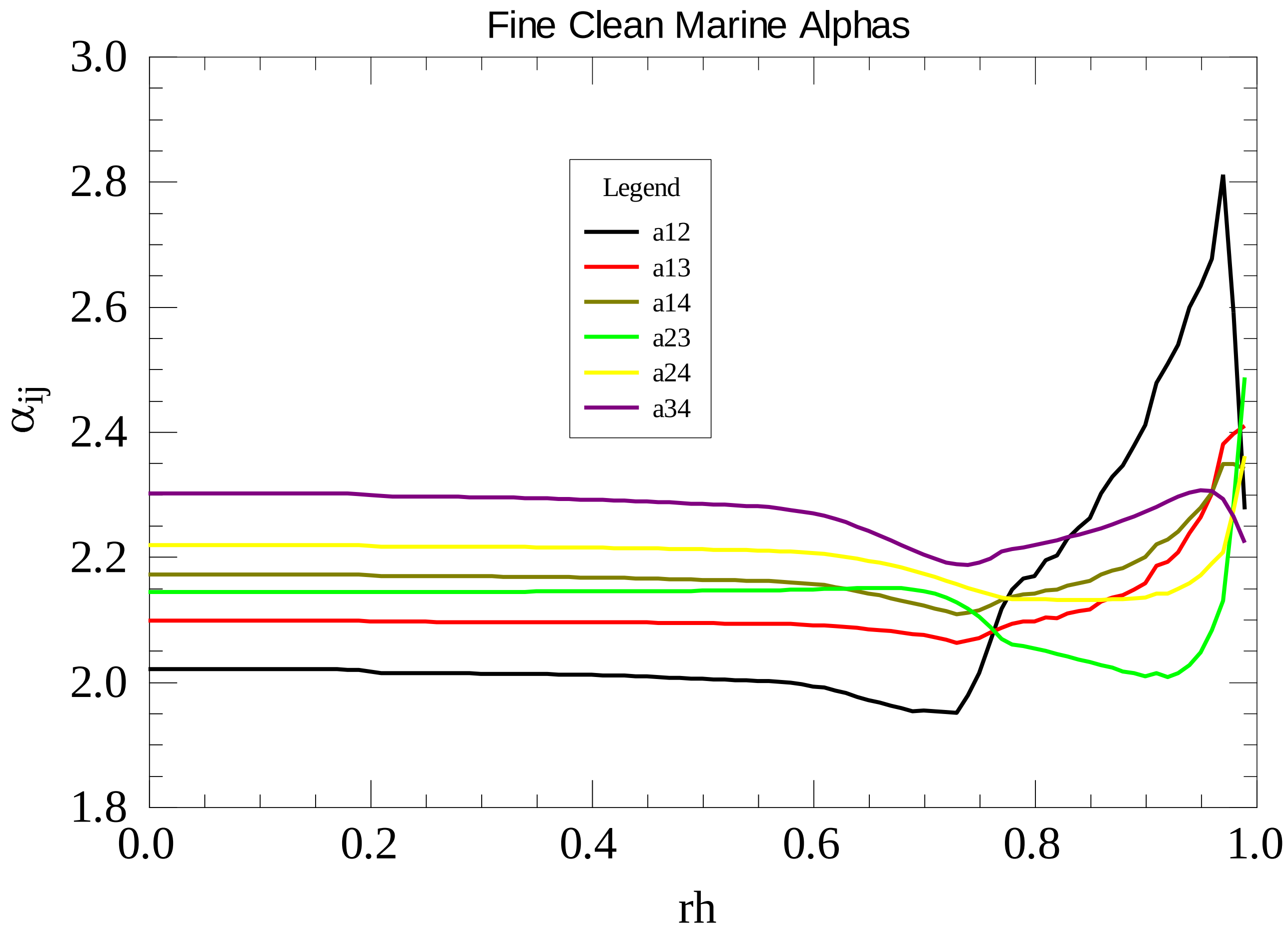
Fine Clean Marine Alphas
3.0
2.8
2.6
2.4
2.2
2.0
1.8
0.0
0.2
0.4
0.6
0.8
1.0
rh
α_{ij}
Legend
a12
a13
a14
a23
a24
a34

Figure D49

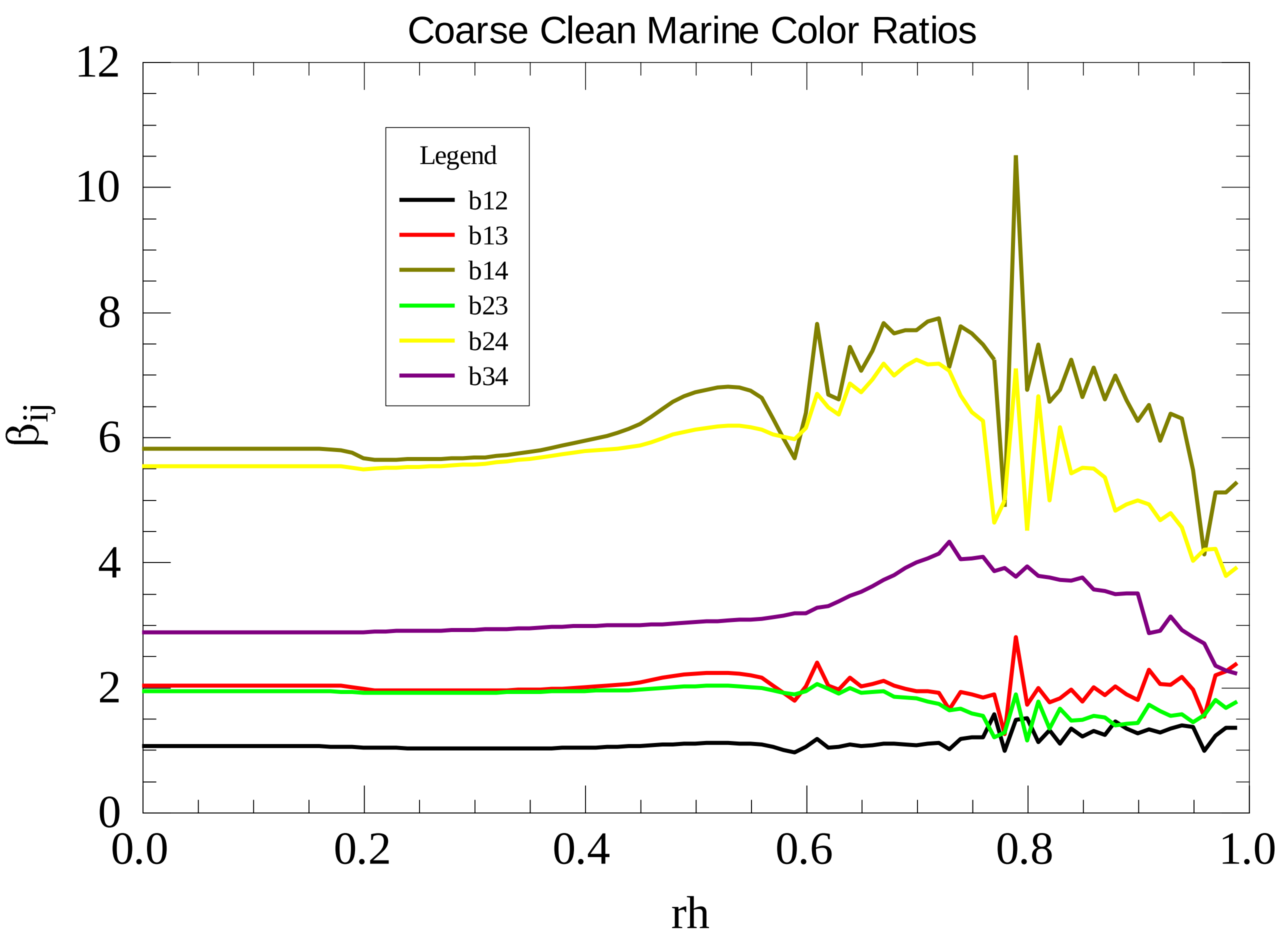
Coarse Clean Marine Color Ratios
Legend
b12
b13
b14
b23
b24
b34
β_{ij}
rh
0
2
4
6
8
10
12
0.0
0.2
0.4
0.6
0.8
1.0

Figure D50

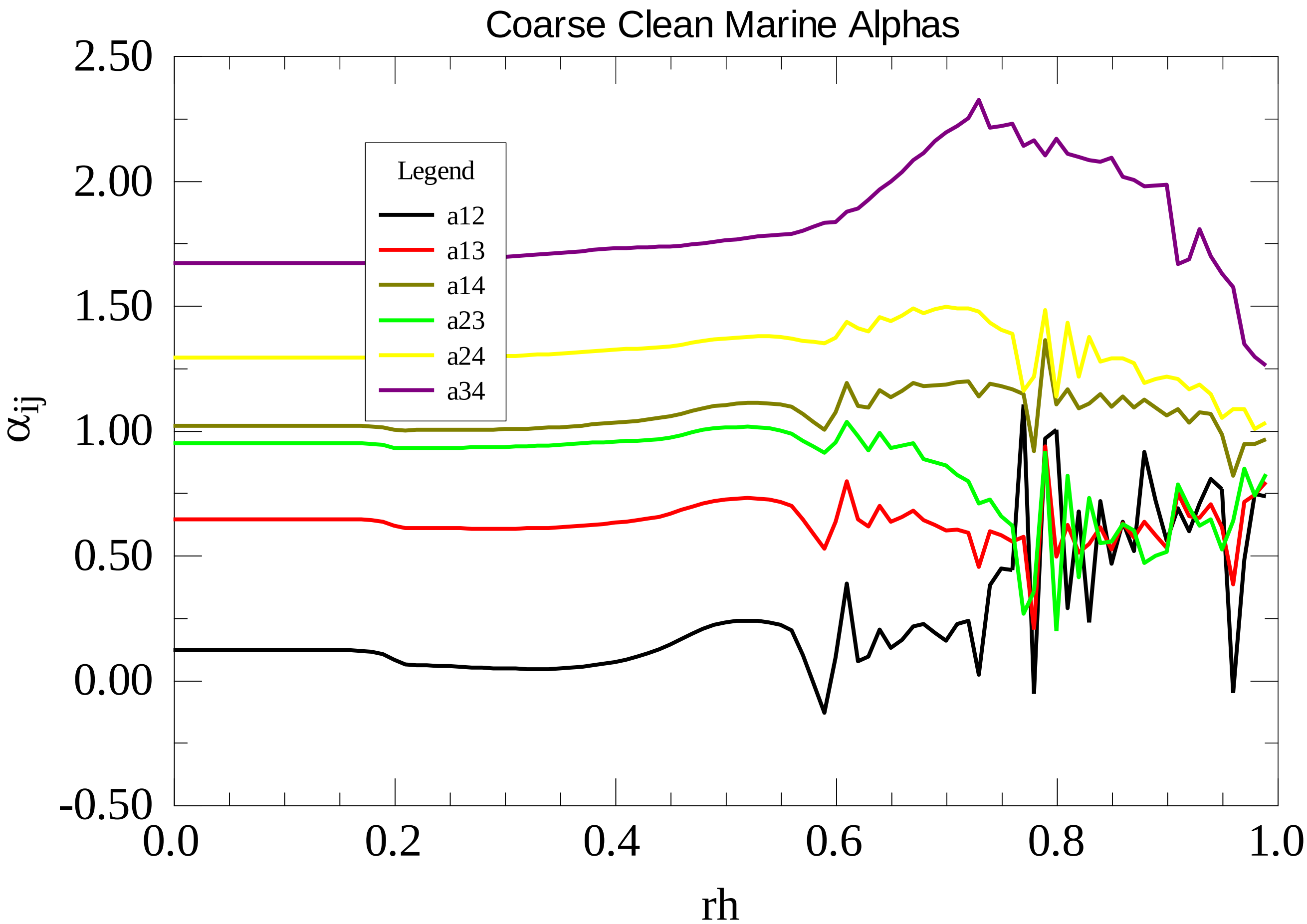
Coarse Clean Marine Alphas
Legend
a12
a13
a14
a23
a24
a34
2.50
2.00
1.50
1.00
0.50
0.00
-0.50
0.0
0.2
0.4
0.6
0.8
1.0
rh
α_{ij}

Figure D51

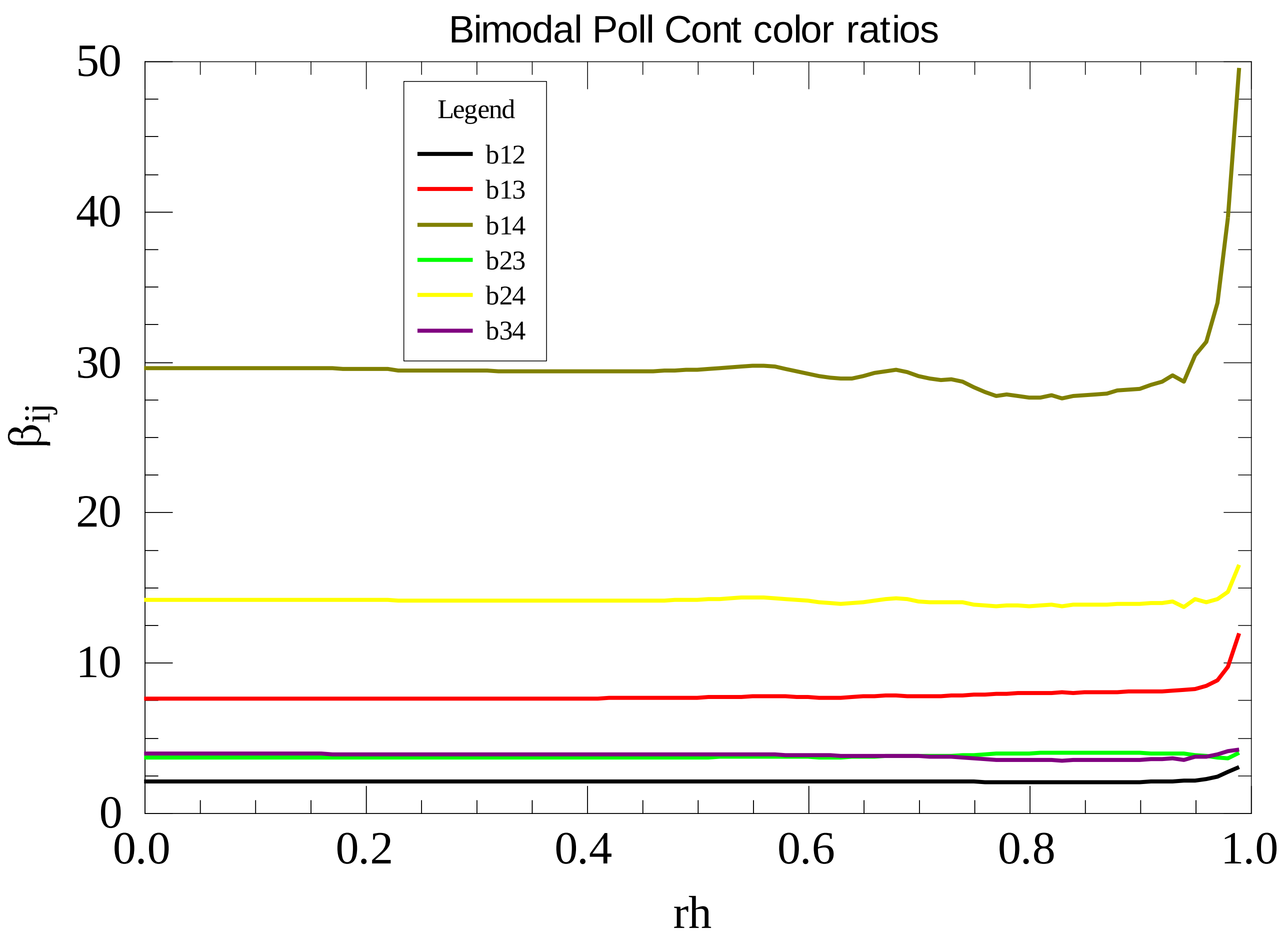

Bimodal Poll Cont color ratios
Legend
b12
b13
b14
b23
b24
b34
50
40
30
20
10
0
0.0
0.2
0.4
0.6
0.8
1.0
rh
βij

Figure D52

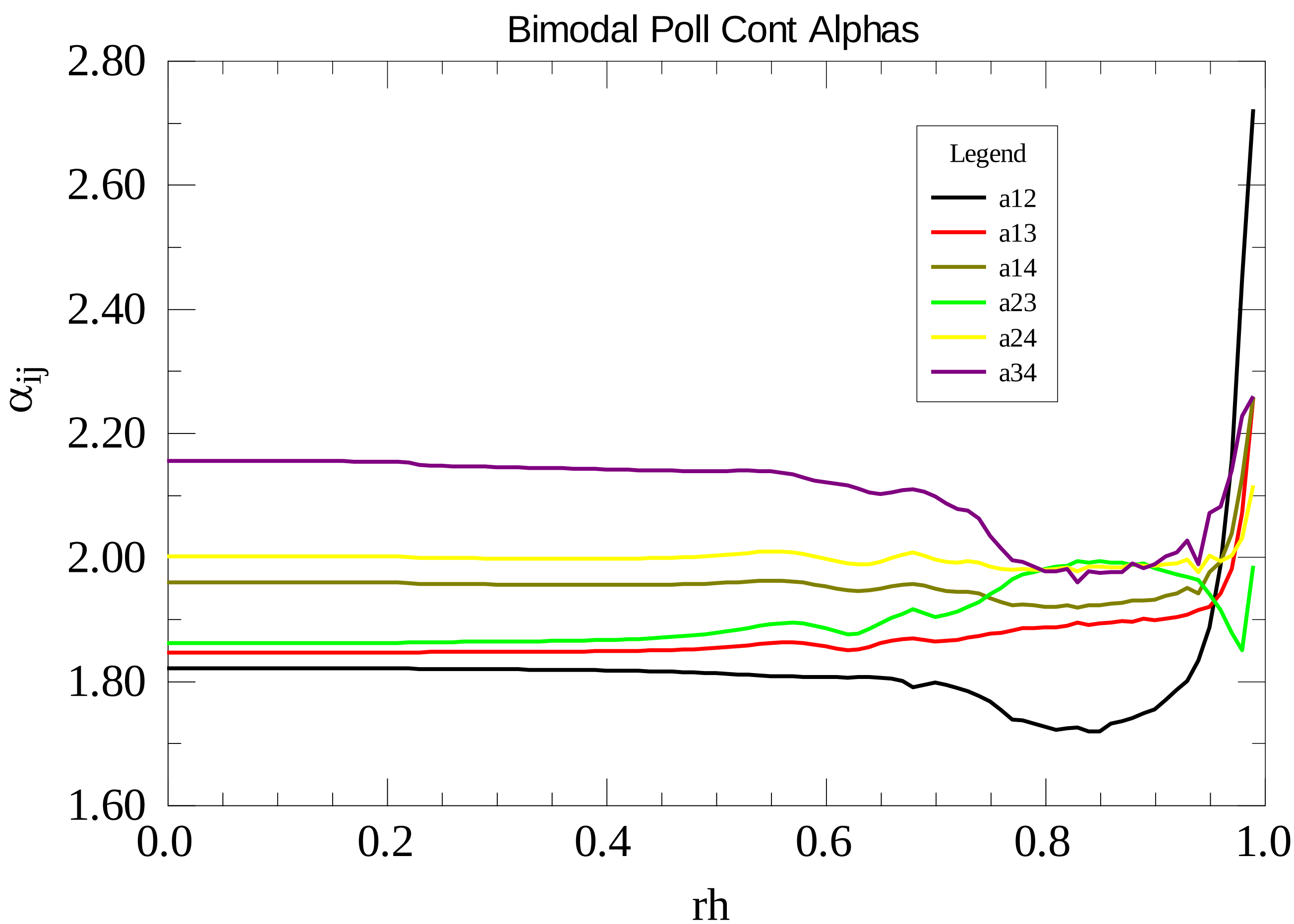
Bimodal Poll Cont Alphas
2.80
2.60
2.40
2.20
2.00
1.80
1.60
0.0
0.2
0.4
0.6
0.8
1.0
α_{ij}
rh
Legend
a12
a13
a14
a23
a24
a34

Figure D53

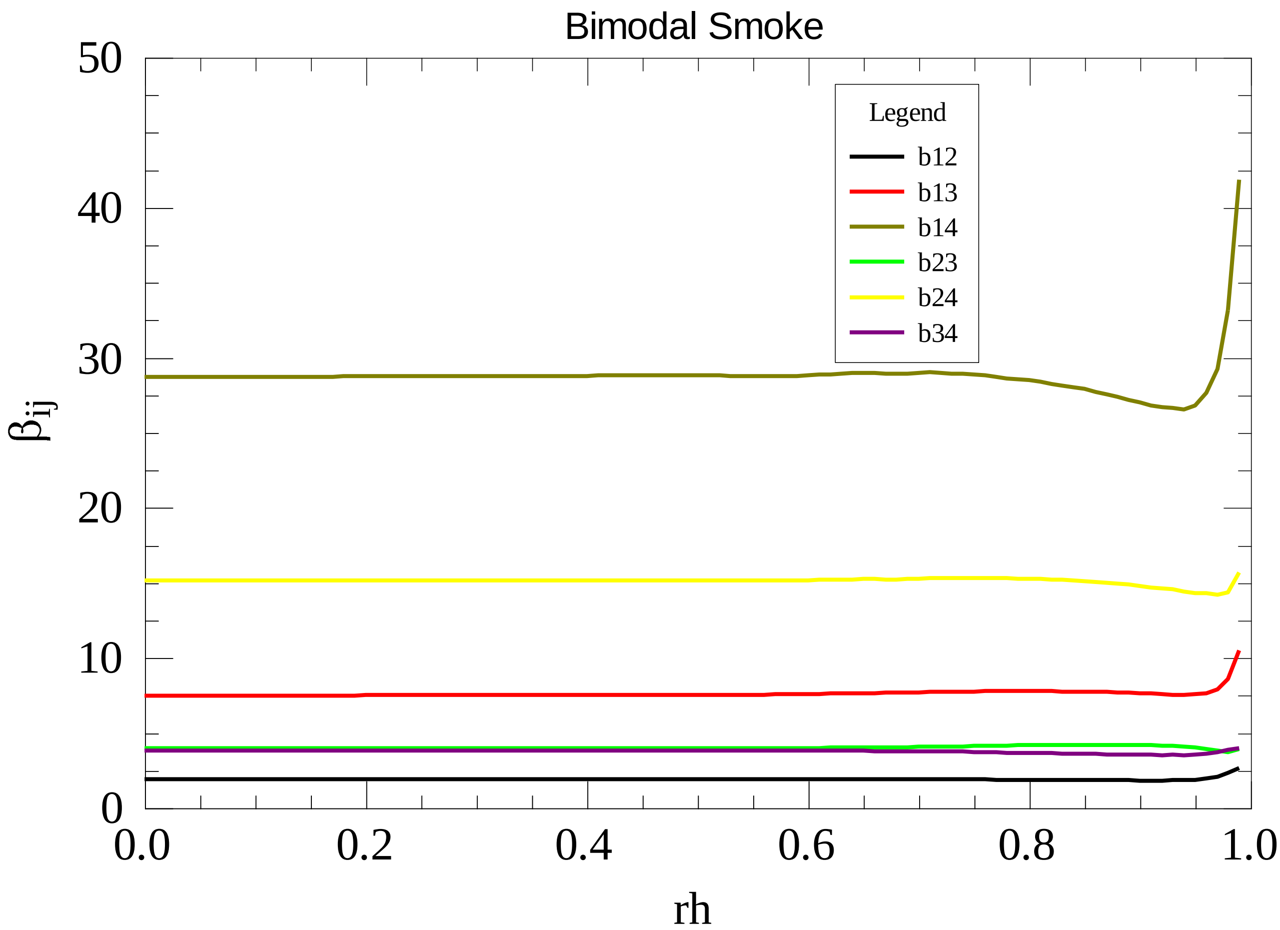

Bimodal Smoke
Legend
b12
b13
b14
b23
b24
b34
50
40
30
20
10
0
0.0
0.2
0.4
0.6
0.8
1.0
rh
βij

Figure D54

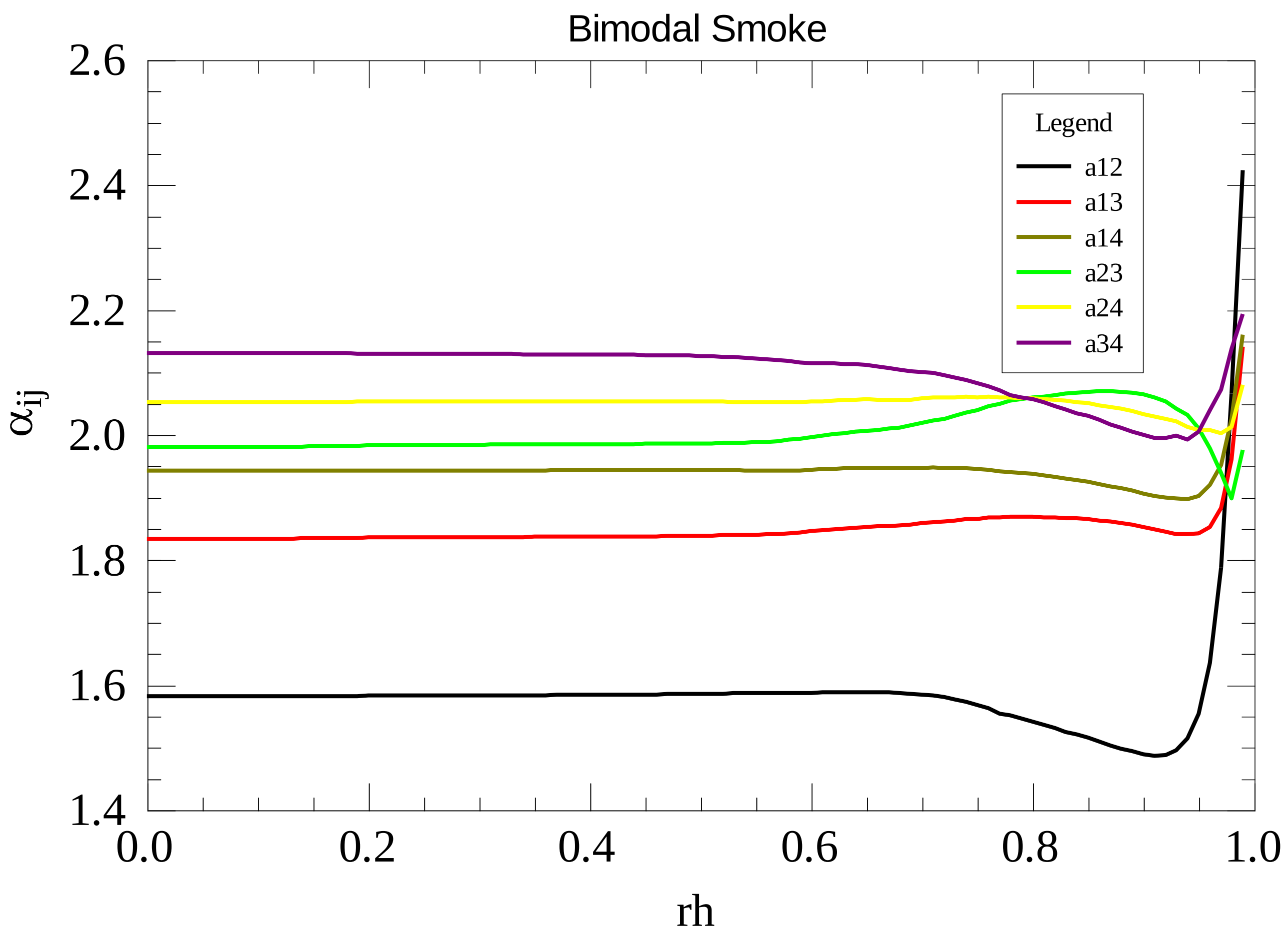
Bimodal Smoke
Legend
a12
a13
a14
a23
a24
a34
2.6
2.4
2.2
2.0
1.8
1.6
1.4
0.0
0.2
0.4
0.6
0.8
1.0
rh
α_{ij}

Figure D55